Modeling, Analysis, and Validation of Temperature Dependent Vibration Induced Fretting Corrosion

by

Rebecca David Ibrahim

A thesis submitted to the Graduate Faculty of
Auburn University
in partial fulfillment of the
requirements for the Degree of
Master of Science in Mechanical Engineering

Auburn, Alabama
August 9, 2010

Keywords: electrical contacts, fretting corrosion, modeling, finite element analysis, temperature dependent material properties, static friction coefficient, experiment

Approved by

George T. Flowers, Chair, Alumni Professor of Mechanical Engineering
Jeffrey C. Suhling, Quina Distinguished Professor of Mechanical Engineering
Roy W. Knight, Assistant Professor of Mechanical Engineering

Abstract

Connector reliability is an extremely important factor in electronic packaging, especially with regard to vehicle electronics. Two of the major drivers for fretting corrosion are vibration and thermal cycling. Most previous studies in this area have focused on experimental evaluations of both thermal induced fretting and vibration induced fretting separately; extremely few, if any, have combined the two. In recent years, previous studies have focused on the development and analysis of such models for vibration driven fretting corrosion.

The present study extends this work into the thermally-driven fretting and the effects of vibration at different temperatures. This was accomplished by utilizing sources that have documented experimental work on temperature dependent materials, and by conducting experiments to find the temperature dependent static friction coefficient as well, and entering the temperature dependent material properties into the ABAQUS^{TM} model.

The experiment conducted to determine the temperature dependent static friction coefficient used an automated inclined plane (based on Newton's Second Law). The apparatus was first utilized to test how pressure affects the static friction coefficient at room temperature. The experimental data obtained from that experiment was then compared to analytical data from the literature. Both the experimental data and the analytical data were compatible and showed that as the mass increases the static friction coefficient decreases. The apparatus was then placed in a temperature chamber and data was collected to see the effect of temperature on the static friction coefficient. Using several masses, it was found that as the temperature increased the static friction coefficient decreased, as expected.

Using ABAQUS™, two models were developed for a single blade-receptacle connector pair and the resulting models were analyzed for fretting behavior. One model was developed to analyze how thermal cycling induces fretting corrosion. Temperature dependent properties were used for the Static Friction Coefficient, Young's Modulus, Thermal Conductivity, Thermal Expansion, and Heat Transfer Coefficient. The results from this model showed that as the frequency of the temperature change increases the larger the temperature needed to induce fretting corrosion. The second model analyzed how temperature affected vibration induced fretting, and three temperatures were analyzed. The effect of temperature on the vibration induced fretting corrosion could not be observed, but that could be due to the small range of temperature change.

Acknowledgements

I thank God the Father for sending this Son to die on the cross for me. The most important gift He has given me is my salvation. But along other gifts there are two other gifts I must thank Him for: One of which is for being "… a shield for me; my glory, and the lifter up of my head" (Ps. 3:3, ESV) during my time at Auburn, and the second for putting the following people in my path:

My parents, David and Jeanette Ibrahim, have sacrificed so much for me over the years words cannot express my appreciation to them. Their unconditional love is shown through constantly encouraging me to use my God given abilities. Without their support, I would not be here today.

My advisor, Dr. George T. Flowers, who has lead me through this project and through my journey at Auburn. I will always cherish his wise instruction and tremendous support particularly during the challenging times of my journey. I would also like to express my gratitude to the rest of my committee, Dr. Knight and Dr. Suhling who have given me their invaluable advice on my research and for editing my thesis. Also Dr. Jackson has played a huge part in helping determine how the static friction coefficient is a function of temperature.

Lt. James Dickey has been there to calm me down /make me laugh when classes or research did not go as planned. He has been so patient as I was writing my thesis. As deadlines would approach I would cancel lunch dates; he never complained, instead he would come to my office on Saturday evenings to keep me company as the final simulations ran.

The professors at Olivet Nazarene University have taught me that “I was called to make a life, not a living” (Bowling, 2007). But I would like to thank four professors in particular: Dr. Ivor Newsham, Professor Mike Morgan, Dr. Joseph Schroeder, and Dr. Rodney Korthals; those four gentlemen have taught me the basics in the engineering field and in the process have encouraged me to continue my education.

I would also like to thank my other colleagues: Brittney Consuegra, Grant Roth, Chen Chen, Robert Jantz, Bruce Shue, and Jessen Pregassen for their personal friendship, academic support and advice. I would also like to thank Jyoti Ajitsaria and George Vallone for constructing the experimental apparatus and Jack Maddox for helping with the uncertainty analysis.

Last but not least. I would like to thank my home church in Illinois, Kankakee First Church of the Nazarene and the church I attend in Auburn, Lakeview Baptist Church. Both congregations have supported me with prayers and words of encouragement. But most importantly, the fellowship that I have experienced in both places has been invaluable sources for my spiritual growth.

Table of Contents

List of Tables

List of Figures

Nomenclature

A_0 contact area due to the normal load alone (m^2)

a constant (1/ ºC)

A_n nominal area of contact surface (m^2)

A_s contact area due to sliding inception (m^2)

c specific heat of the workpiece (J/kg- ºC)

C constant dependent on Poisson's ratio (non-dimensional)

$C_\xi^i = \frac{\xi!}{(\xi - i)!i!}$ (non-dimensional)

d the distance between the mean of asperity heights and the smooth rigid surface (m)

E' Hertz Modulus of Elasticity (Pa)

E_i modulus of elasticity of material i (Pa)

F Coulomb friction (page 5) or external force (page 6)

F_f friction force (N)

F_x force in the x-direction (N)

F_y force in the y-direction (N)

g gravitational acceleration (m/s^2)

H hardness of the softer material (non-dimensional)

k thermal conductivity of the workpiece (W/m- ºC)

K hardness factor (non-dimensional)

l_C the chip tool contact length (m)

M magnitude of transfer function (mm)

m mass (g)

m_0 spectral moment root mean square squared of the variance of height (m^2)

m_2 spectral moment root mean square squared of the mean square slope (non-dimensional)

m_4 spectral moment root mean square squared of the mean square curvature (1/ m^2)

P_0 pressure of the tool tip

P the real contact load (N)

$P*$ dimensionless normal load

q constant found by experimental means (non-dimensional)

Q_{max} maximum tangential force needed to shear the contact points (N)

R asperity radius (m)

T_0 reference temperature (ºC)

T_1 the temperature at the outflow of the primary shear zone (ºC)

T temperature (ºC)

T_f melting temperature of the workpiece material (ºC)

$\overline{T}_{\text{int}}$ mean temperature (temperature distribution) (ºC)

V_c chip velocity (m/s)

Y Yield Strength (N/m^2)

z height of an asperity measured from the mean of asperity height (m)

Z_f relative motion (mm)

Greek Letters:

α bandwidth parameter (non-dimensional)

ρ density of the workpiece material (kg/m^3)

$\Delta\gamma$ change in surface energy (J)

η area density of asperity ($1/m^2$)

θ adhesion parameter (non-dimensional)

μ static friction coefficient (page 6)

μ_0 friction coefficient at reference temperature T_0 (non-dimensional)

$\overline{\mu_0}$ constant found by experimental means (non-dimensional)

$\overline{\mu}$ mean friction coefficient (non-dimensional)

ν relative velocity (m/s)

σ_s standard deviation of asperity heights (m)

υ Poisson's ratio (non-dimensional)

ϕ probability density (1/m) (page 28), phase angle (rad) (page 58)

Ψ plasticity index (non-dimensional)

$\omega = z - d$ (m)

Subscript:

ξ parameter that controls the pressure profile

Superscript:

i index in the r direction

j index in the y direction

* non-dimensionalized variable

$^-$ variable acting on one asperity only

CHAPTER 1- INTRODUCTION AND LITERATURE REVIEW

1.1 Fretting Corrosion

Fretting corrosion is a phenomenon that takes place because of chemical reactions and mechanical stresses; predominately because of chemical reactions (Waterhouse, 1972). Fretting corrosion takes place at the interface of two surfaces compress together when they start to repeatedly slip. Slipping is defined as oscillatory motion, with small amplitude, which is caused by various mechanical stresses and magnetic forces. Usually the loads that cause slipping are mechanical vibration and/or differential thermal expansion; although some research has shown that magnetic forces also cause slipping (Xie, 2006). While slipping is taking place at the interface, chemical corrosion (usually oxidization) takes place as well. The mechanics on how chemical corrosion takes place during fretting corrosion will be further explained in the next section.

The after effects of fretting corrosion are "pits or grooves" at the interface along with various "corrosion products" surrounding it (Fontana, 1986). If one or both of the materials contain iron, "reddish brown debris" is found (Williams, 2005). Not only is the color of the debris unattractive (Figure 1-1), fretting corrosion is extremely detrimental object for two reasons: The original dimensions and tolerances are no longer satisfied, and the debris could cause seizing for moving parts.

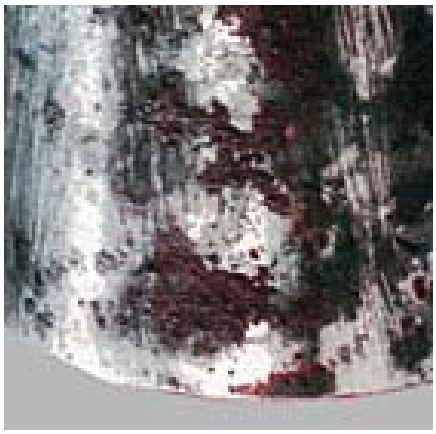

Figure 1-1 Photograph of Debris Caused by Fretting Corrosion (www.oerlikon.com)

This phenomenon has caused severe problems in multiple fields ranging from the biomedical (Geringer, 2005) to aerospace to construction fields. Fretting corrosion, causing the loosening of the femoral stem is one of the reasons artificial hips have to be replaced after nine years. Multiple bridges have collapsed due to fretting corrosion at key areas of the bridge design; two in particular are the Silver Bridge, and the Mianus River Bridge (Majzoobi, 2009). Due to its importance and its effects, fretting corrosion is one of the areas being investigated at the Corrosion Technology Laboratory at the NASA Kennedy Space Center. According to the lab's website (corrosion.ksc.nasa.gov) "The cost of corrosion to the USA is a $276 billion/year".

Environmental parameters have been tested to find how they affect fretting corrosion. One of the parameters is the chemistry in the surrounding environment; Nitrogen speeds up the rate in which fretting takes place (Xie, 2006). As can be seen later, frequency is inversely proportional to the amount of fretting. Some parameters are directly proportional to the rate at which fretting corrosion takes place. Those parameters include the amplitude of slippage, the number of cycles slippage takes place and normal load (load that keeps the two surfaces compressed) (Waterhouse, 1972).

1.2 Mechanism of Fretting Corrosion

As was stated in section 1.1, fretting corrosion takes place when two surfaces that are in compression start slipping. Due to the slipping, chemical reactions start to take place, and in fact dominate the process. If the slipping occurs on metallic surfaces, oxidation will take place. There are two theories that explain how oxidation occurs; those mechanisms are called wear-oxidation and oxidation-wear theories. Both theories are illustrated in the Figures below.

Figure 1-2 illustrates the wear-oxidation theory. As shown in Figure 1-2, frictional force breaks the contact points (peaks of the asperities), causing particles to oxidize. The oxidation-wear theory is shown in Figure 1-3, and as can be seen it is the opposite of wear-oxidation theory. It can also be seen that wear-oxidation theory takes place first followed by oxidation-wear; and it oscillates from there between the two theories (Fontana, 1986).

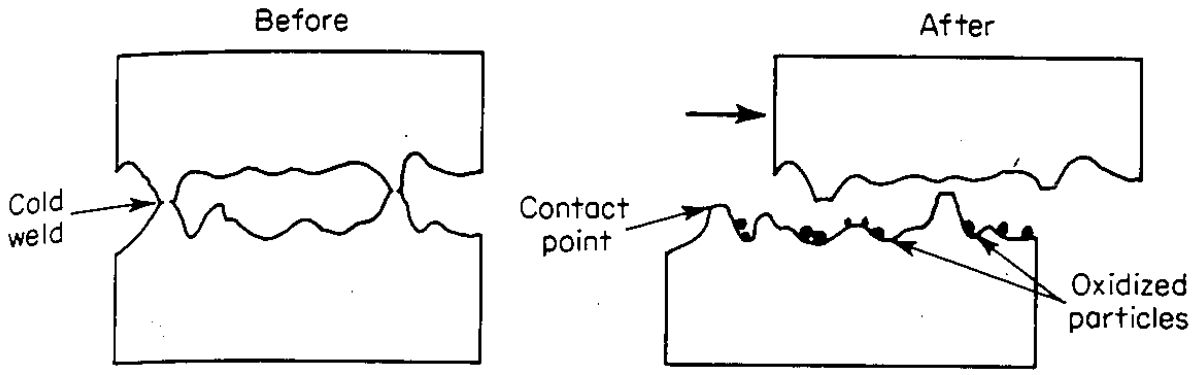

Figure 1-2 Diagram Displaying the Mechanics of Wear-Oxidation Theory (Fontana, 1986)

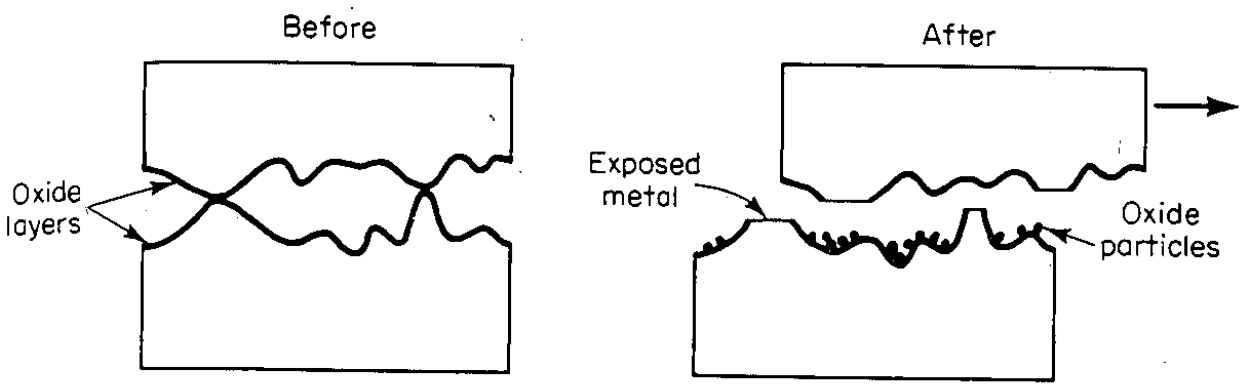

Figure 1-3 Diagram Displaying the Mechanics of Oxidation-Wear Theory (Fontana, 1986)

1.3 Literature Review of Parameters that Governed the Static Coefficient of Friction

Static friction has always played a key part in many engineering applications, whether it is as simple and conventional as a bolted joint member (Karamis et al., 1993) or a static seal (Xie, et al., 2000) or as complicated and new as a compliant electrical connector (Etsion et al., 1994) or a MEMs device (Gao et al., 2002). The same principle that binds these applications has been developing now for over 300 years. As expected the list of researchers who have investigated is long, but only a few will be focused on: Charles Augustin de Coulomb (Richard, 2000), D. Tabor (Tabor, 1981), W. R. Chang , Izhak Estion, D.B. Bogy (Chang et al., 1988), John Dunkin, and Dae Kim (Dunkin et al. 1996).

1.3.1 How the Static Coefficient of Friction is Governed by Pressure/Normal Load

In 1785, Coulomb developed a model that represents the frictional force (F_f) in terms of the relative velocity *v* and the Coulomb friction *F* (Richard, 2000):

$$F_f = F\ sgn\ (v) \qquad [1]$$

Where the signum function is:

$$sgn(v) = \begin{cases} 1, & v > 0 \\ 0, & v = 0 \\ -1, & v < 0 \end{cases} \quad [2]$$

This model has two major drawbacks:

1. It does not accurately give a physical representation of the behavior near zero velocity.
2. It is difficult to create a computer simulation because of the sudden non-linearity at zero velocity. Models using the Coulomb approach are prone to oscillate around zero velocity.

In 1981, Tabor outlined three findings dealing with friction of dry solids (Tabor, 1981). Those elements are:

1. The real area of contact between mating rough surfaces
2. Concluding that adhesion was the type of bond formed when interference occurs; also finding out the strength of the bond.
3. Analyzing how the contacting region was sheared and damaged during sliding.

The expression to quantify these three elements is:

$$\mu = \frac{Q_{max}}{F} = \frac{Q_{max}}{P - F_s} \quad [3]$$

where μ is the static friction coefficient, F is the external force, P is the real contact load, F_s is adhesion (which is also known as intermolecular forces), and Q_{max} is the tangential force needed to shear the contact points.

In 1988 Chang, Etsion, and Bogy, used the three principles Tabor outlined to develop what became known as the CEB model (Chang et al., 1988). The CEB model used a statistical representation of surface roughness to calculate the static friction force, while accounting for normal preloading. The CEB statistical model uses the plasticity index which is very instrumental in finding a mathematical function representing the static friction coefficient as a function of dimensionless pressure. The CEB model also took into account the change in surface energy ($\Delta\gamma$). Figure 1-4 displays that the static friction coefficient decreases as both the plasticity index and the dimensionless external force increase.

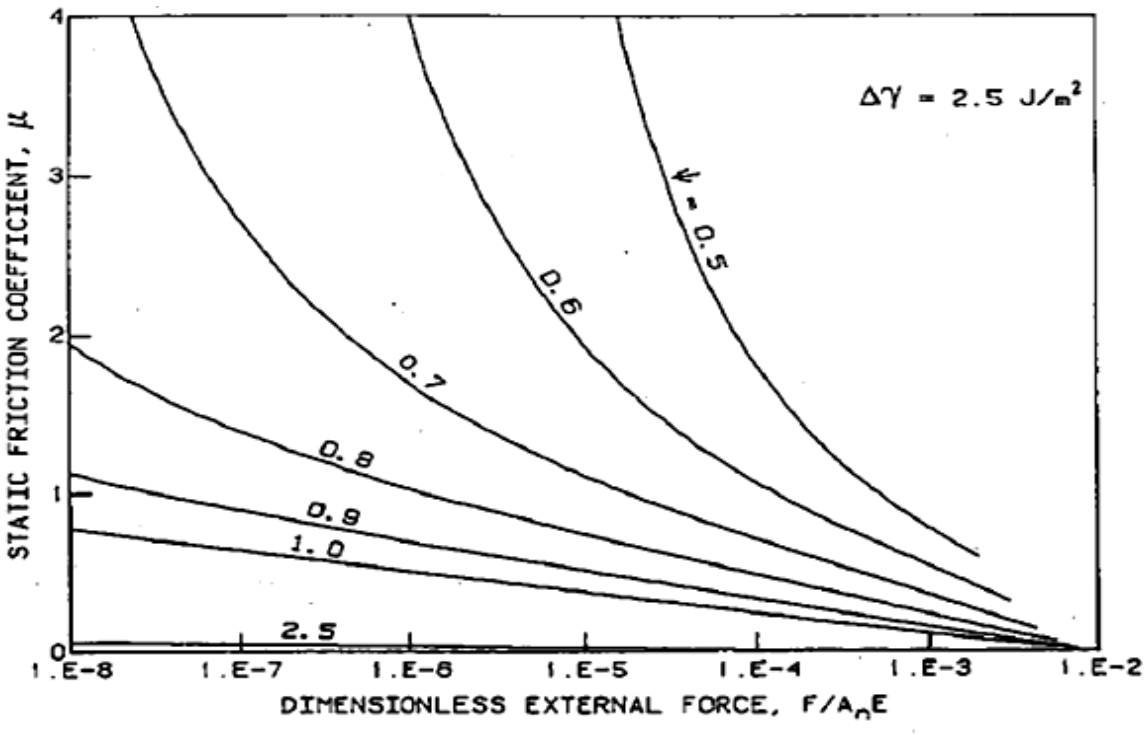

Figure 1-4 CEB model results when the surface energy is equal to 2.5 J/m^2 (Chang et al., 1988)

In 1994, Dunkin and Kim designed a Centrifugal Friction Apparatus (CFA), as shown in Figure 1-5, that was designed to measure the static friction coefficient between flat surfaces with low normal forces (Dunkin et al. 1996).

The CFA is used to find the effect of the following conditions on the static friction coefficient:

- Varying the normal load, while keeping the real contact area constant
- Varying the real contact area while keeping the normal load constant
- Solid lubricant and abrasive particles between surfaces
- Sliding for long distances under light loads.

The first two bullets fit the objective of this project; the results of each are shown in Figures 1-6 and 1-7.

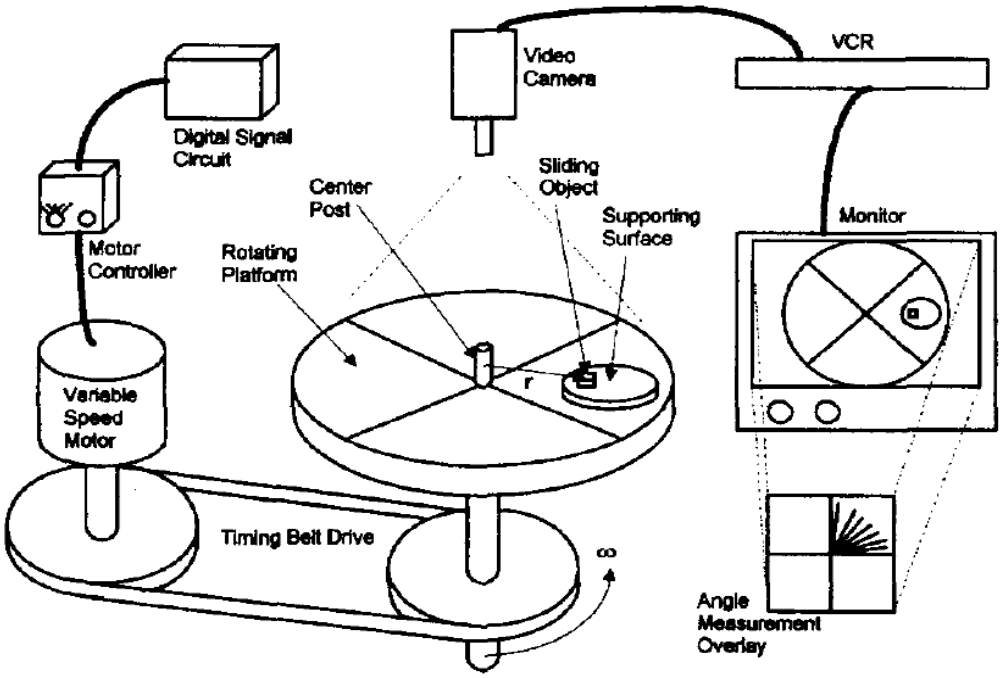

Figure 1-5 CFA used by Dunkin and Kim, 1996

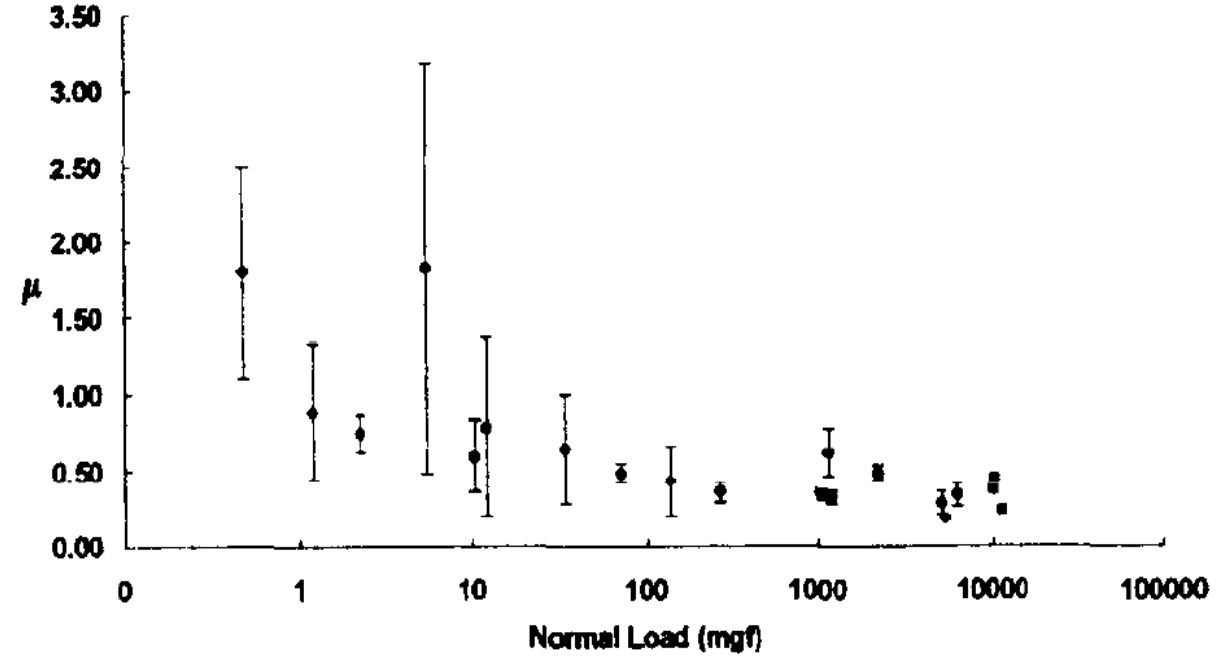

Figure 1-6 Results from the CFA of the Normal Load versus the Static Friction Coefficient (Dunkin and Kim, 1996)

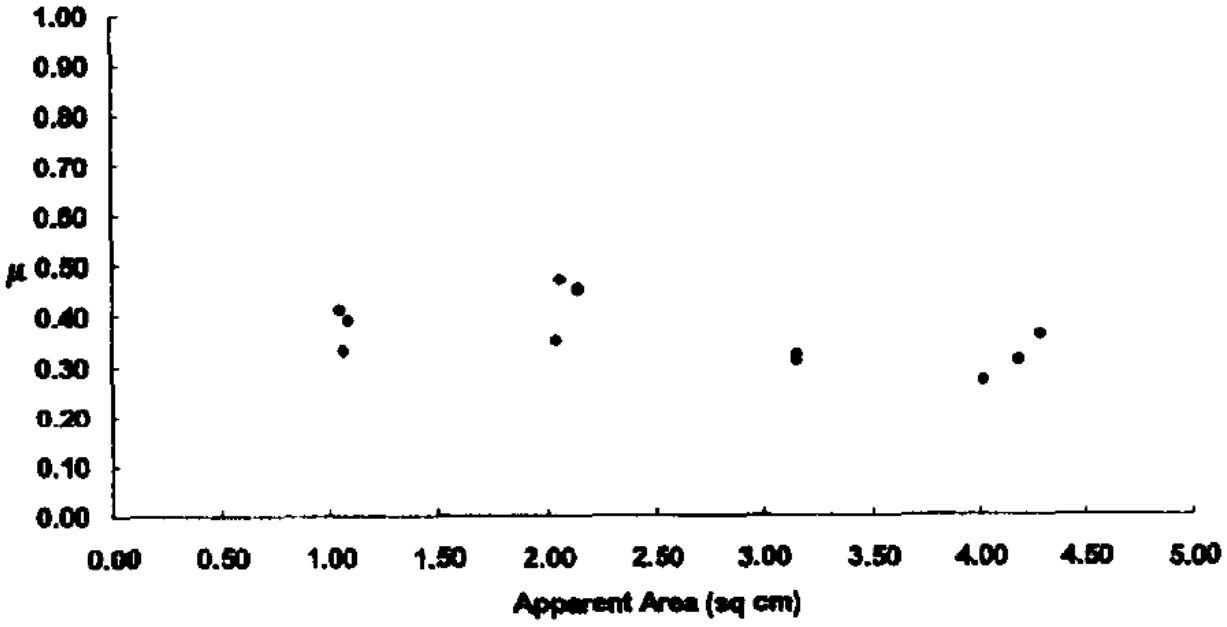

Figure 1-7 Results from the CFA of the Apparent Area versus the Static Friction Coefficient (Dunkin and Kim, 1996)

1.3.2 How the Static Friction Coefficient is Governed by Temperature

Two models are now discussed which attempt to describe the relationship between the coefficient of friction and temperature. The simpler model was derived by L. Schneider in 1988. The more elaborate model was derived by Moufki, Molinari, and Dudzinski in 1998. The simpler model is:

$$\mu(T) = \mu_0 - a(T - T_0) \quad [4]$$

Where μ_0 is the friction coefficient at a specific reference temperature (T_0) and a is a constant that is obtained by experimental means (Schneider, 1988). In the Thuresson paper, (Thuresson, 2006) the constant that was used was $a=1\times10^{-4}\ °C^{-1}$. The friction coefficient ($\mu(T)$) decreases as the temperature rises significantly because the solid peaks of the asperities (causing contact points) turn into molten film. As the asperities turn into molten film, frictional stress is no longer based on the shear stress of asperities, but on the viscous shear stress on the film.

The more elaborate model was derived so the process of orthogonal cutting could be investigated using analytical means (see Figure 1-8). The following assumptions are used to simplify the equation (Moufki et al., 2004):

1. The cutting edge is sharp
2. The flank contact is neglected
3. The heat flow through the tool surface is neglected
4. Conduction is neglected in the flow direction; but only with respect to the heat convection due to material flow.

The equation was derived postulating Coulomb's Friction Law with a mean friction coefficient ($\bar{\mu}$) that is dependent of the mean temperature ($\bar{T}_{int}$).

$$\bar{\mu} = \bar{\mu}(\bar{T}_{int}) \quad [5]$$

From there the following temperature distribution was derived:

$$\bar{T}_{int} = \frac{\bar{\mu} P_0}{\sqrt{\pi k \rho c}} \sqrt{V_C l_C} \sum_{i=0}^{\xi} \frac{2}{2i+1} C_{\xi}^{i} \left(\sum_{j=0}^{\xi-1} (-1)^j C_{\xi-i}^{i} \frac{2}{2(i+j)+3} \right) + T_1 \quad [6]$$

The friction coefficient is based on temperature distribution at the interface, which is shown in Equation 7:

$$\bar{\mu}(\bar{T}_{int}) = \bar{\mu}_0 \left(1 - \left(\frac{\bar{T}_{int}}{T_f} \right)^q \right) \quad [7]$$

where:

- T_f is the melting temperature of the workpiece material
- q is a constant found by experimental means
- $\bar{\mu}_0$ is a constant found by experimental means
- P_0 is the pressure of the tool tip
- V_C is the chip velocity
- l_C is the chip tool contact length
- T_1 is the temperature at the outflow of the primary shear zone
- k is the thermal conductivity of the workpiece material
- ρ is the density of the workpiece material
- c is the specific heat of the workpiece material
- i is the index in the r direction

- j is the index in the y direction
- ξ is a parameter that controls the pressure profile
- $C_{\xi}^{i} = \frac{\xi!}{(\xi - i)!i!}$

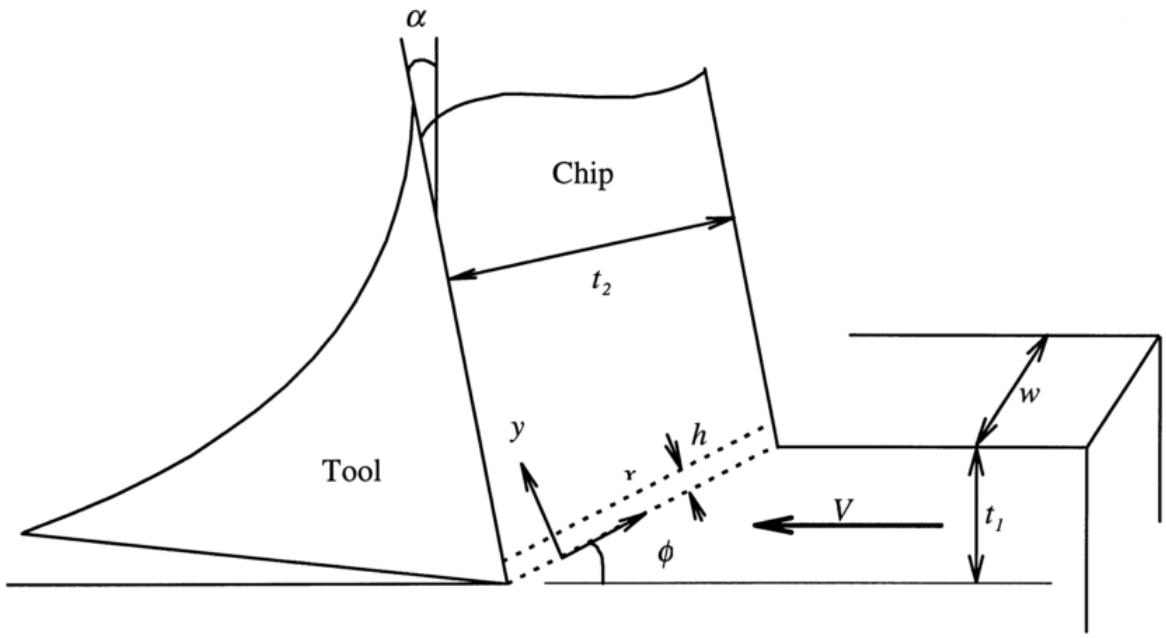

Figure 1-8 Diagram of the Workpiece and Location of Variables used in Equation 6 (Moufki et al., 2004)

1.4 Literature Review of Fretting Corrosion in Electrical Contacts

1.4.1 Computational Modeling

Over the years, finite element analysis has been developing into an extremely extensive and valuable field. The cost of both time and money reduces significantly when finite element analysis is used over conventional experimental means. Various programs and finite element packages are used to determine the physical characteristics of fretting corrosion.

In 1996, a group of researchers from the Ford Company (Villeneuve, Kulkami., Bastnagel, and Berry) used finite element analysis to simulate the terminal crimping process for a connector specially designed to be in automobiles. The model consisted of the terminal grip cross section, the punch tooling, and the wire strands. In order to imitate the actual process as closely as possible, the grip was "forced" into the punch, while which was placed on the anvil (Chen, 2009). The results produced by the model showed that in order to get a "good" crimp, friction between the grip surface and the punch surface is crucial (Villeneuve et al., 1996).

Monnier, Froidurot, Jarrige, Testé, and Meyer (Monnier et al., 2007), published a paper in 2007 describing how by using finite element analysis one is able to combine the mechanical, electrical and thermal aspects of the model to simulate the behavior of a sphere- plane electrical contact while high current is flowing through it. Multiple mathematical expressions where used in order to construct this model which was then validated by experimental means. This model was able to provide additional information that could not be found experimentally, such as the contact resistance, the terminal voltage, and the solid inner temperature.

In 2008, Angadi, Wilson, Jackson, Flowers, and Rickett published a paper modeling the bulk region of an electrical connector. The multi-physics model included the structural,

electrical, and thermal aspects of the bulk region. Using a MATLAB™ code that ANSYS™ can read, a multi-scale sinusoidal rough surface (MSRS) was the foundation of the multi-physics model. The model was used to predict how the connector performed under a specific current range. The results showed that the relationship between the voltage drop and temperature was proportional across the bulk regions. That relationship showed that the multi-physics model, combined with the MSRS model, predicts contact forces, electrical contact resistance, and thermal contact resistances more accurately (Angadi, 2008).

Xie, Flowers, Chen, Bozack, Suhling, Ricket, Malucci, and Manlapaz, (Xie et al., 2009) published a paper in 2009 that showed that finite element analysis and experimental results (see 1.4.2.1) of the blade/receptacle connector pair can be compatible. The program used in constructing the finite element program was ANSYS™. For simplicity and computational time, a 2-D model was used instead of a 3-D model. The model consisted of a receptacle, blade, U-bend portion of the cantilever beam, and wire portion outside the crimp. Supplementary masses are used to decrease the natural frequency so that fretting corrosion could be more evident at lower frequencies. The results from both the finite element model and the experiment ended up being compatible.

1.4.2 Experimental-Parametric Studies

Experiments have been used to investigate various parameters to see how it affects fretting. Some of the following parameters have been investigated since the early 1950's: number of cycles, normal load, amplitude of slip, vibration frequency, thermal cycling, etc. There is one paper that stated that there might be as many as fifty variables that effect fretting corrosion (Attia, 1992). This thesis is focusing on how vibration and thermal cycling affects

fretting corrosion. In most cases the experimental results are put in terms of contact resistance. The higher the contact resistance, the more probable, fretting corrosion takes place.

1.4.2.1 Relative motion/Vibration cycles

Lee and Mamrick published a paper in 1987 that explained an experiment that was conducted. The relative motion was created by a "stepper motor/precision stage assembly" (Lee and Mamrick, 1987) (See Figure 1-9), while electrical current was flowing through the electrical contacts. The two currents tested were: 0.853 mA and 0.093mA. It was observed that the higher the current the faster the contact resistance rises. Also in both cases the contact resistance eventually leveled off. The other observations that were found are:

1. Electrical load does not affect fretting corrosion during the "first few tens cycles".
2. After 200 cycles, it is evident that the higher the current the higher the contact resistance
3. Plateaus in contact resistance delay fretting corrosion therefore corrosion characteristics are altered.
4. To keep the contact resistance plateaus low, use higher current; to make the contact resistance plateaus last for more cycles, increase the voltage.

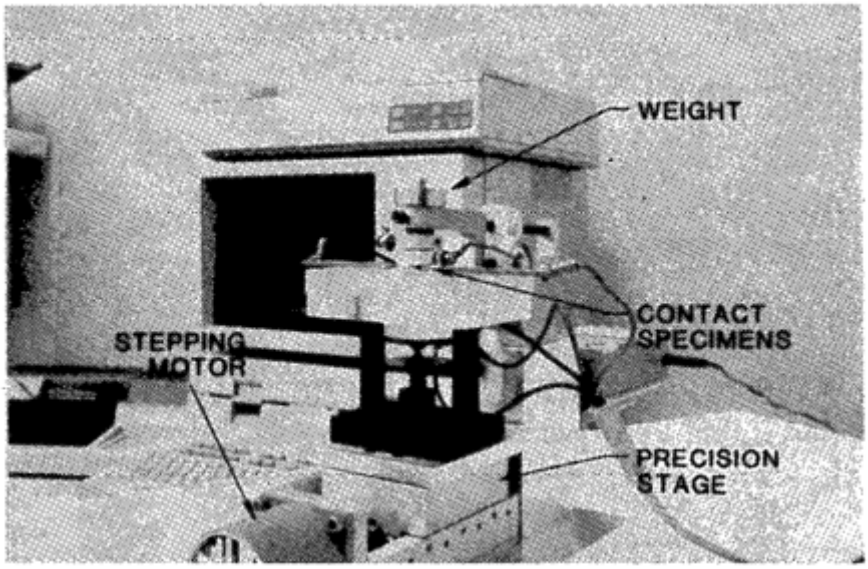

Figure 1-9 Experimental Setup Used by Lee and Mamrick, 1987

Up until 2004, periodic relative motion (vibration) was induced by mechanisms that moved horizontally. Flowers, Xie, Bozack, and Malucci published a paper (Flowers et al., 2004) which described an experiment performed where the vibration was induced vertically using a shaker. The basic test article that was used on the shaker was a 25-pin connector (see Figure 1-10). The theoretical model used the transfer matrix (Myklestad-Prohl) Method (Vance, 1987). The initial frequency of the experiment was tested was 36 Hz and it was tested at various excitation levels (g-level). It was found that as excitation level increased, the rate of contact resistance increased as well. As the frequency increased, the excitation level and displacement (vertical motion) needed for fretting to take place decreased.

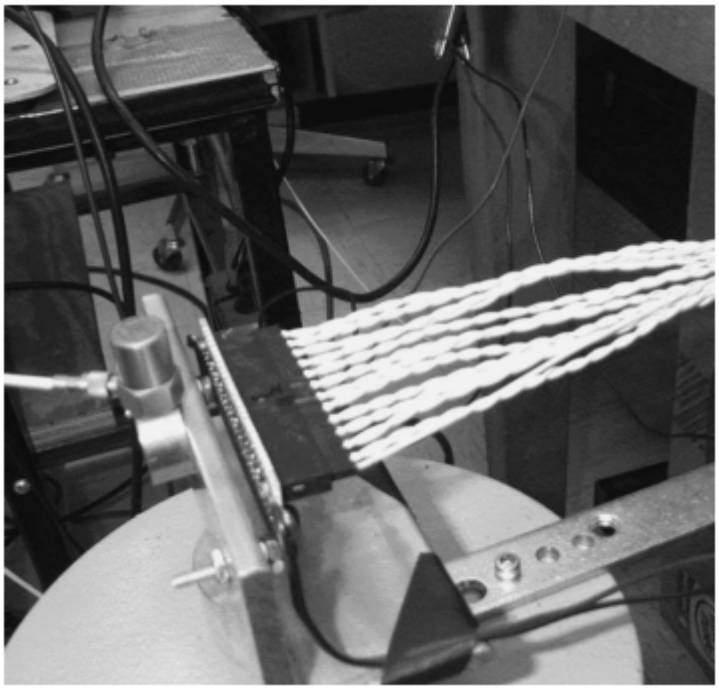

Figure 1-10 Experimental Setup Used by Flowers et al., 2004

To confirm the accuracy of results obtained by Flowers et al. 2004; another experimental setup was constructed (see Figure 1-11) and the results were later published in 2006. Flowers et al. (2006) used the experimental setup in Figure 1-11 to investigate how random vibration effects fretting corrosion. Sixteen samples underwent sinusoidal frequencies between 50 and 100 Hz for 100 seconds. The relative amplitude between the two ends of the connector becomes a function of the input frequency at G-levels above the threshold. The transfer function is a function that relates the input frequency to the G-levels that were determined by the relative amplitude. The results showed that the model constructed and the experiment conducted exhibited a "high degree of consistency" (Flowers et. al, 2006).

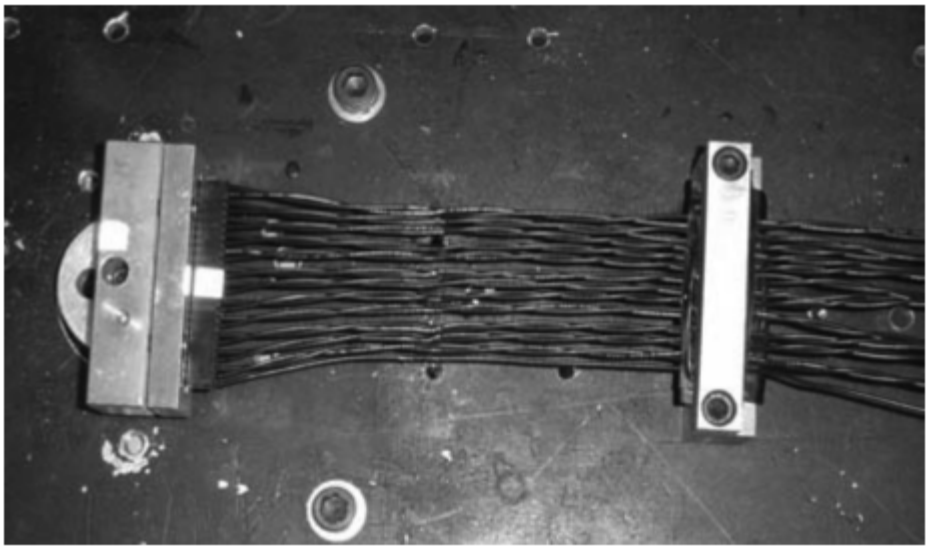

Figure 1-11 Experimental Setup Used by Flowers et al., 2006

So that computational and experimental methods could be compared, reducing the number of connectors that being tested needed to be reduced to one. In 2007, Xie et al. published a paper comparing the two methods (the computational model will be described in 1.4.1). The three steel balls (shown in Figure 1-12) is the supplementary mass used to lower the natural frequency. That is needed reasoning because the lower the frequency, the more evident fretting corrosion takes place.

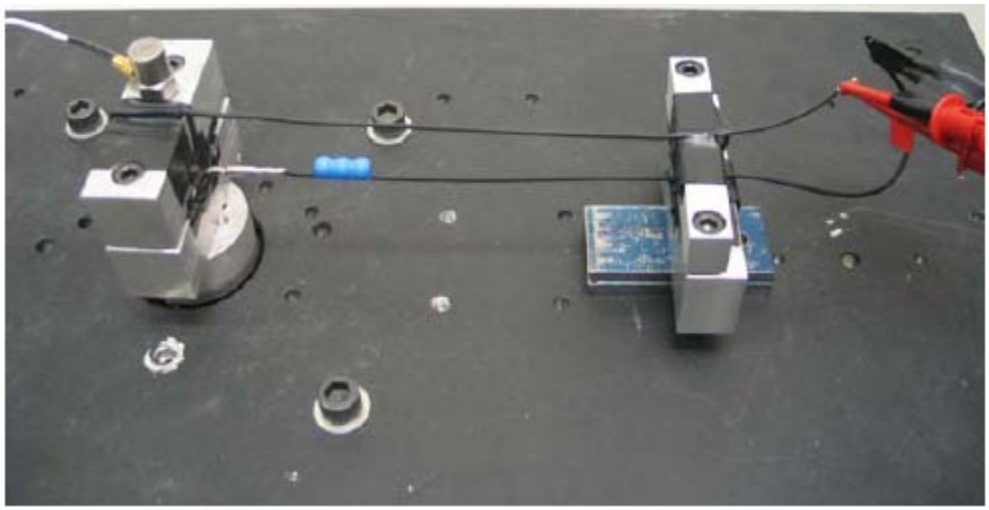

Figure 1-12 Experimental Setup Used by Xie et al., 2007

In 2008 Park, Narayanan, and Lee conducted experiments with the purpose to find "the development of fretting corrosion maps for life-time prediction and the effectiveness of lubrication as a preventive strategy it increases the life-time of tin plated contacts" (Parks et al., 2008). The range of each variable tested is listed in Table 1-1. The material tested was made out of a copper alloy with the following chemical makeup: Ni-1.82%, Si-0.75%, Zn-0.01%, Sn-0.37%, and the reminder Cu; electroplated with a tin layer with a thickness of 3 μm. The tests, using the experimental setup in Figure 1-13, were conducted under gross-slip conditions. After the experiment, both the surface profile and roughness along the fretting area was processed using a Carl Zeiss laser scanning microscope. With the following initial conditions set: temperature at 22 °C, amplitude at ±25 μm, normal load at 0.5 N, and current at 0.1 A; it was found that the contact resistance increased at a faster rate, the lower the frequency. Under another setup, the initial conditions set were: temperature at 22 °C, frequency at 10 Hz, and normal load at 0.5 N, and current at 0.1 A; it was found that the contact resistance increased at a faster rate, the smaller the amplitude.

Table 1-1 Variables that Changed During Experiment Conducted by Park et al., 2008

Variable	Range
Frequency	3, 5 ,7, 10, 15, 20 Hz
Amplitude	±5, ± 25, ±50, and ± 90 μm
Normal Load	0.1, 0.5, 1 and 2 N
Temperature	27 °C, 55 °C, 65 °C, 75 °C, 85 °C, 105 °C, 125 °C, 155 °C, and 185 °C
Humidity	20-45% RH, 45-75% RH, >85% RH
Current Load	0.1 A, 0.5 A, 1.0 A, 1.5 A, 2.0 A, and 3.0 A

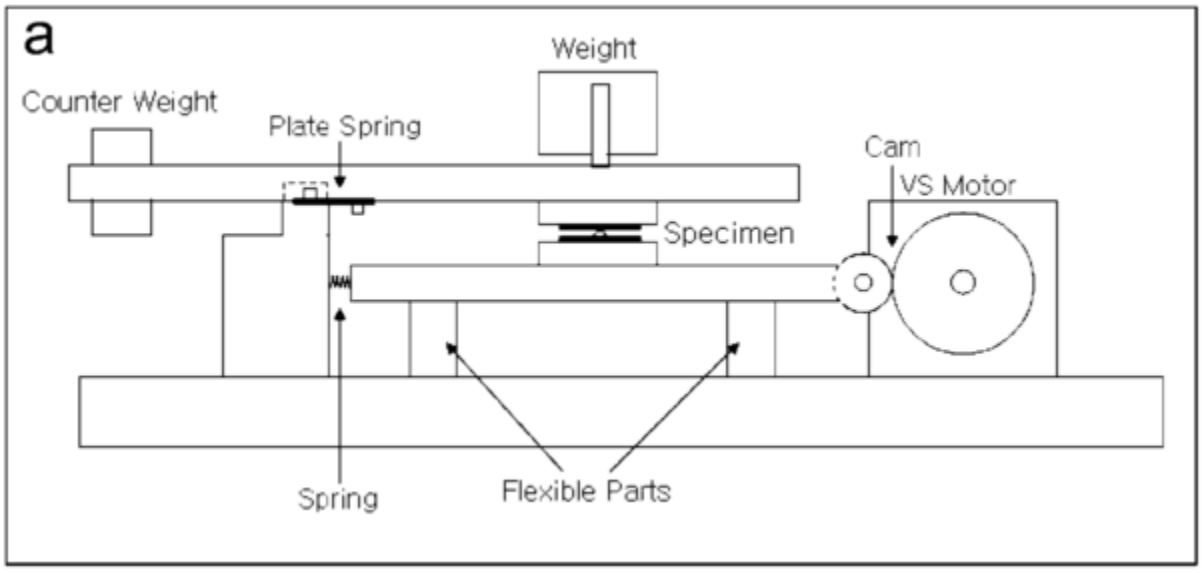

Figure 1-13 Experimental Setup Used by Park et al., 2008

1.4.2.2 Thermal shock/cycles

Bock and Whitley presented a paper in the 1974 Holm Conference that showed how thermal cycling effected fretting corrosion (Bock and Whitely, 1974). Two fixtures were made for this experiment; one was exclusively made of steel and the other of a combination of nylon and steel. The combination nylon and steel fixture was made so that translation motion between the nylon and the steel could take place, 0.75mm $°C^{-1}$; the steel fixture was made so that there would be negligible translation would take place. The fixture was placed in a temperature chamber, where the temperature difference (ΔT) is 5 °C (55 °C to 60 °C). The fixture and samples (bright tin and nickel plated) were each subjected to temperatures at 60 °C for 45 minutes and 55 °C for 15 minutes. The normal forces put on the samples are: 784.8 N, 981 N, and 4414.5 N. Both types of samples (tin and nickel) experienced high contact resistance after 100-200 cycles.

A few years later Kongsjorden, Kulsetås, and Sletbak (Kongsjorden et al., 1979) developed another method to show how differential thermal expansion plays apart in fretting corrosion (see Figure 1-14). Instead of placing the contacts in a temperature chamber, they used other methods to simulate thermal expansion. The heating element connected to the aluminum rod changed the length of the rod, causing relative motion of contact members which was measured by an inductive transducer. Normal force is applied by adding mass to a pan; the normal loads ranging from 20 N to 170 N are used. The results showed that the contact resistance decrease as the normal load increases. Also, the results showed that as the change in temperature increased (causing the slippage amplitude to become larger) the contact resistance decreased.

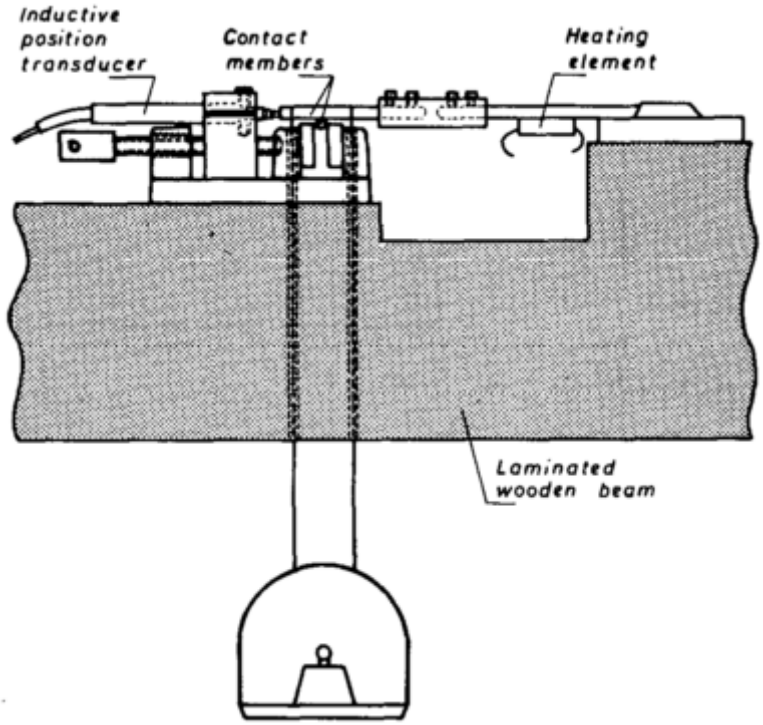

Figure 1-14 Experimental Setup Used by Kongsjorden et al., 1979

The experiment that Lee and Mamrick conducted and later published in 1987 was expanded upon to include how temperature affects fretting while vibration is taking place. The test setup was very similar to that of the paper published in 1987 (Lee and Mamrick, 1987). The setup was heated with hot fluid that circulated in a reservoir inside the metal structure. The temperatures in which this was done at were: 35 °C, 60 °C, 85 °C, and 110 °C. Each temperature was tested at each of the following normal forces: 0.5 N, 1.0 N, and 2N. Other important conditions included:

- Fretting motion- amplitude 20μm and frequency 10 Hz
- Contact resistance- four wire, dry circuit (20 mV, 100 mA)
- Contact configuration-flat vs. 3mm diameter dimple formed from the same material
- Contact material- 3μm electro-plate matte tin over copper alloy CA65400

When the normal force was 0.5 N, the experiment concluded that from 35 °C to 60 °C the number of cycles needed till the contact resistance started to increase, actually decreased. But after 85 °C, the number of cycles needed for the contact resistance to increase, also increased. It should also be noted that, once the contact resistance starts to increase it increases at faster rate as the temperature increases. When the normal force was 1 N, the same trend took place; where the number of cycles needed to increase the contact resistance, decreased (until 110 °C), when the number of cycles needed to increase the contact resistance also increased (Lee and Mamrick, 1987)

Dr. Robert Malucci of the Molex Corporation noticed that the connectors they developed, performed well under "normal field conditions" (Malucci, 1999); but would fail when the connector was used in a high temperature environment. Four experiments were conducted to investigate whether it was the elevated temperature, the thermal cycling, or the humidity of the environment that caused the fretting corrosion, which produced a failure. Table 1-2 displays the types of experiments that were performed. The results ended up showing that humidity and elevated temperatures accelerate fretting corrosion; because as temperatures increase the amount of oxide also increases.

Table 1-2 Environment Parameters and Material Test in Malucci, 1999

Temperature Ranges	Dwell Time	Relative Humidity	Transition Time
25 °C to 70 °C	15 min	~	Instant
-40 °C to 105 °C	15 min	~	Instant
50 °C to 85 °C	15-30 min	90%	25/10 min
70 °C to 150 °C	30 min	~	Instant

In 2007 Park, Narayanan, and K. Lee published a paper (Park et al., 2007) describing an experiment is very similar to the experiment conducted by Lee and Mamrick (Lee and Mamrick, 1987). The differences are an updated experimental setup, the contact configuration and the temperature range tested. In Lee's experiment a 3mm dimple was used but in Park's experiment a 1.5mm dimple was used (the thickness of the material is 3mm for both, and the same material was used). The temperatures tested are: 25 °C, 85 °C, 125 °C, 155 °C, and 185 °C.

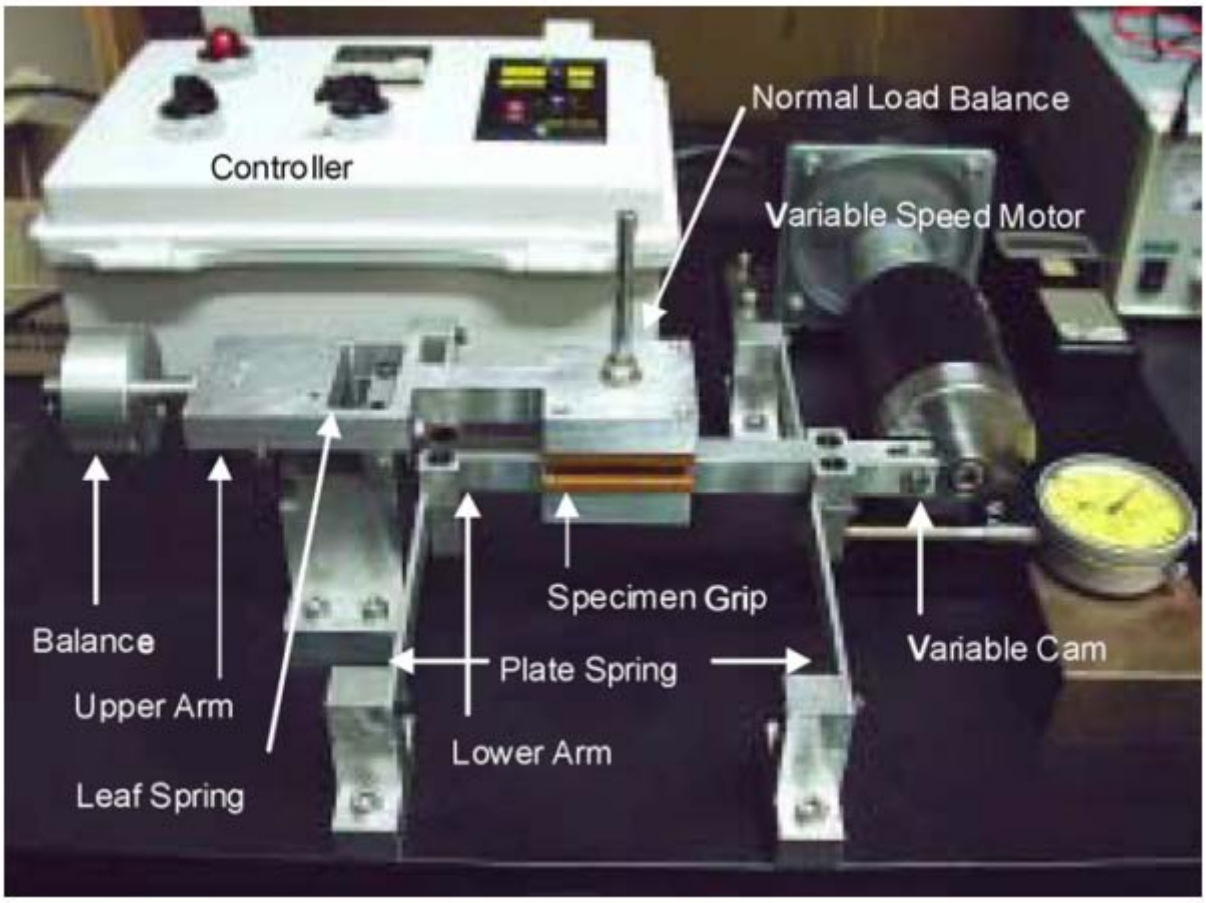

Figure 1-15 Experimental Setup Used by Park et al., 2007

The results from this experiment showed the same trend, from the same temperature 85 °C; but as the temperature increased to 125 °C the number of cycles needed to increase the contact resistance started to decrease again.

1.5 Overview of Work

This thesis discusses two experiments and two finite element programs which focus on fretting corrosion, while also discussing how different parameters affect fretting corrosion.

The thesis has been divided into four chapters. Chapter one is the literature review and introduction. It introduces the concept and mechanism of fretting corrosion and how pressure and temperature affect the static friction coefficient. This chapter has shown how the work has progressed in this field over the years.

Chapter two describes two experiments; both utilize the same apparatus. In the first experiment, static friction coefficient changes with pressure were evaluated using a weight set. The results from this experiment were compared to analytical results to demonstrate the suitability of the apparatus. In the second experiment, the static coefficient changes with temperature were measured by placing the apparatus in a temperature chamber. The results from the experiments provided input data for subsequent finite element models.

Chapter three describes the two finite element models. Both models were constructed in ABAQUS^{TM}. One model demonstrates how vibration cycling affects fretting corrosion at a specified temperature. The input material properties (coefficient of friction and elastic modulus) were temperature dependent. The second model illustrates how thermal cycling affects fretting corrosion. The input material properties were again temperature dependent including the: elastic modulus, friction coefficient, thermal expansion coefficient, thermal conductivity, and heat transfer coefficient.

Chapter four gives a summary and conclusions, as well as suggested future work.

CHAPTER 2- A STUDY ON THE PARAMETERS OF THE STATIC FRICTION COEFFICIENT

2.1) How Both Experimental Setups Relate to Each Other

Two experiments were performed to test how pressure and temperature affect static friction coefficient (μ) of tin plated copper on tin plated copper. Because the samples are made of tin plated copper and the plating will not be removed during the experiment, the static friction coefficient of tin on tin is being tested. One experiment used the apparatus shown in Figure 2-1, but the apparatus was placed in a temperature chamber. The results from this experiment will be entered in the ABAQUS^{TM} code (more information on how that was incorporated in the code in Chapter 3). And the other experiment was performed to test the effect of pressure on the static friction coefficient, with the purpose to compare the results obtained by experimental means (same experimental setup) to the analytical model that Cohen, Kligerman, and Etsion derived.

2.1.1) Experimental Setup/Apparatus

In Figures 2-1, 2-2, and 2-3 show the experimental setup and the close up of the inclined plane. Figures 2-4 and 2-5 show how the sample is adhered to the weight set, for both experiments. The mechanical drawings and electrical drawing of the setup are in Appendices A and B.

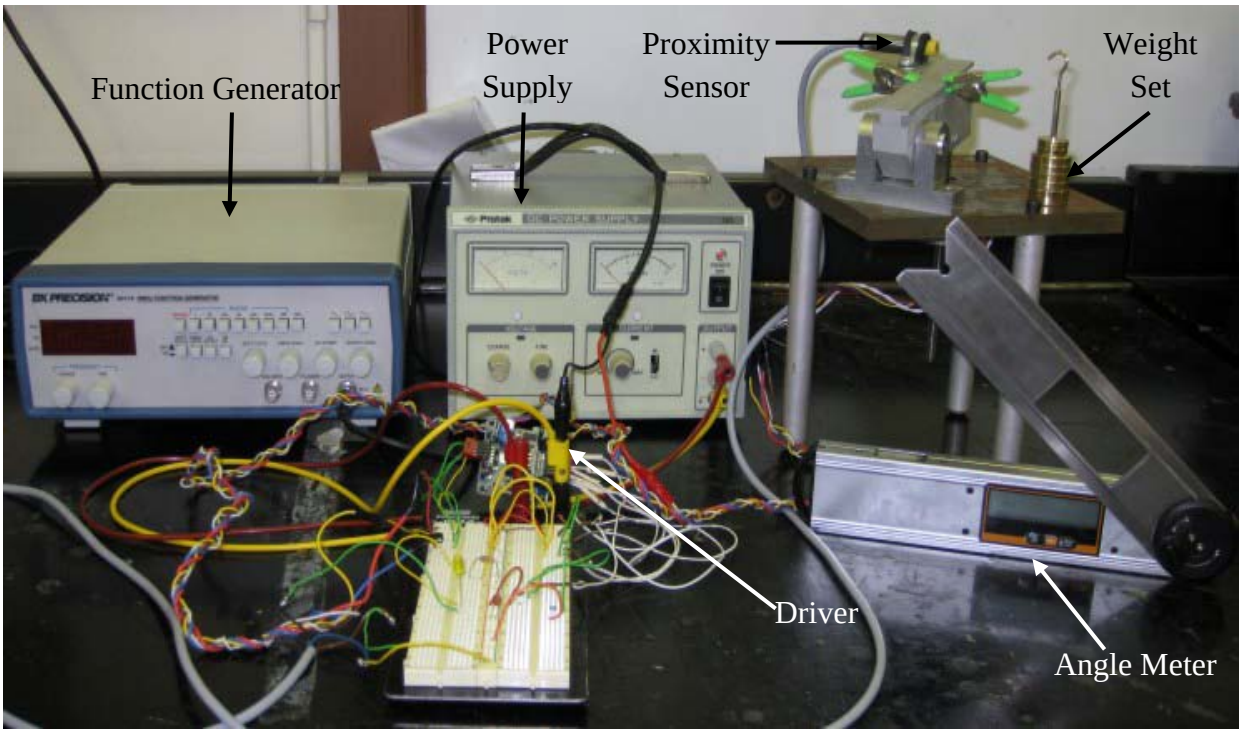

Figure 2-1 Experimental Setup

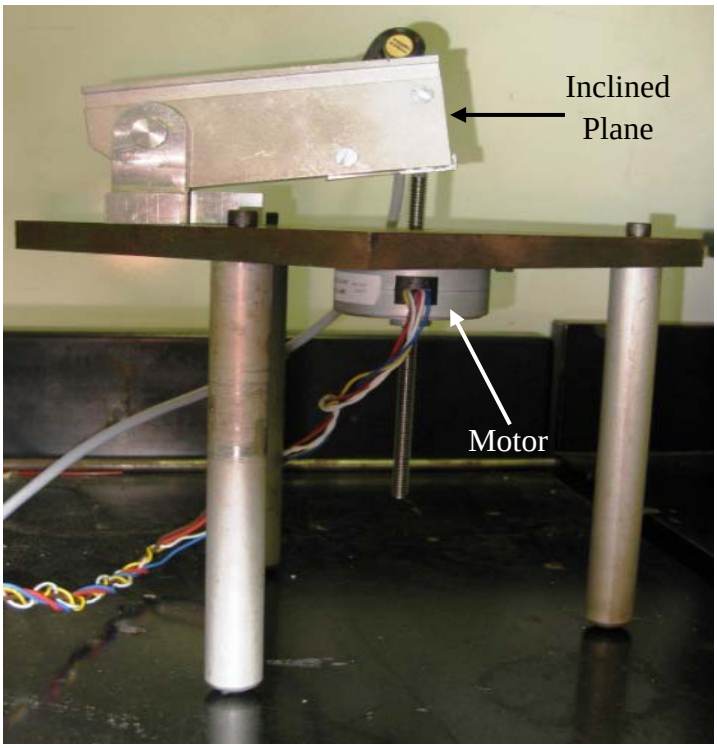

Figure 2-2 Inclined Plane of the Experimental Setup

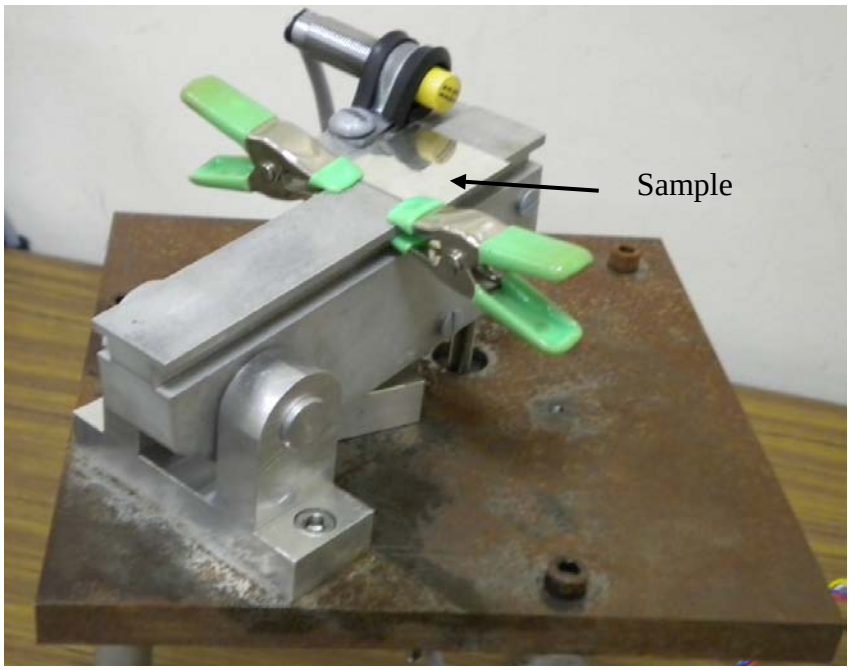

Figure 2-3 Sample Clipped on Inclined Plane

Figure 2-4 One of the Samples Used in Temperature Test Taped[1] on Weight Set

[1] Using double-sided tape to adhere the sample to the weight set.

Figure 2-5 One of the Samples used in Pressure Test Taped on Weight Set

The design uses the following hardware/materials for the following set up. This list also gives a brief synopsis of each function.

- Tin Plated Copper Samples: Material was used to determine the static friction coefficient of tin on tin.
- Aluminum: Used to make the inclined plane and base of the apparatus. Selected because it is easier to machine than other materials.
- Linear Actuator Stepper Motor: This particular DC motor converts rotational motion into linear motion, causing the inclined plane to steady increase its inclination angle theta (θ).
- Electrical Driver: Sends signal to the motor to either increase or decrease θ, or to stop the inclined plane from moving.
- Proximity Sensor: Used as a switch in the circuit. Once the sensor senses motion of the weight set, it sends a signal to the electrical driver to stop the motor.

- Function Generator: clock for the electrical driver.
- Power Source: Powering the motor and the electrical driver.
- Weight Set: To add and subtract the amount of weights needed to obtain the static friction coefficient needed at that particular non-dimensional force.
- Angle meter: Determines the angle θ of the inclined plane when desired. Takes away the additional measurements and potential errors of the x and y directions to obtain θ.

2.1.2) Theory Behind Experimental Setup/Apparatus

Using an inclined plane it is relativity simple to attain the static friction coefficient. By drawing a force body diagram (Serway, 2004):

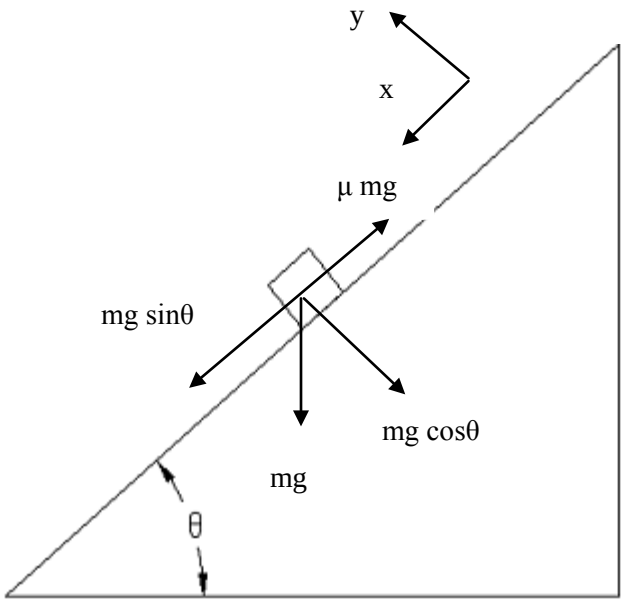

Figure 2-6 Force Body Diagram of the Experimental Apparatus

From Figure 2-6, it can be seen that Newton's Second Law is applied to write equations in the x and y directions respectively:

$$F_x = ma_x = mg\sin\theta - \mu N = 0 \qquad [8]$$

$$F_y = ma_y = N - mg\cos\theta = 0 \quad [9]$$

Using elimination it can be seen that Equation 9 can be rewritten as:

$$N = mg\cos\theta \quad [10]$$

And Equation 8 can be rewritten as:

$$F_x = mg\sin\theta - \mu\,(mg\cos\theta) = 0 \quad [11]$$

$$\boxed{\mu = \frac{mg\sin\theta}{mg\cos\theta} = \tan\theta} \quad [12]$$

2.2) How Static Friction Coefficient is Affected by Temperature

2.2.1) Experimental Setup

The same apparatus used to conduct the experiment discussed in Section 2.1, was placed in a temperature chamber to find out the effect of temperature on the static friction coefficient by taking readings at -10 °C, 10 °C, 25 °C, 50 °C, 75 °C, and 110 °C. Figures 2-7, 2-8, and 2-9 display all of the aspects of the experimental setup.

Figure 2-7 Experimental Setup Including Temperature Chamber

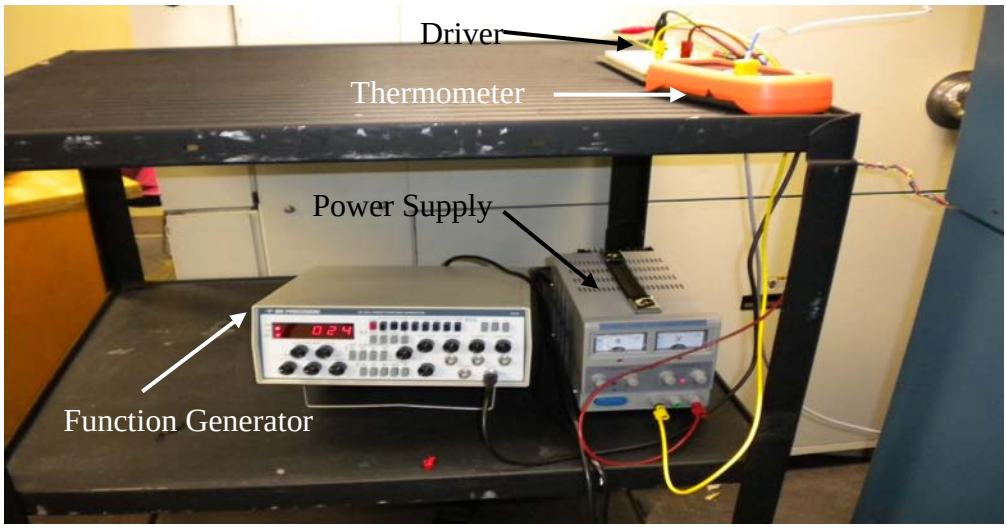

Figure 2-8 Experimental Setup Excluding Apparatus and Temperature Chamber

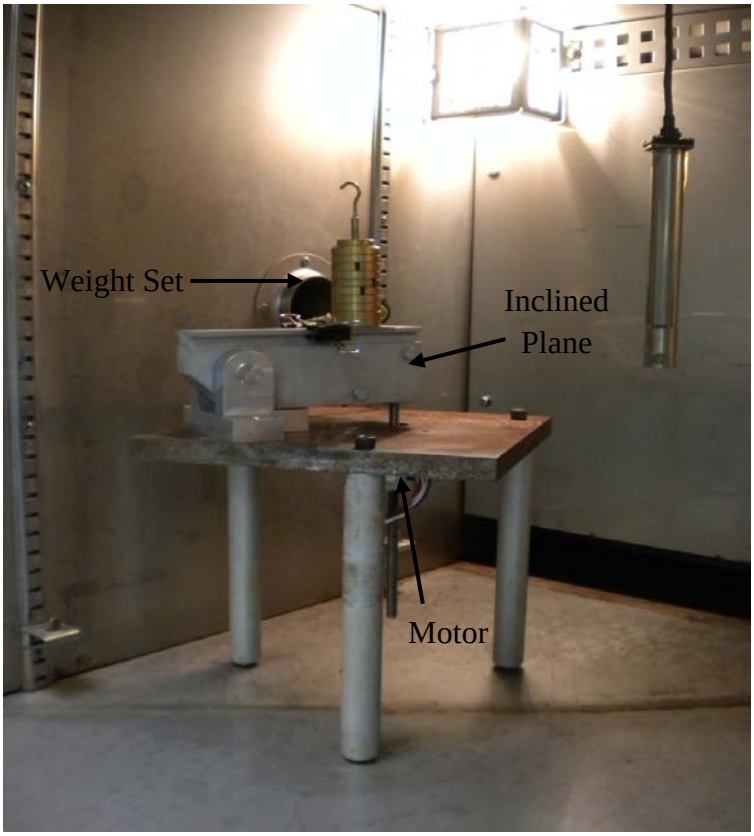

Figure 2-9 Experimental Apparatus in Temperature Chamber

2.2.2) Experimental Procedure and Parameters

Table 2-1 Summary of Experiment Parameters

Mass Minimum	70 g
Mass Maximum	220 g
Weight Increment	30 g
Temperatures Tested	-10 °C, 10 °C, 25 °C, 50 °C, 75 °C, and 110 °C
Nominal Contact Area	$5.067*10^{-4}$ m^2
Material Used	Sn

The experiment procedure used is described in the following sequence:

1) Start up apparatus
2) Set temperature chamber to desired temperature
3) Start with 70 g
4) Once the desired temperature in the chamber has been reached place weight set (with sample adhered to it) on inclined plane
5) Let motor increase the inclination angle of the inclined plane until slippage occurs
6) Repeat to verify the measurement
7) Record
8) Increase mass by 30 g
9) Repeat steps 4-8 till the maximum mass is reached
10) Change temperature
11) Repeat 1-10 till all temperatures and masses are tested

2.2.3) Experimental Results

Figures 2-11, 2-12, 2-13, 2-14, 2-15, and 2-16 show the experimental results obtained from the setup described in Section 2.1. Figure 2-10 summarizes how static friction coefficient is affected by both temperature and normal force. It can be seen, from the best fit lines in Figures 2-11 through 2-16 that as the temperature increases the static friction coefficient decreases. This is in agreement with previous work. According to Thuression, 2006: "A decreasing function for a coefficient of friction is in agreement of the thermal softening (brake fade) effects often seen in experiments". The use of these numbers will be discussed in Chapter 3.

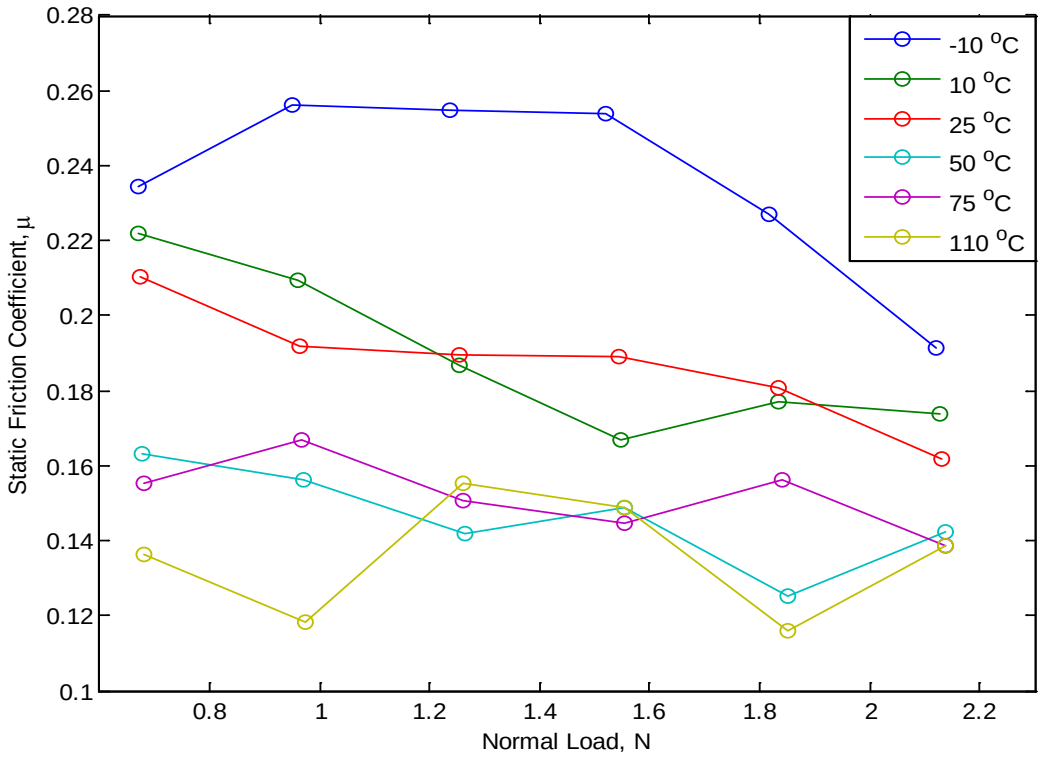

Figure 2-10 Static Friction Coefficient as a Function of Normal Force at Various Desired Temperatures[2]

[2] The uncertainty analysis done on the desired temperature can be found in Appendix C

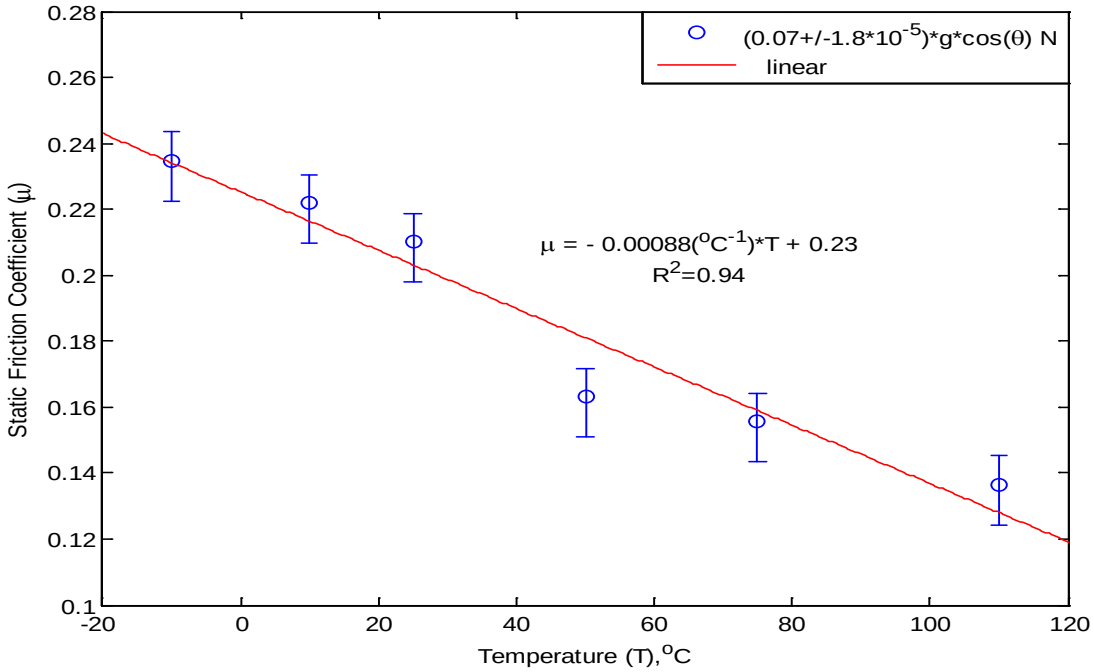

Figure 2-11 Static Friction Coefficient vs. Temperature with 70 grams Compressing the Samples[3]

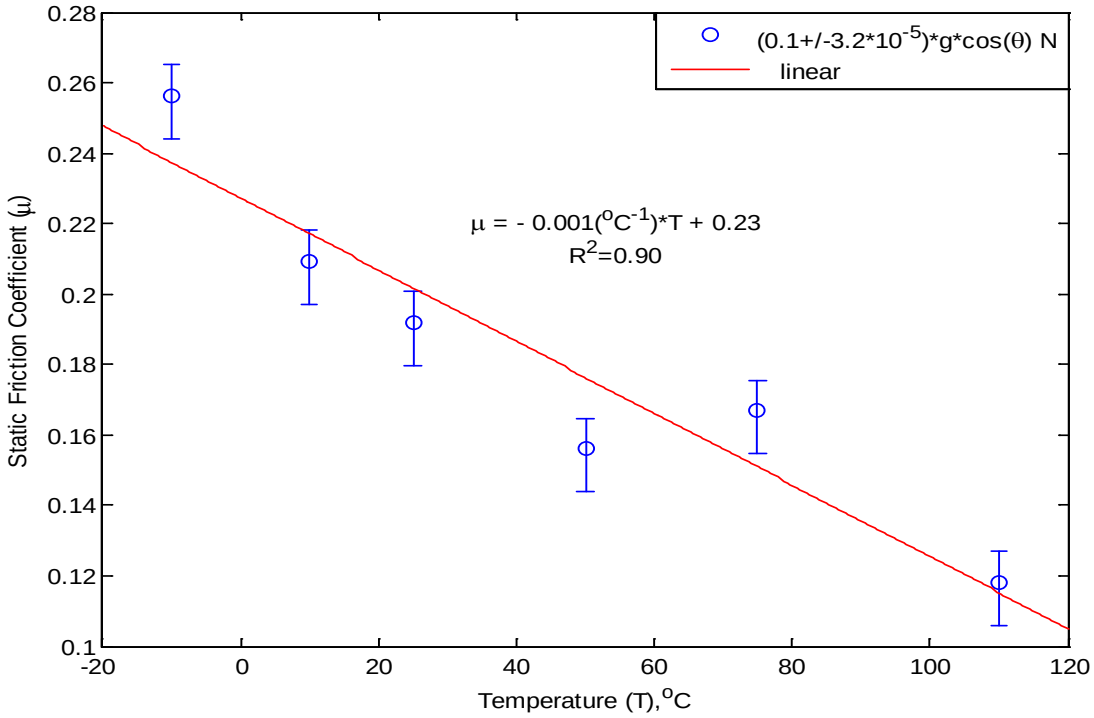

Figure 2-12 Static Friction Coefficient vs. Temperature with 100 grams Compressing the Samples

[3] Uncertainty Analysis can be found in Appendix C

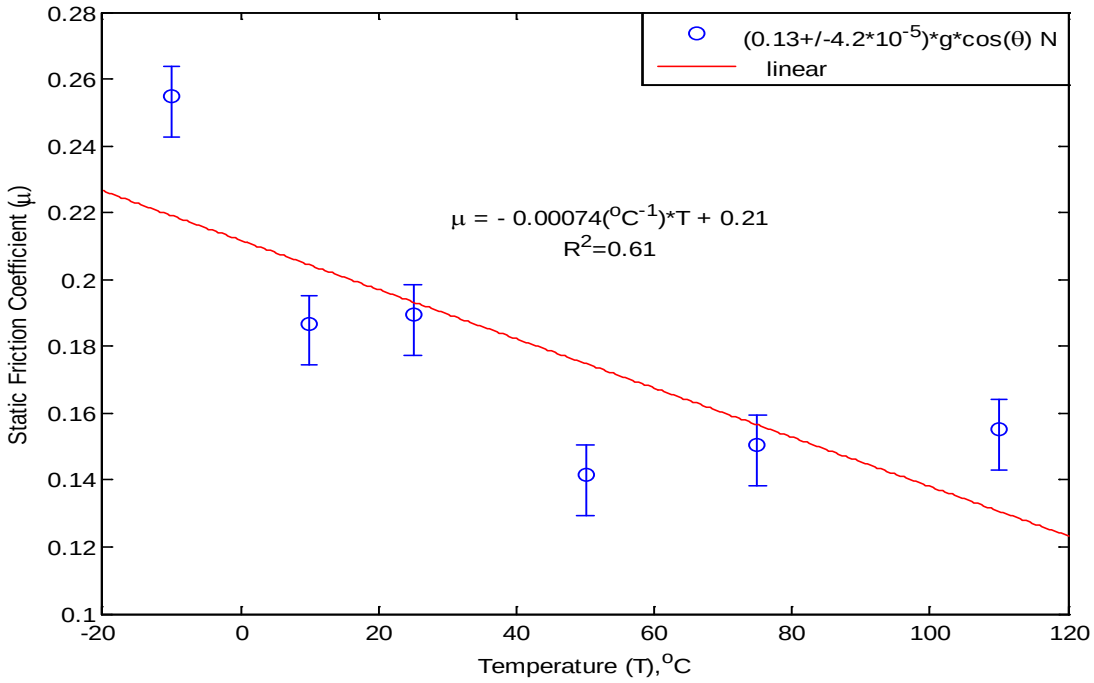

Figure 2-13 Static Friction Coefficient vs. Temperature with 130 grams Compressing the Samples

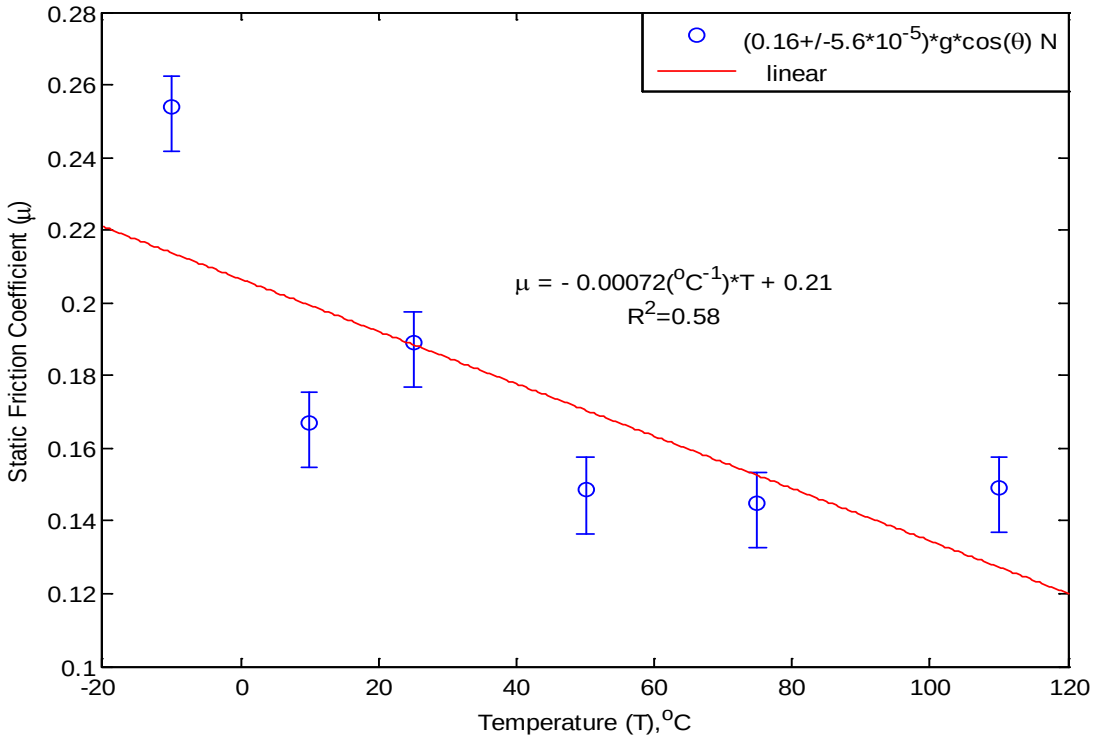

Figure 2-14 Static Friction Coefficient vs. Temperature with 160 grams Compressing the Samples

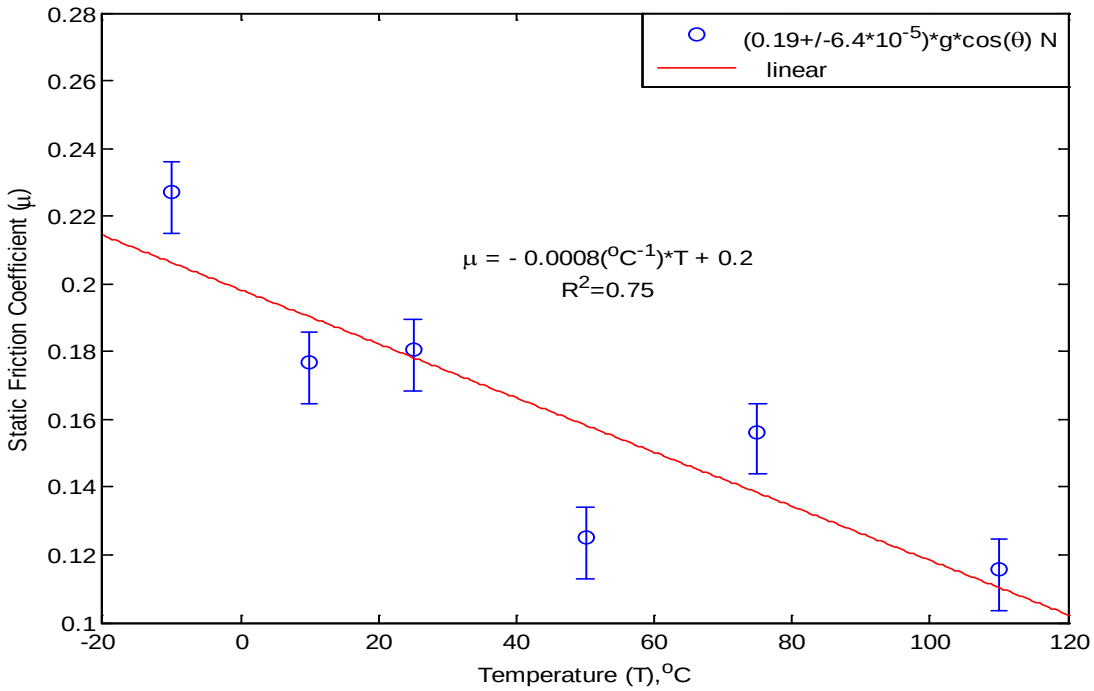

Figure 2-15 Static Friction Coefficient vs. Temperature with 190 grams Compressing the Samples

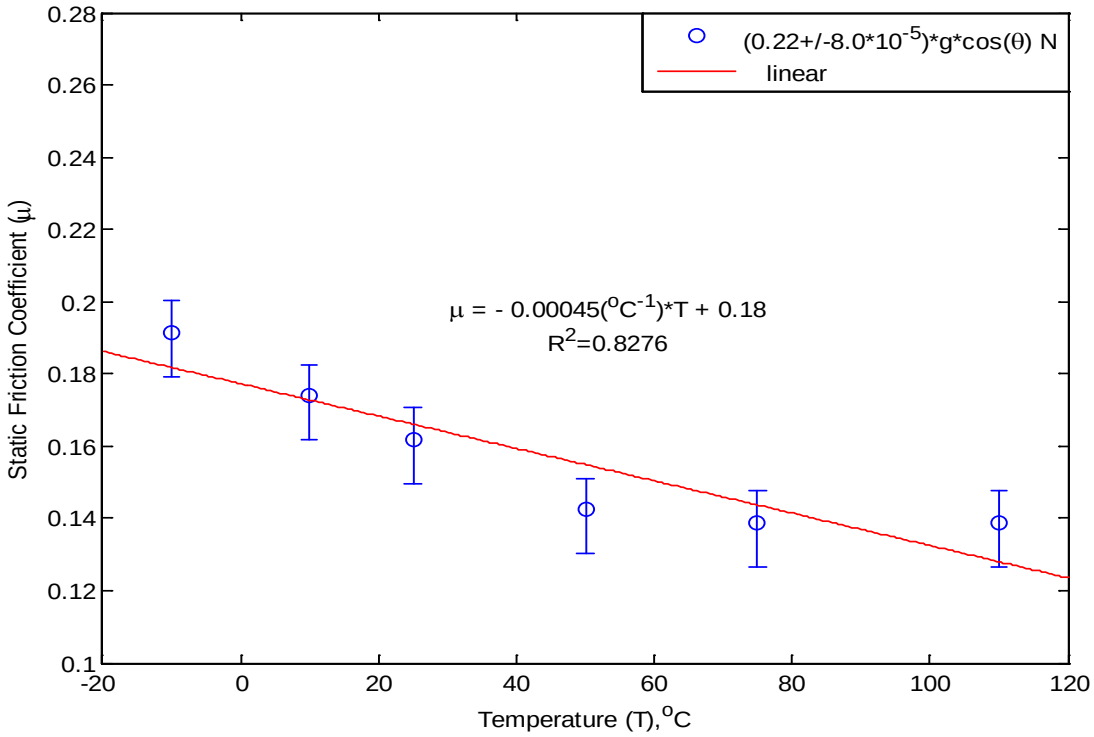

Figure 2-16 Static Friction Coefficient vs. Temperature with 220 grams Compressing the Samples

The results from this experiment will be entered into the ABAQUS™ code that will be discussed in more detail in Chapter 3. Tables 2-2 to 2-7 show what will be entered into ABAQUS™. Static Friction Coefficient will be entered into ABAQUS™ as it changes with contact pressure instead of force, because it will be entered in the interaction portion of ABAQUS™ (between the spring and blade, and between the blade and receptacle).

Table 2-2 Static Friction Coefficient at -10°C Listed at Various Pressures

Contact Pressure (N/m^2)	Static Friction Coefficient
1235.35	0.235
1755.99	0.256
2283.47	0.255
2811.25	0.254
3358.50	0.227
3916.82	0.191

Table 2-3 Static Friction Coefficient at 10°C Listed at Various Pressures

Contact Pressure (N/m^2)	Static Friction Coefficient
1238.96	0.222
1774.37	0.209
2316.52	0.187
2860.79	0.167
3391.42	0.177
3928.91	0.174

Table 2-4 Static Friction Coefficient at 25°C Listed at Various Pressures

Contact Pressure (N/m^2)	Static Friction Coefficient
1241.76	0.210
1780.17	0.192
2315.25	0.190
2849.86	0.189
3389.30	0.181
3936.59	0.162

Table 2-5 Static Friction Coefficient at 50°C Listed at Various Pressures

Contact Pressure (N/m^2)	Static Friction Coefficient
1252.31	0.163
1791.02	0.156
2333.16	0.142
2868.68	0.149
3417.43	0.125
3948.11	0.142

Table 2-6 Static Friction Coefficient at 75°C Listed at Various Pressures

Contact Pressure (N/m^2)	Static Friction Coefficient
1253.82	0.155
1787.99	0.167
2330.19	0.151
2870.39	0.145
3402.93	0.156
3950.04	0.139

Table 2-7 Static Friction Coefficient at 110°C Listed at Various Pressures

Contact Pressure (N/m^2)	Static Friction Coefficient
1257.23	0.136
1800.17	0.118
2328.53	0.155
2868.68	0.149
3421.26	0.116
3950.04	0.139

2.3) How Static Friction Coefficient is Affected by Pressure

2.3.1) Experimental Procedure and Parameters

Table 2-8 outlines some of the parameters used in the experiment:

Table 2-8 Summary of Experiment Parameters

Minimum Mass	50 g
Maximum Mass	250 g
Mass Increment	10 g
Nominal Contact Area	$2.89*10^{-4}$ m^2
Material Used	Sn

The experiment procedure used is described in the following sequence:

1) Start up apparatus
2) Start with 50 g
3) Let motor increase the inclination angle of the inclined plane until slippage occurs
4) Repeat to verify the measurement
5) Record
6) Increase mass by 10 g
7) Repeat steps 3-6 till the experiment is done

2.3.2) Experimental Results

Figure 2-17 shows that as the normal load increases, the static friction coefficient decreases. Comparing Equation 13 to the results obtained from the experimental method (outside of the temperature chamber), it can be seen (Figure 2-17) that the experimental method follows the analytical trend (which will be explained in section 2.3.3). As the plasticity index increases, the static friction coefficient decreases. Also as the dimensionless pressure (P^*) (Equation 15) increases the static friction coefficient decreases.

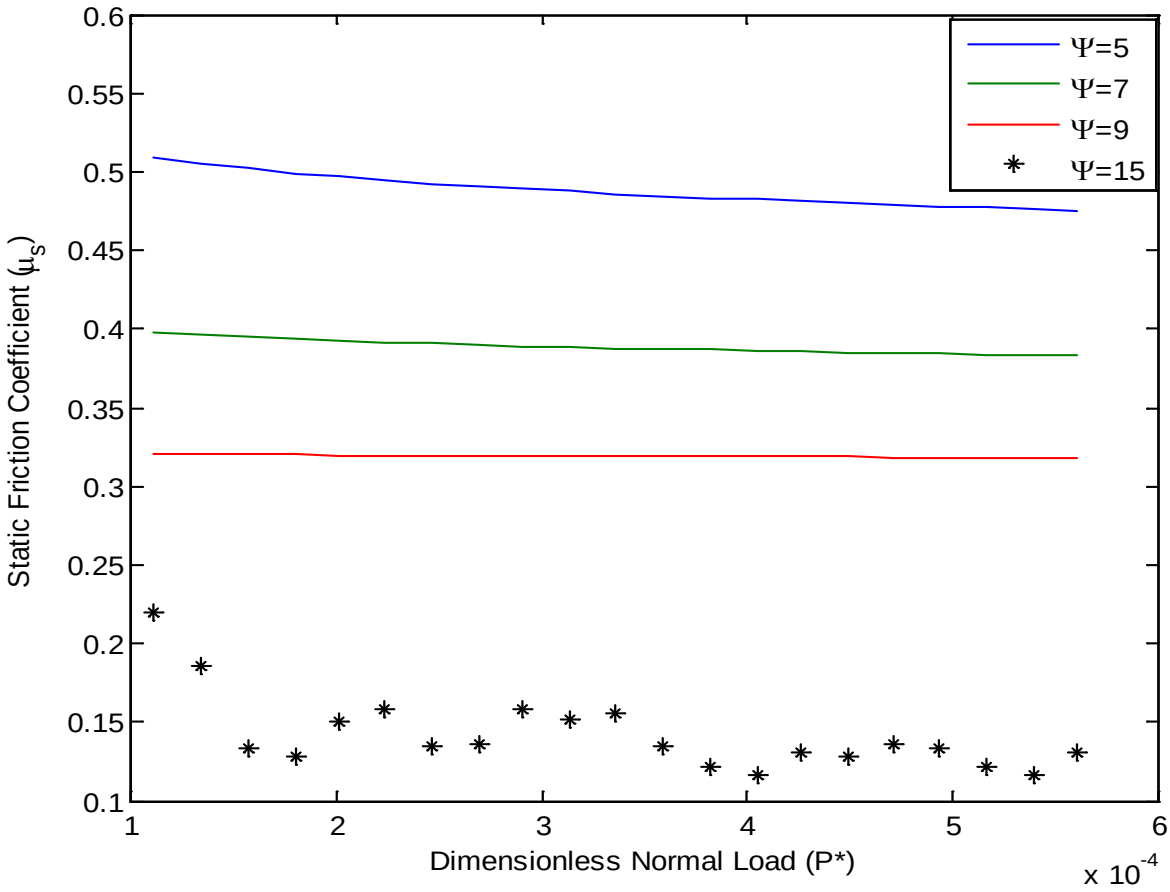

Figure 2-17 Comparison Between Analytical and Experimental Methods[4]

[4] It should be noted that equation 13 is not being used to compare the experimental data due to the fact that it was derived to fit the data of lower plasticity indexes.

2.3.3) Explanation of Results and Analytical Method

The experiment discussed in Section 2.1was performed to test the effect of pressure on the static friction coefficient with the purpose to compare the results obtained by experimental setup shown in Figure 2-8 to that of the analytical model that Cohen, Kligerman, and Etsion derived in Equation 13 (Cohen et al., 2008).

$$\mu = \left(0.26 + \frac{0.43}{\Psi}\right)(P^*)^{0.0095\Psi - 0.09} \quad [13]$$

$$\Psi = \frac{2E'}{\pi C Y (1 - \upsilon^2)}\sqrt{\frac{\sigma_s}{R}} \quad [14]$$

$$P^* = \frac{P}{A_n Y} \quad [15]$$

Where Ψ is the plasticity index, P^* is the dimensionless normal load, and μ is the static friction coefficient, E' is the Hertz Modulus of Elasticity (Equation 16), Y is the Yield Strength, C is a constant dependent on Poisson's Ratio (υ) (Equation 17), σ_s is the standard deviation of asperity heights, A_n is the nominal area, P is the load, R is the asperity radius. Once the experimental and analytical results are found to be compatible, that apparatus will be used in the next experiment.

$$\frac{1}{E'} = \frac{(1 - \upsilon_1^2)}{E_1} + \frac{(1 - \upsilon_2^2)}{E_2} \quad [16]$$

$$C = 1.234 + 1.256\upsilon \quad [17]$$

According to Kogut and Etsion their "…model shows strong effect of the external force and nominal contact area on the staic friction coefficient in contrast to the classical laws of friction. It also that the main dimensionless parameters affecting the static friction coefficient are the plasiticity index and [the] adhesion parameter," (Kogut and Etsion, 2004). This work was done

assuming the following assumptions (It is noteworthly to point out that they are almost the same assumpsions that where used in the Greenwood and Williamson Microcontact Model (Greenwood and Williamson, 1966)):

- The probability density ($\phi(z)$) function is Gaussian:

$$\phi(z) = \frac{1}{\sqrt{2\pi}\sigma_s} \exp\left[-0.5\left(\frac{z}{\sigma_s}\right)^2\right] \quad [18]$$

- The summits of the asperities are spherically capped and the asperity radius of curvature is the same throughout as diplayed in Figure 2-18:
- While loading, the contact load (P), the adhesion force (F), and the static force Q_{max} of each individual asperity depend only on its own interference, if there is no interaction taking place between the asperities, where the interference (ω) is defined[5] as (where z is the height of an asperity measured from the mean of asperity height, and d is the distance between the mean of asperity heights and the smooth rigid surface) :

$$\omega = z - d \quad [19]$$

It is noteworthly to point out that the above assumptions are almost all the same assumpsions that McCool (McCool, 1987) used. The final assumption that the "asperities deform elastically in accordance with the hertzian relation between deflection, load and contact area", is not valid here because aperities could deform plastically as well.

[5] The dimensionless form ($\omega^* = z^* - d^*$)of equation 19 will be used in equations 20-23

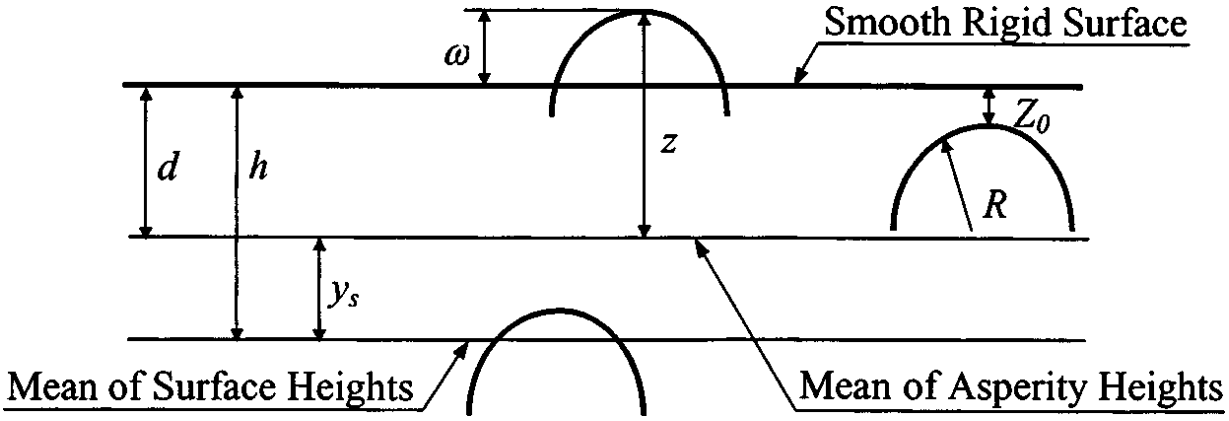

Figure 2-18 Displays that the Asperities are Spherically Capped (Kogut and Etsion, 2004)

Using two of the same governing equations in the Greenwood and Williamson model (Greenwood and Williamson, 1966)(with expection that dimensionless terms are used instead of terms with dimensions) , load (P) and maximum friction force (Q_{max}) can be expressed as:

$$P = \eta A_n \int_d^\infty \bar{P}(z^* - d^*)\phi^*(z^*)\, dz^* \quad [20]$$

$$Q_{max} = \eta A_n \int_d^\infty \bar{Q}_{max}\,(z^* - d^*)\phi^*(z^*)\, dz^* \quad [21]$$

The other governing equations used in this model are contact area due to the normal load alone (A_0), and contact area at sliding inception (A_s).

$$A_0 = \eta A_n \int_d^\infty \bar{A}_0(z^* - d^*)\phi^*(z^*)\, dz^* \quad [22]$$

$$A_s = \eta A_n \int_d^\infty \bar{A}_s(z^* - d^*)\phi^*(z^*)\, dz^* \quad [23]$$

According to Cohen et al. 2008: "In the absence of adhesion, the static friction coefficient is the

ratio of the maximum tangential load at sliding inception over the normal load".

$$\mu = \frac{Q_{max}}{P} = \frac{Q^*_{max}}{P^*} \quad [24]$$

As can be seen in Figure 2-19 (Etsion et al., 2004), the adhesion parameter (θ) is negliable if the plasiticity index (Ψ) is greater than two. This takes place because the plasticity index is proportional to the Hertz Elastic Modulus which is proportional to the yield strength. Concluding that "as the plasticity index increases the static friction becomes much less sensitive to these parameters, similar to the teaching of the classical laws of friction." The plasticity index used in Figure 2-19 can be seen in Equation 25.

$$\Psi = \frac{2E'}{\pi K H}\sqrt{\frac{\sigma_s}{R}} \quad [25]$$

Where H is the hardness of the softer material and the K is the hardness factor:

$$K = 0.454 + 0.41v \quad [26]$$

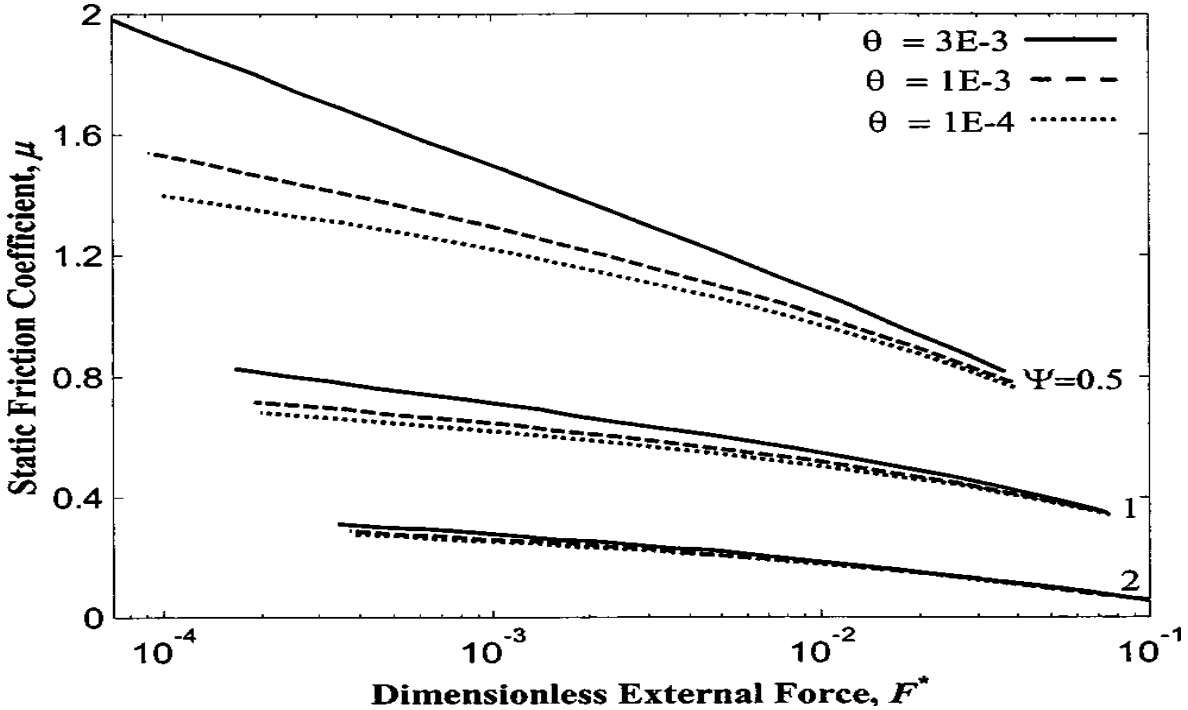

Figure 2-19 Analytical Results Obtained using the Kogut and Etsion Model (Kogut and Etsion, 2004)

2.3.4) Methodology of Analytical Method

To obtain any of the values needed to obtain the plasticity index and adhesion parameter, the raw surface heights need to be gathered using a profilometer as shown in Figure 2-20. Raw surface heights were taken of twenty samples of tin plated copper; ten samples would be placed under the weight set and the remaining ten samples would be placed on the inclining plane. After the raw surface heights are collected from the profilometer the program Dektak v.9 was used to perform a first order leveling[6].

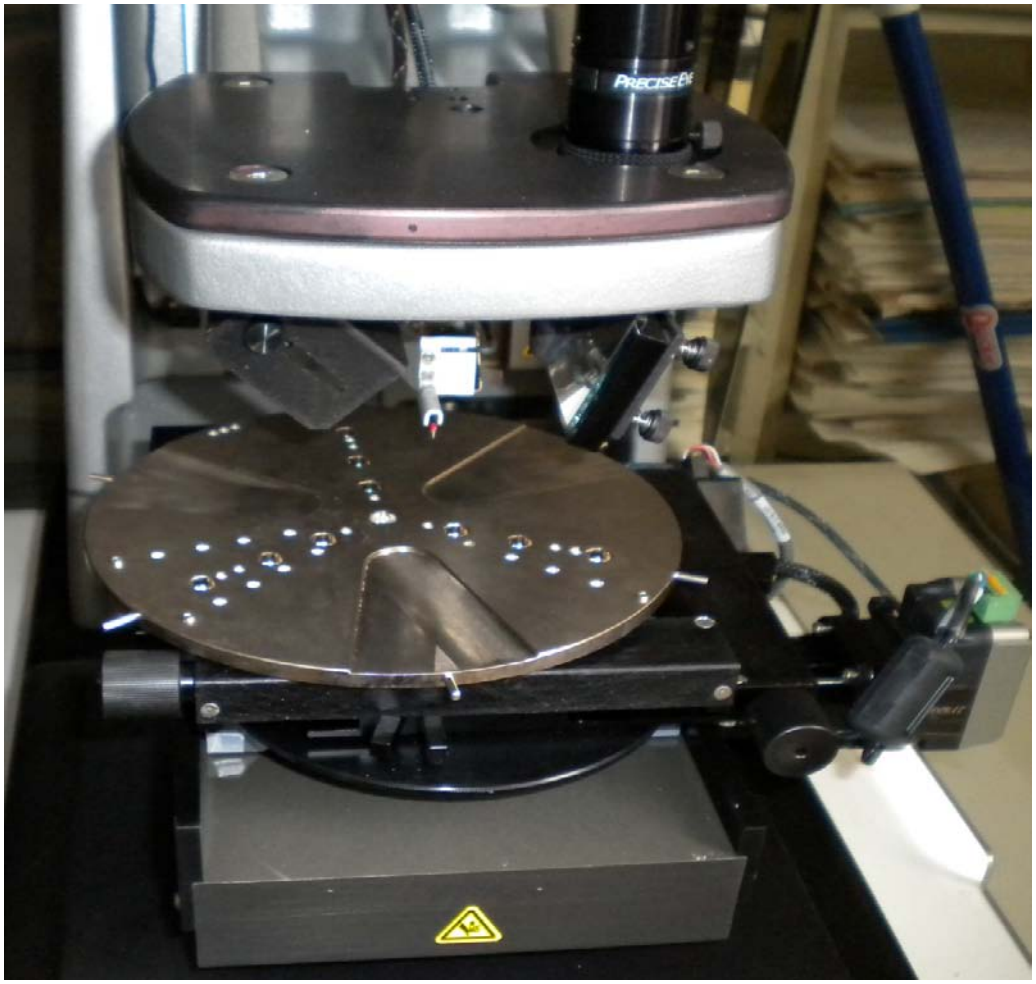

Figure 2-20 Profilometer Used to Obtain Raw Surface Data

[6] Fit a function to the surface heights (in this case a linear function); use that equation to obtain calculated values. Then subtract the calculated values from the measured value. This procedure will then "flatten" the data along the x-axis. In short, to remove any slope of the sample

The next figure is an example of one of the first order leveling of the raw surface heights. It can be seen that the raw surface heights are still not leveled due to the "arc" that can be seen in Figure 2-21. Because of the "arc", an additional second order leveling was performed; using the best fit function, which in this case is a parabolic function[7]. Figure 2-22 shows the second order leveling of the same sample discussed (the other second order leveling will be displayed in Appendix D). Figure 2-23 is the average leveled data of the ten samples that was attached under the weight set, and Figure 2-24 is the average leveled data of the ten samples was attached to the inclined plane.

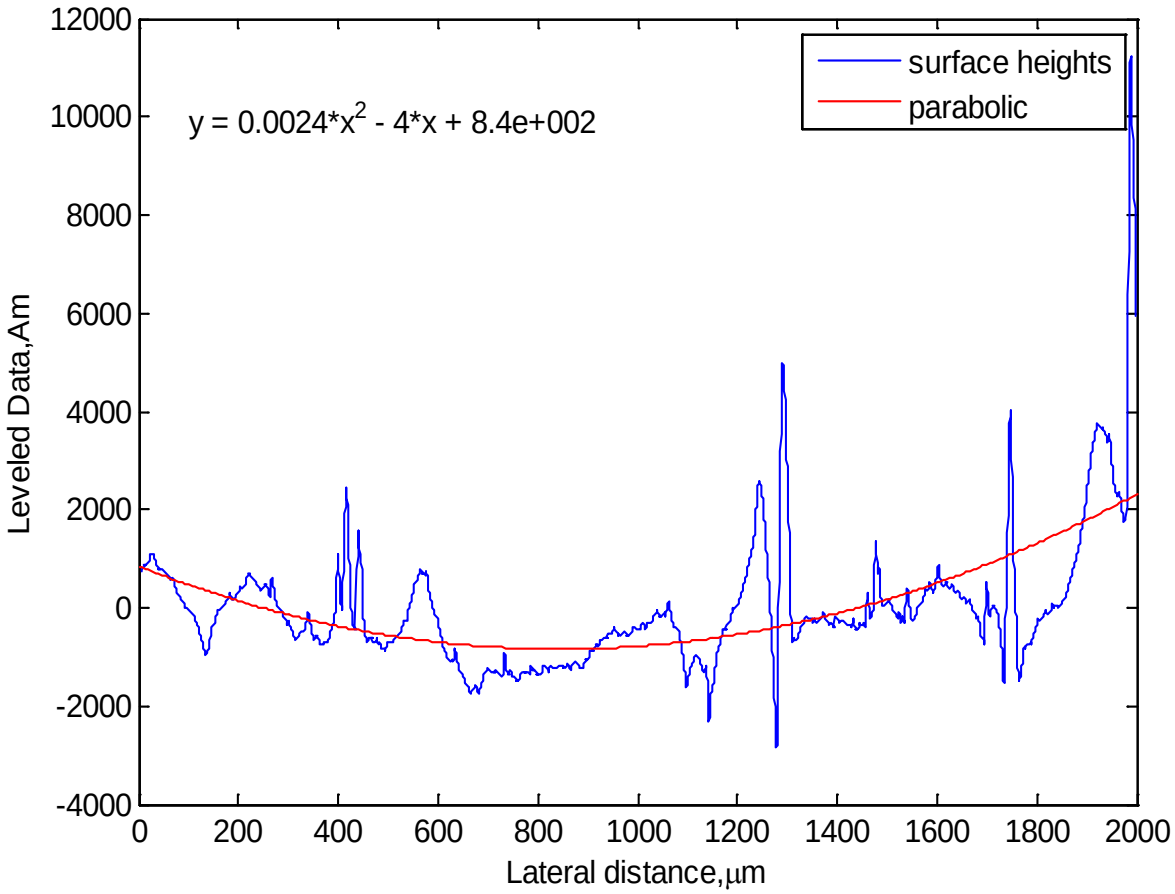

Figure 2-21 First Order Leveling of Raw Surface Heights of Sample

[7] The samples were cut out of a roll. So the samples were bent, despite the fact that they were cut out.

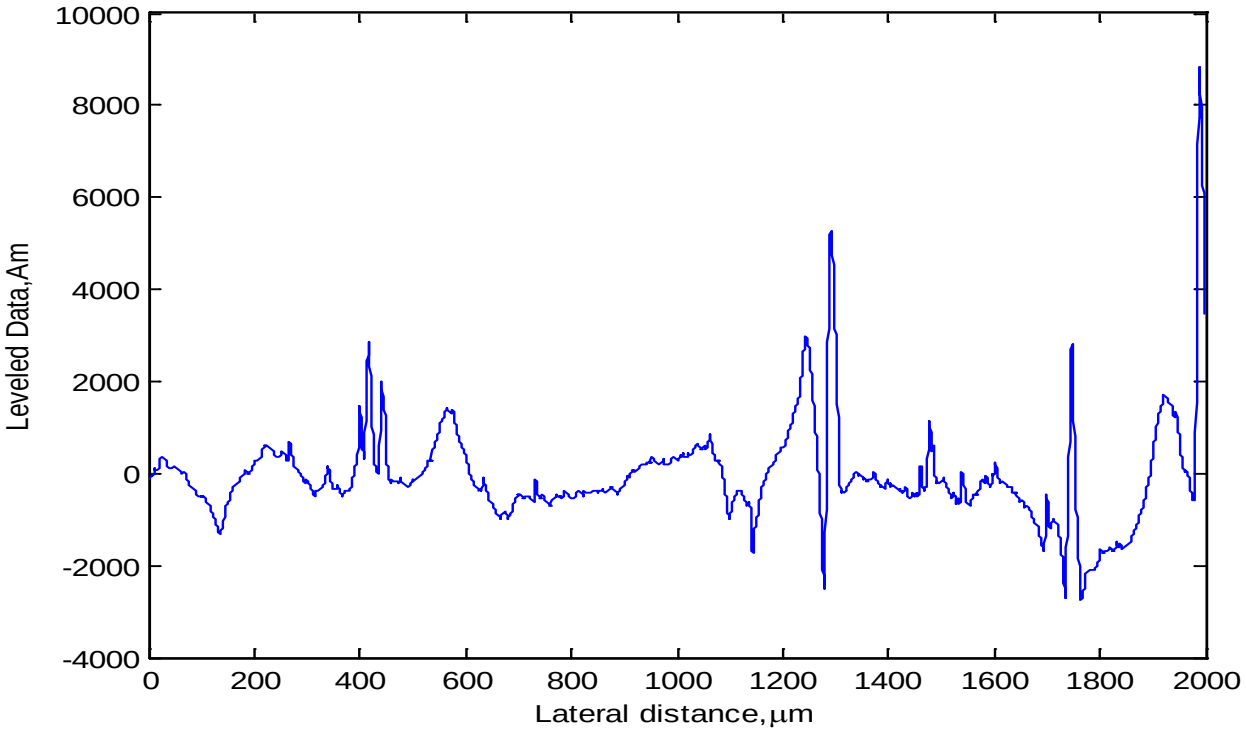

Figure 2-22 Second Order Leveling of Raw Surface Heights of Sample

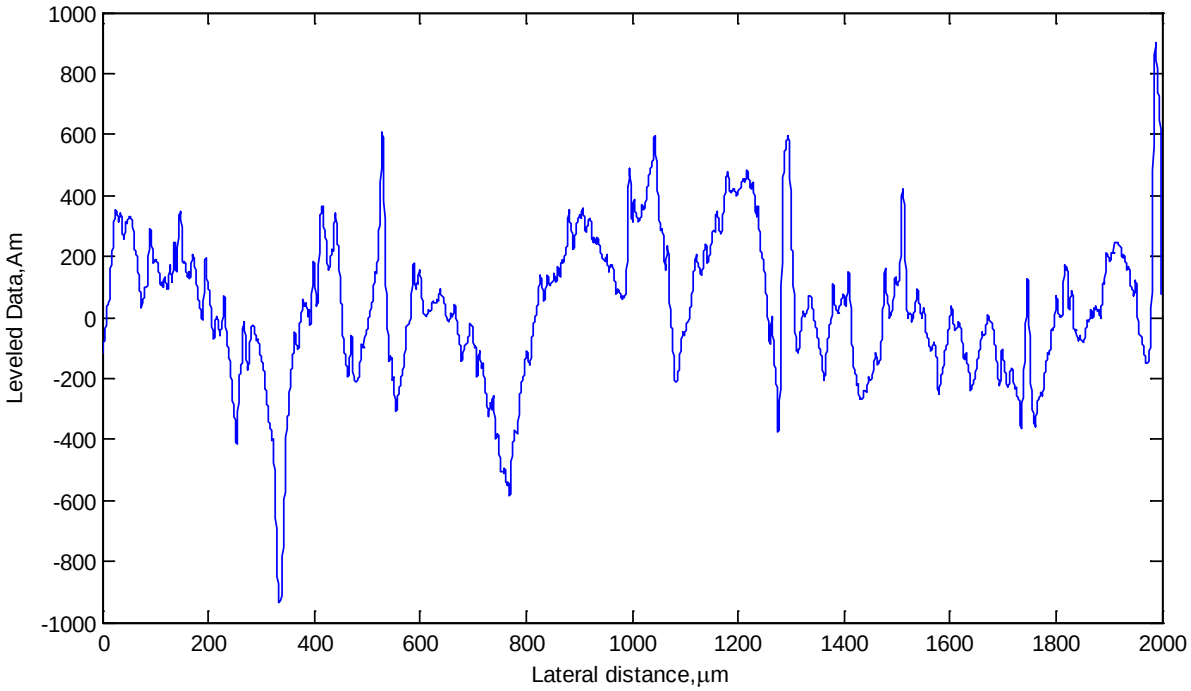

Figure 2-23 Second Order Leveling of Raw Surface Heights of Samples that was Placed Under the Weight Set

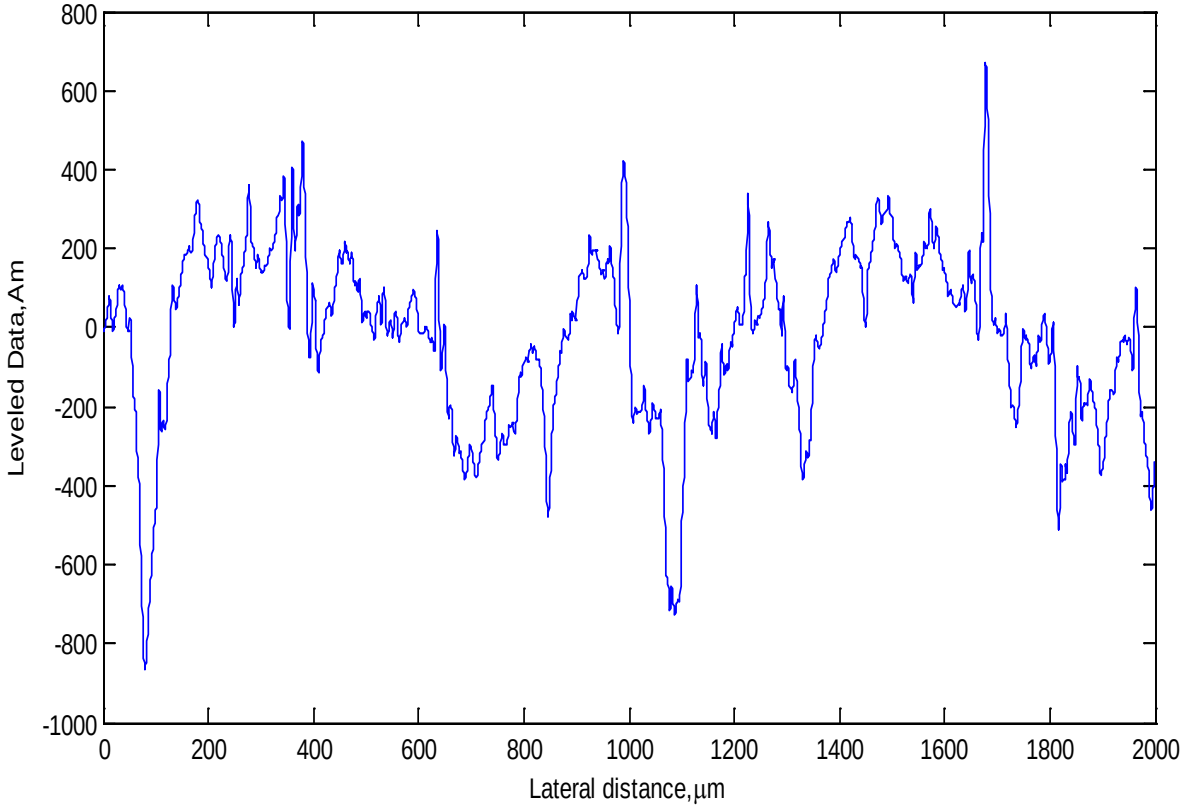

Figure 2-24 Second Order Leveling of Raw Surface Heights of Samples that was Placed on the Inclined Plane

With the leveled data above, the spectral moments outlined by McCool can be found. Spectral moments m_0, m_2, and m_4 are the variance of heights, mean square slope, and the mean square curvature respectively.

$$m_0 = \frac{1}{n}\sum_{i=1}^{\infty} z^2(x) \quad [27]$$

$$m_2 = \frac{1}{n}\sum_{i=1}^{\infty} \left(\frac{dz(x)}{dx}\right)^2 \quad [28]$$

$$m_4 = \frac{1}{n}\sum_{i=1}^{\infty} \left(\frac{d^2z(x)}{dx^2}\right)^2 \quad [29]$$

Spectral moments m_2 and m_4 can be calculated using the forward, central and backward difference methods. From the above spectral moments, the following equations for the asperity radius of curvature, and the asperity height standard deviation can be derived:

$$\boxed{R = 0.375\left(\frac{\pi}{m_4}\right)^{1/2}} \quad [30]$$

$$\boxed{\sigma_s = \left(1 - \frac{0.8968}{\alpha}\right)^{1/2} m_0^{1/2}} \quad [31]$$

Where α is the bandwidth parameter:

$$\alpha = \frac{(m_0 m_4)}{m_2^2} \quad [32]$$

The values obtained from Equations 27-31 and material properties obtained from other sources were used to calculate the plasticity index and the adhesion parameter. Table 2-9 lists the spectral moments, the asperity radius curvature, the summit height standard deviation, the surface standard deviation, the plasticity index, and the adhesion parameter. Appendix E is the Matlab code that is used to calculate the values shown in Table 2-9.

Table 2-9 Numerical Values of Parameters

Parameter	Units	Value
m_0	m^2	1.0721E-15
m_2	n/a	1.1537E-5
m_4	m^{-2}	1.045E7
R	m	2.0561E-4
Y	N/m^2	9E6
σ_s	m	3.2568E-8
C	n/a	1.6485
E'	Pa	2.4857E10
v	n/a	0.33
Ψ	n/a	15

CHAPTER 3- A STUDY OF VIBRATION AND THERMAL INDUCED FRETTING CORROSION

3.1 Similarities between Vibration and Thermal Cycling Models

Recently finite element models have proven to be extremely efficient and reliable. Both 2-D models were constructed in ABAQUS^{TM} and modeled to simulate a single blade/receptacle connector (Figure 3-1 and Figure 3-2). The geometric models for the crimp, receptacle, spring, and supplementary mass are identical in both (vibration and thermal cycling) models. There are differences in the other components of the models and they will be discussed further in this chapter.

Figure 3-1 Blade/receptacle Connector Apart (Chen, 2009b)

Figure 3-2 Blade/receptacle Connector in Contact (Chen, 2009b)

Determining when fretting corrosion induces (in both models) takes place when the horizontal distance (slip) between two specific nodes (points of contact) on the blade and receptacle (see Figure 3-3) reaches a specified amount. "Almost any slip (>1 μm) resulted in an

increased contact resistance in the performed experiments" (Hammam et al., 2005). The specified horizontal distance that was used for both of these models was 1.5μm, because that value was used in "A Study of the Prediction of Vibration-Induced Fretting Corrosion in Electrical Contacts" (Chen, 2009b) and "A Study of Vibration-Induced Fretting Corrosion for Electrical Connectors" (Xie, 2006).

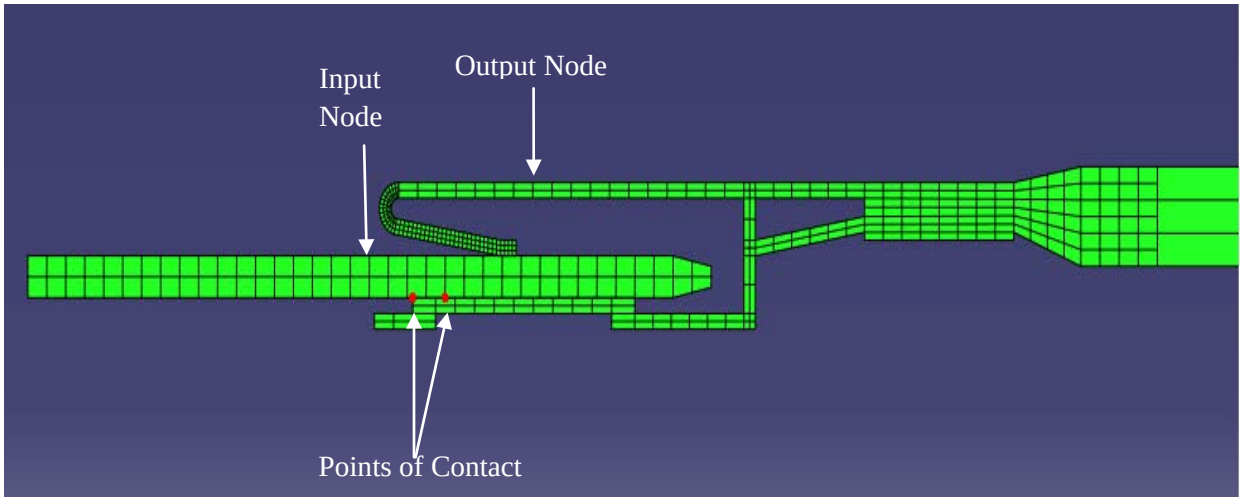

Figure 3-3 Displays the Output and Input Nodes as well as the Points of Contact on the Receptacle and Blade Respectively

The purpose of each finite element model is different. The vibration model, will determine how the onset of fretting corrosion caused by vibration cycling varies under constant temperature. The thermal cycling model, will determine how the onset of fretting corrosion is caused by thermal cycling alone. These two models will be discussed in sections 3.2 and 3.3 respectively.

3.2 Vibration Model

3.2.1 Geometric Model

Figure 3-4 shows the overall view of the model and Figure 3-5 is a closer view of the blade, crimp, receptacle, spring, and supplementary mass. The construction of this model was based on the model that was previously constructed in ANSYS™ that was used in Chen, 2009b and Xie, 2006. Table 3-1 displays the dimensions and density of the components in the model.

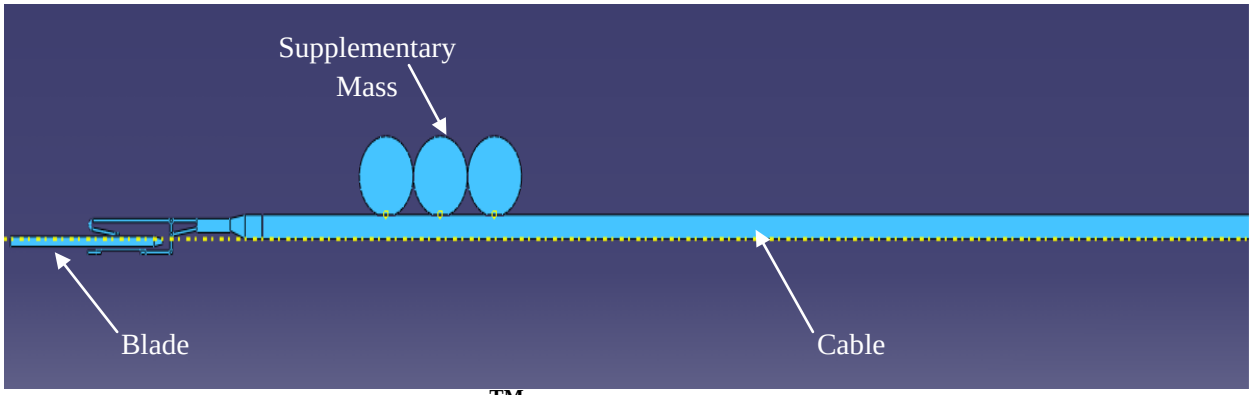

Figure 3-4 2-D ABAQUS™ Model of the Blade/Receptacle Connector

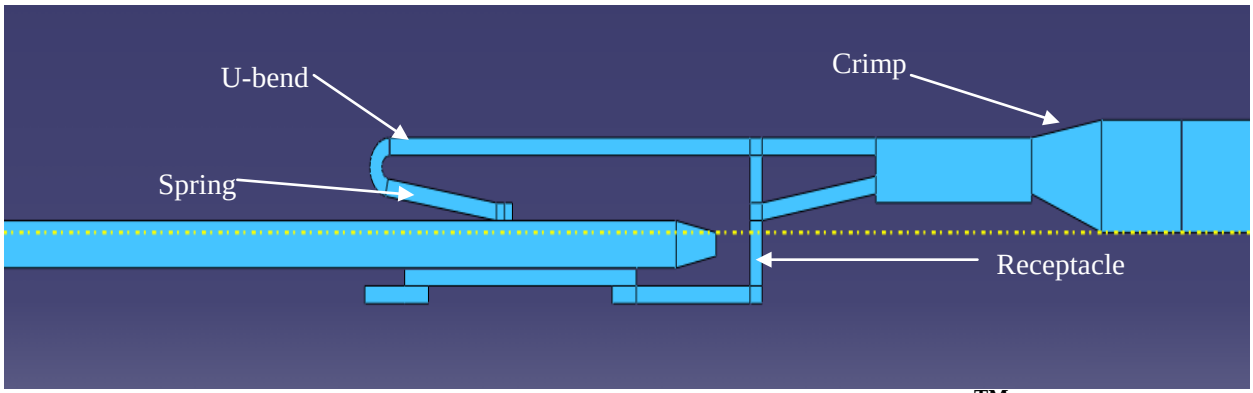

Figure 3-5 Close Up of Spring, and Receptacle of the 2-D ABAQUS™ Model of the Blade/Receptacle Connector

Table 3-1 The Thickness and Density of the Components Used in the Model (Chen et al., 2009b)

Components	Thickness (mm)	Density (kg/m^3)
Blade	1.50	8910
U-bend portion of the cantilever beam	1.90	8910
Cantilever beam spring in the receptacle	1.50	8910
Receptacle (excluding spring member) and part of cable under the crimp	2.55	8910
Cable portion outside the crimp	1.12	4564
Supplementary mass (balls)	2.55	12876

The real thickness of the cable is not 1.12mm. Because the cable's cross section was modeled as a square instead of a circle an equivalent thickness was utilized. Because of the geometric change Equation 33 (Xie, 2006) was used to come up with an equivalent thickness.

$$I_{equivalent} * E_{equivalent} = I_{real} * E_{real} \quad [33]$$

Where E is the Young's Modulus and I is the second moment of area. It should be noted that the Young's modulus for the outer structure of the receptacle (excluding the annulus and spring inside the receptacle) was set to a very large value. The reason for that is because the receptacle was modeled without two sides of the "hollow" box (which is necessary so that the mechanics the spring and blade is visible). Due to the fact that the two sides of a box was removed Young's Modulus of the receptacle needs to be significantly larger. With the larger Young's Modulus, the structure would not deform as the blade was being inserted into the receptacle. The Young's Modulus was set to be 1000 times larger than the original value of the material used to construct the receptacle.

This form of tin plated copper will be entitled: rigid tin plated copper.

To ensure the geometry of the ABAQUS™ and ANSYS™ models are compatible the transfer functions (Figure 3-6) and between frequency and the vertical amplitude (threshold displacement at the shaker head) (Figure 3-7) both were compared and deemed compatible. For this particular model, the transfer function is the ratio of the output node's displacement and the input node's displacement. Because (both experimentally and computationally) the blade is fixed to the shaker, the input displacement is the same as the shaker head. The transfer function can be mathematically expressed as:

$$Transfer\ Function = M\cos\phi + i\,M\sin\phi \quad [34]$$

Where ϕ is the phase angle and M is the magnitude. Based on the transfer function the relative motion (Z_f) can be mathematically expressed as:

$$Z_f = \sqrt{(1 - M\cos\phi)^2 + (M\sin\phi)^2} \quad [35]$$

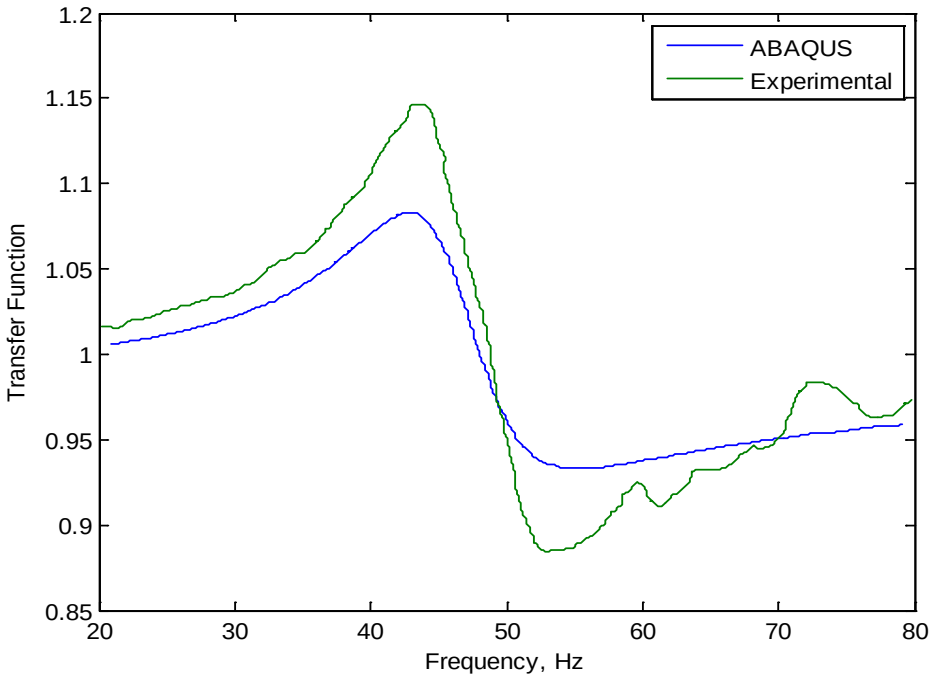

Figure 3-6 Comparison of the Transfer Functions to Show Compatibility

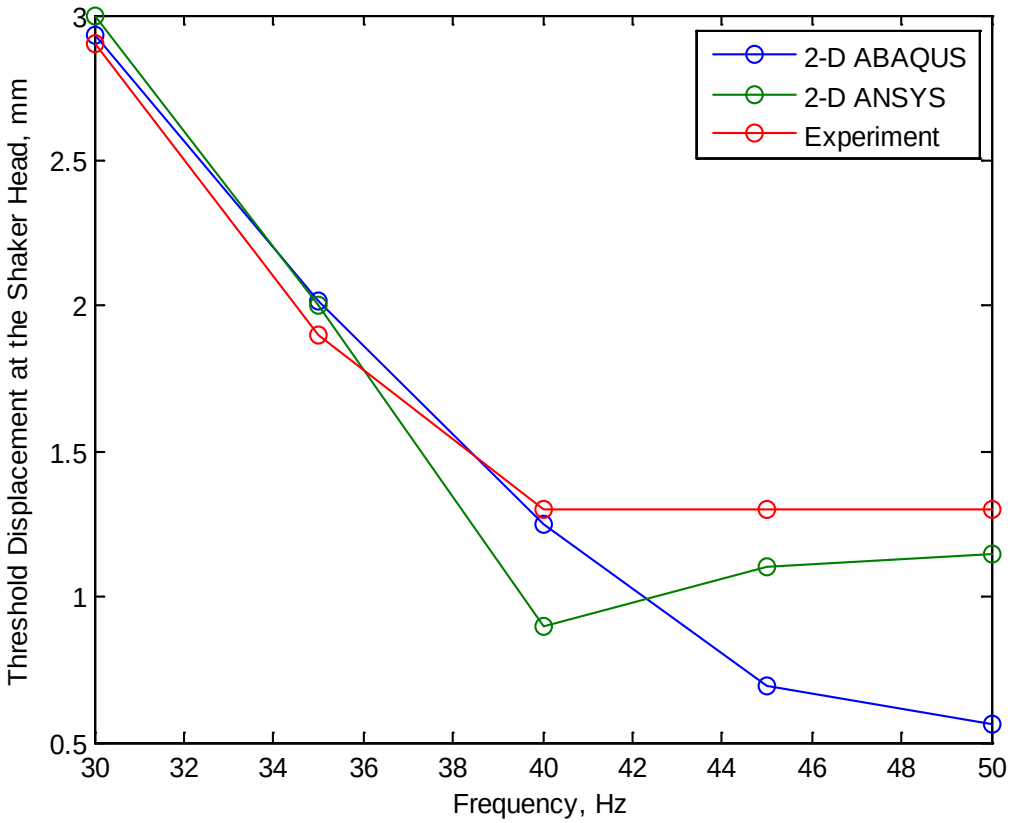

Figure 3-7 Graph to Display that the Current ABAQUS™ Model is Compatible with the Previous ANSYS™ Model and Experiment

3.2.2 Meshing and Element Type

ABAQUS™ does not consider temperature, even though the purpose of the simulation is to determine how temperature affects fretting corrosion during vibration cycling. The element type that is being used is the plane stress element (CPS4R) which according to ABAQUS™ is defined as: "A 4-node bilinear plane stress quadrilateral, reduced integration, hourglass control". Figure 3-8 displays the mesh of the system. It can be seen that the bend of the spring has the finest mesh, while less detailed parts of the model (such as the cable) have a coarser mesh (see Figure 3-9); which is necessary because there is more interest in the mechanism taking place in the connector, not the cable.

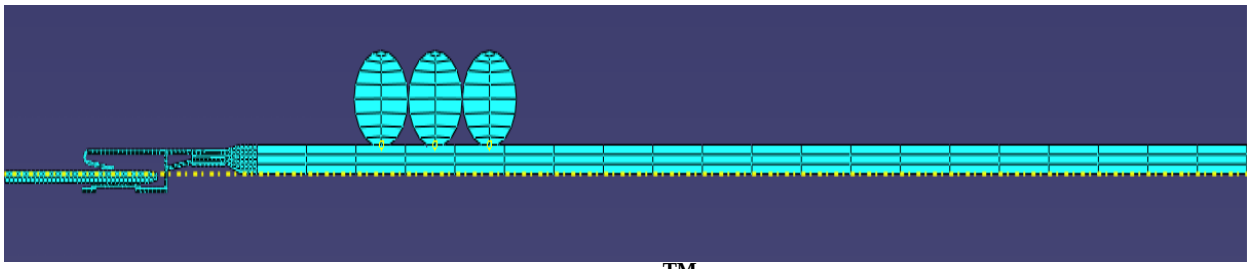

Figure 3-8 Displaying How ABAQUS™ Meshes the Vibration Model

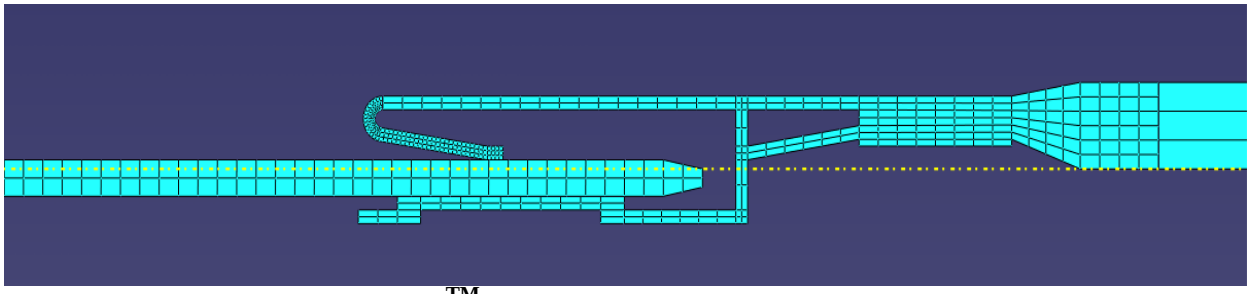

Figure 3-9 How ABAQUS™ Meshes the Blade, Spring, Crimp and Receptacle

3.2.3 Material Properties

In section 3.2.3, one of the initial conditions states that the vibration cycling took place at a specific temperature. Because of this, the Young's Modulus of the cable[8] and the friction coefficient between the blade and the receptacle will be different at each temperature tested. The temperature dependent Young's Modulus for tin plated copper and a rigid tin plated copper, was found in the ASTM Special Technical Publication No. 181 (Upthegrove et al., 1956) and for the Silicone Rubber (which was used to calculate the Young's Modulus of the cable[9]) was found in Tran et al. 2001 (Tables 3-2, 3-3, and 3-4). The static friction coefficient was determined experimentally (section 2.2). The constant temperatures at which vibration cycling will take place are: 50 °C, 75 °C, and 110 °C[10].

[8] With the information given by Upthegrove et al., 1956, the Young's Modulus of tin plated copper and rigid tin plated copper stays the same during those temperatures

[9] Using a form of equation 31, the combined Young's Modulus was determined.

[10] These temperatures were selected based on the availability of the needed material properties.

Table 3-2 List of Materials Used in Model and Corresponding Young's Modulus and the Static Friction Coefficient at 50 °C (Upthegrove et al., 1956, Olin Brass®, and Tran et al. 2001)

Material	Young's Modulus (N/m^2)	Static Friction Coefficient
Tin Plated Copper	129742E6	(See Table 2-5)
Rigid Tin Plated Copper	129742E9	~
Cable	1673.95E6	~

Table 3-3 List of Materials Used in Model and Corresponding Young's Modulus and the Static Friction Coefficient at 75 °C (Upthegrove et al., 1956, Olin Brass®, and Tran et al. 2001)

Material	Young's Modulus (N/m^2)	Static Friction Coefficient
Tin Plated Copper	129742E6	(See Table 2-6)
Rigid Tin Plated Copper	129742E9	~
Cable	1721.50E6	~

Table 3-4 List of Materials Used in Model and Corresponding Young's Modulus and the Static Friction Coefficient at 110 °C (Upthegrove et al., 1956, Olin Brass®, and Tran et al. 2001)

Material	Young's Modulus (N/m^2)	Static Friction Coefficient
Tin Plated Copper	129742E6	(See Table 2-7)
Rigid Tin Plated Copper	129742E9	~
Cable	1543.73E6	~

3.2.4 Boundary Conditions

The boundary conditions listed below was setup to simulate the blade/receptacle connector undergoing vibration cycling while the surrounding temperature is set to a specific temperature. This model undergoes three steps, which are described below.

1. Initial Conditions: Cable end is fixed. Select temperature and change material properties accordingly (see Figure 3-10 below).
2. Step 1 (0.1 sec): Cable and receptacle are fixed; in addition to the initial conditions, a concentrated load (see Figure 3-11) was added. The reason for the concentrated load is to simulate contact normal force, between blade and spring (see Figure 3-11 below).
3. Step 2 (0.5 sec): Cable is still fixed; receptacle is no longer fixed. Vertical displacement amplitudes and frequencies on blade are specified ahead of time (see Figure 3-12 below).

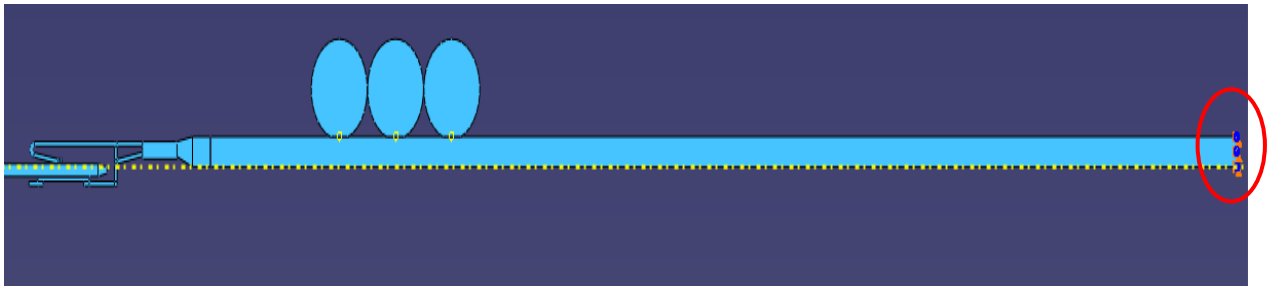

Figure 3-10 Visually Describing the Initial Conditions of the Model

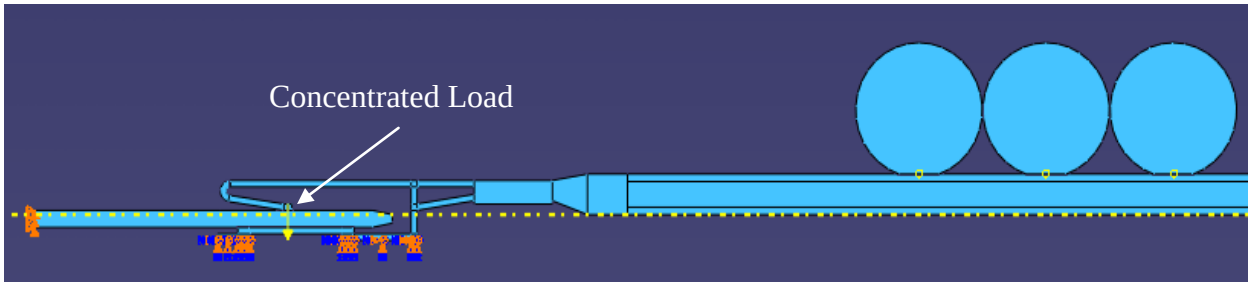

Figure 3-11 Visually Describing the First Step of the Model

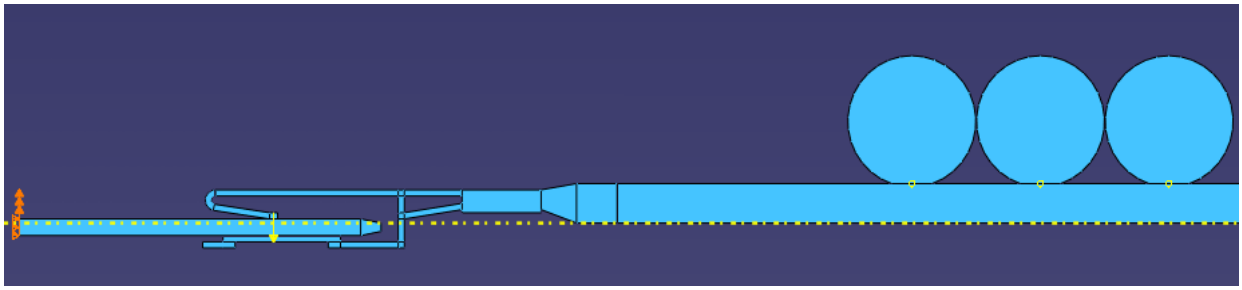

Figure 3-12 Visually Describing the Final Step of the Model

3.2.5 Results and Process

The change in distance between the two points of contact is caused by the vertical displacement taking place at the outer end of the blade: because temperature is constant therefore differential thermal expansion does not play a part. Figure 3-13 shows that in this model, temperature does not play that large of a role. To ensure that it was not a programming error, the Transfer Functions of the model for each temperature are shown in Figure 3-14.

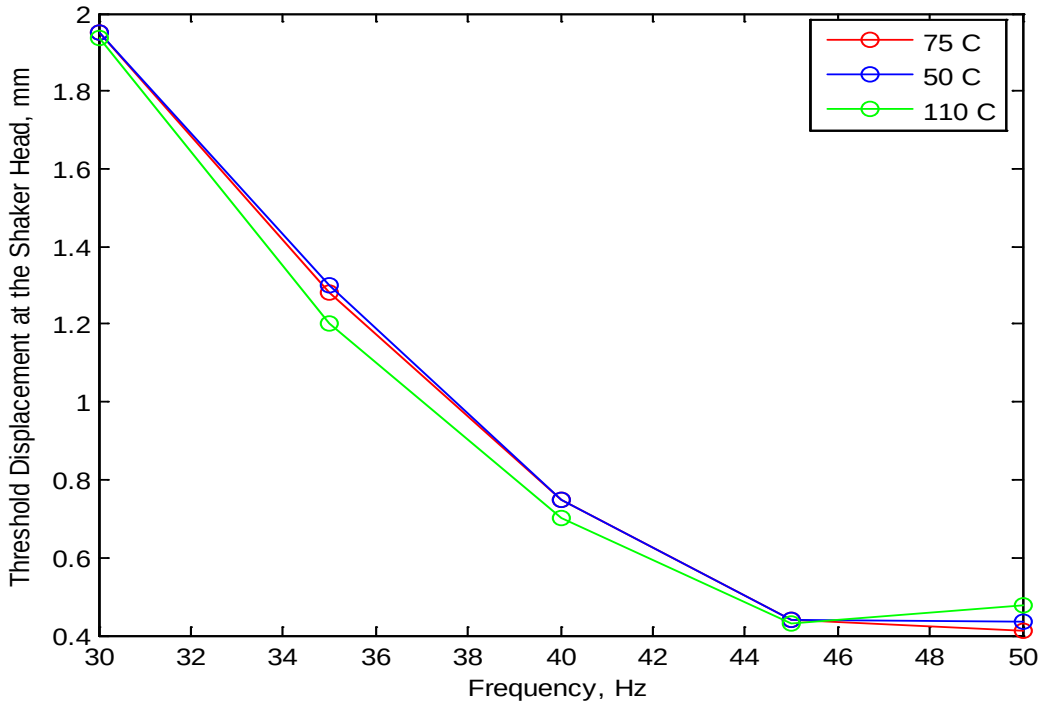

Figure 3-13 Graphically Displaying How Constant Temperature Plays Apart During Vibration Cycling in this Model

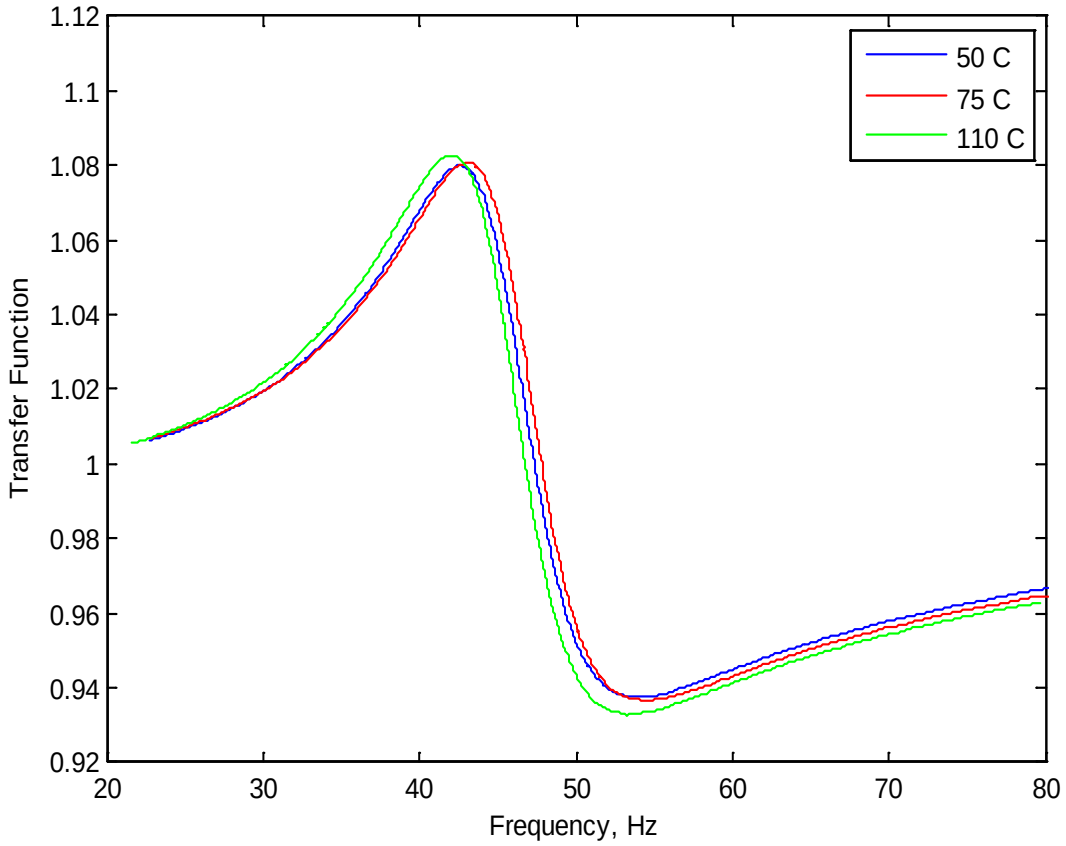

Figure 3-14 Transfer Functions[11] of the Connector Model at 50 °C, 75 °C, and 110 °C

There are two reasons to expect these results. Because of the limited temperature range there was not a large difference in the Young's Modulus for each cable. Also due to the limited temperature range, the Young's Modulus of tin plated copper and rigid tin plated copper did not change at all; causing even less change from temperature to temperature.

[11] Use equations 34 and 35

3.3 Thermal Cycling Model

3.3.1 Geometric Model

The same spring, receptacle, and crimp that were used in the model described in the vibration model (section 3.2) was used in the thermal cycling model (see Figure 3-15 for an overall view). The cable in the thermal cycling model does have a modification, which can be seen in Figure 3-16. The blade also underwent some modifications as well. The reason for these modifications will be discussed further in the following sections (3.3.2.1 and 3.3.2.2).

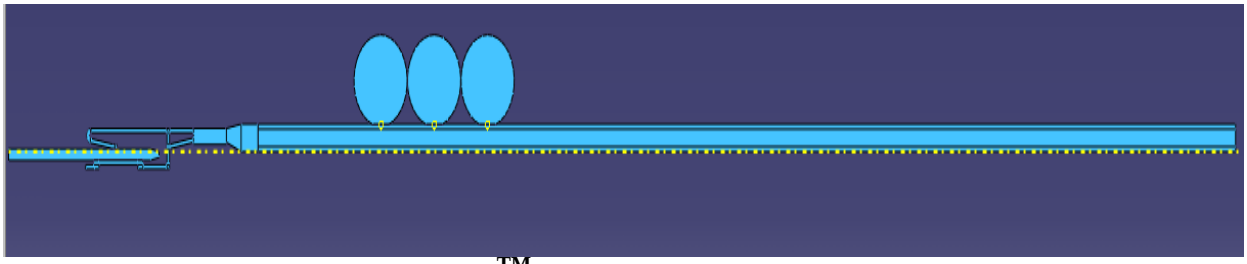

Figure 3-15 2-D ABAQUS™ Model Used to Simulate Thermal Cycling

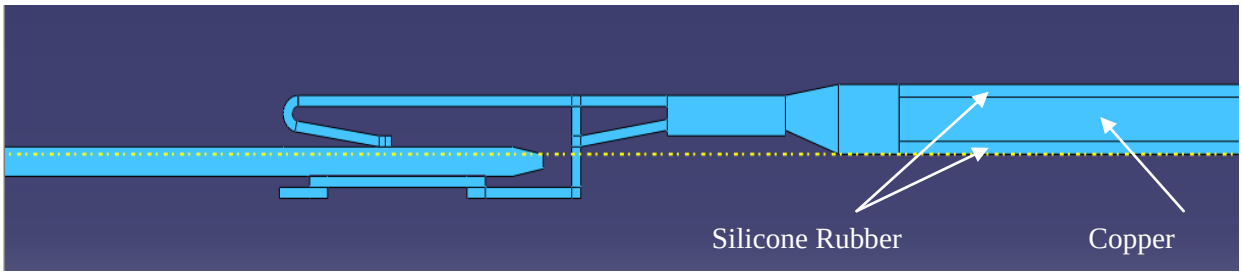

Figure 3-16 Close-Up of Model Used to Simulate Thermal Cycling

3.3.2 Meshing and Element Type

The meshing of the thermal cycling model is very similar to that of the vibration model. Like the vibration model, the bend of the spring has the finest mesh, while less detailed parts of the model (such as the cable) have a coarser mesh (See Figures 3-17 and 3-18). It should be noted that the mesh of the blade is finer in the thermal cycling model than in the vibration model. Because differential thermal expansion is driving the motion of the model due to change of temperature a different element type is being used. The element type that is being used for this model is coupled temperature-displacement (CPE4RT). According the ABAQUS™, the definition of this type of element is: "A 4-node plane strain thermally coupled quadrilateral, bilinear displacement and temperature, reduced integration, hourglass control."

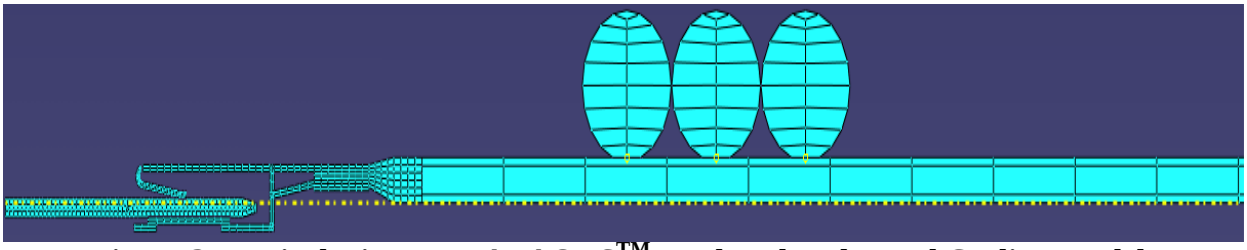

Figure 3-17 Displaying How ABAQUS™ Meshes the Thermal Cycling Model

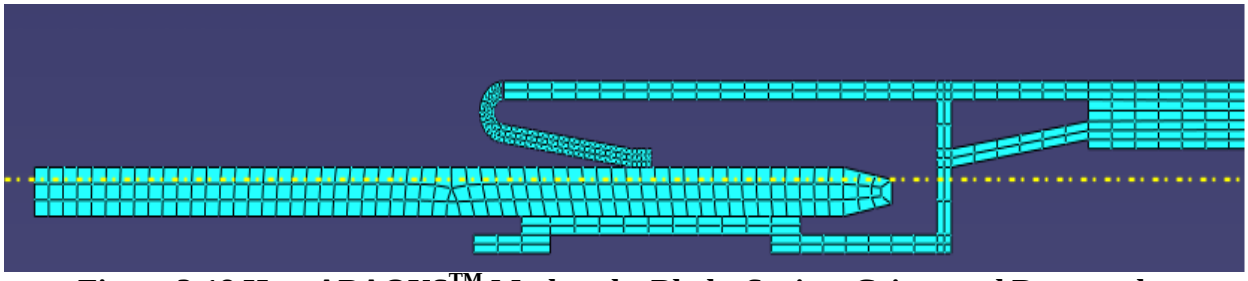

Figure 3-18 How ABAQUS™ Meshes the Blade, Spring, Crimp and Receptacle

3.3.3 Material Properties

As was discussed in Section 3.2.2, material properties do change as a function of temperature. All of these have either been experimentally determined and/or have been published in tables in either handbooks or textbooks. The upcoming sections will be discussing the following temperature dependent properties: heat transfer coefficient, thermal conductivity, thermal expansion, Young's Modulus, and static friction coefficient.

3.3.3.1 Heat Transfer Coefficient

According to thermophysical property tables in the back of any heat transfer textbook various properties of gases that affect the heat transfer coefficient such as kinematic viscosity, conductivity, and Prandtl Number, are tabulated as a function of temperature. Using the values found in the appendix (A.4) of "Fundamentals of Heat and Mass Transfer" by Incropera et al., the following equation (derived by Churchill and Bernstein) could be used for the blade, receptacle, and the cable:

$$\overline{Nu_D} = \frac{\bar{h}D}{k} = 0.3 + \frac{0.62Re_D^{1/2}Pr^{1/3}}{[1+(0.4/Pr)^{2/3}]^{1/4}}\left[1+\left(\frac{Re_D}{282{,}000}\right)^{5/8}\right]^{4/5} \quad [36]$$

It should be noted that the cable is not modeled as a cylinder, but as a rectangular cube (Section 3.2.1). Therefore the equation used to find the heat transfer coefficient would be the same as the one used for the other rectangles in the model. In order to use equation 36 to find $\bar{h}$, some key assumptions were made :

1. The velocity of the air (U_∞) as it passes over the connector is 0.76 m/s, which is the velocity of the air inside a temperature chamber.
2. Convection is only being applied in one direction (see Figure 3-19)

3. The type of convection being used is forced convection. This is the only type of convection that can be used in ABAQUS™ (Analysis User Manuel Volume V).
4. The temperature used to determine the properties, which would determine the heat transfer coefficient, is the surrounding temperature. There are two reasons to use the surrounding temperature instead of the film temperature (average of the surface and the surroundings):
    - Initial temperatures of both the surroundings and the surfaces are the same (room temperature).
    - Convection alone is heating the model (there is no electrical current going through the model).

The validity of assumption number four comes from what happens physically to the model (which is discussed in the two bullets above). The difference between the film temperature, the temperatures of the surroundings and the surface temperature would be negligible. Figure 3-19 displays how each part of the connector was modeled, displaying the characteristic length used to calculate the Reynolds Number. Tables 3-5, 3-6, and 3-7 display the Heat Transfer coefficient values calculated by equation 36 and entered into ABAQUS™. Also in Figure 3-20 shows how the blade was modified to ensure that convection would not be taking place inside of the receptacle.

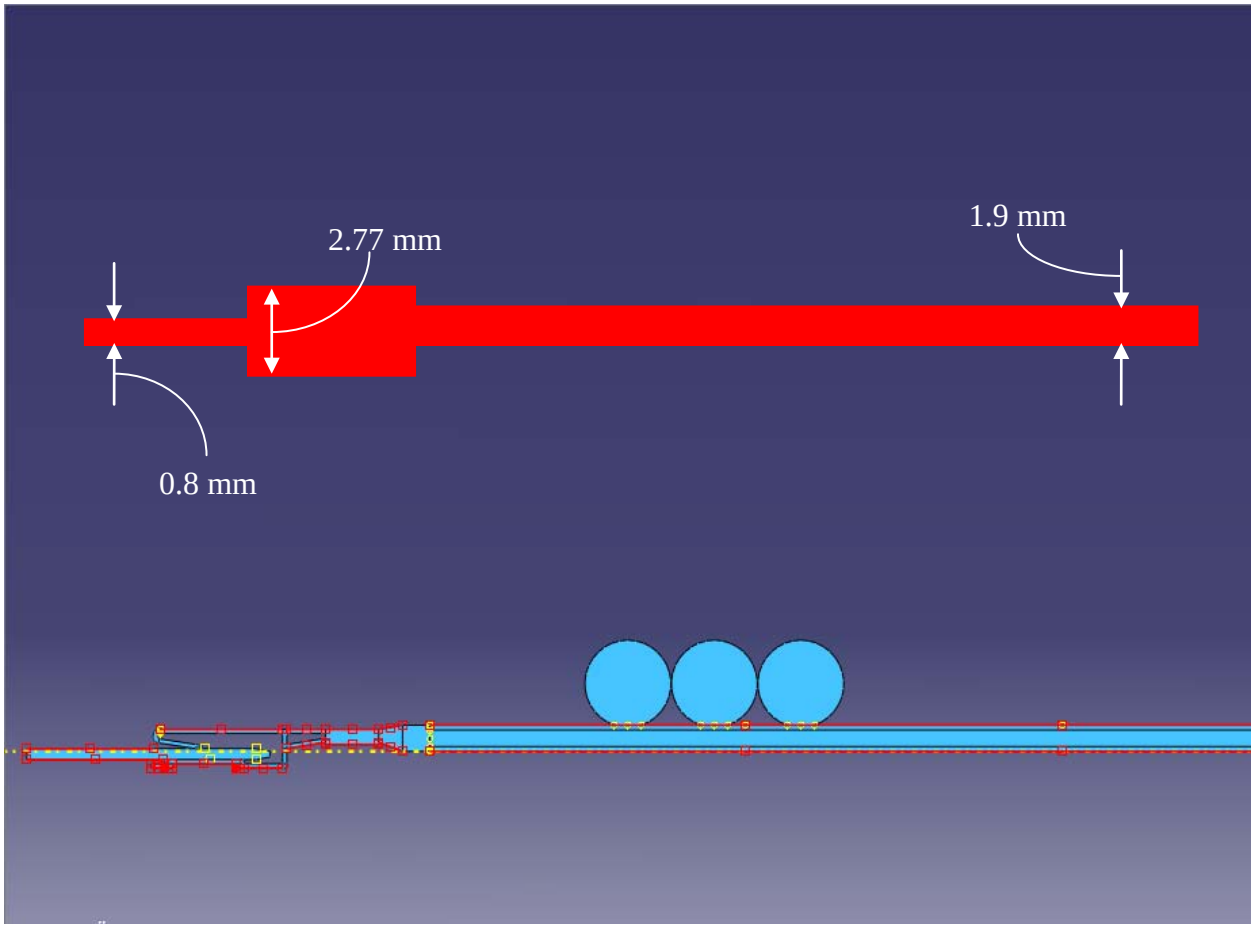

Figure 3-19 Displays the Simpler Model used to Calculate the Heat Transfer Coefficient and where Convective Heat Transfer was Modeled

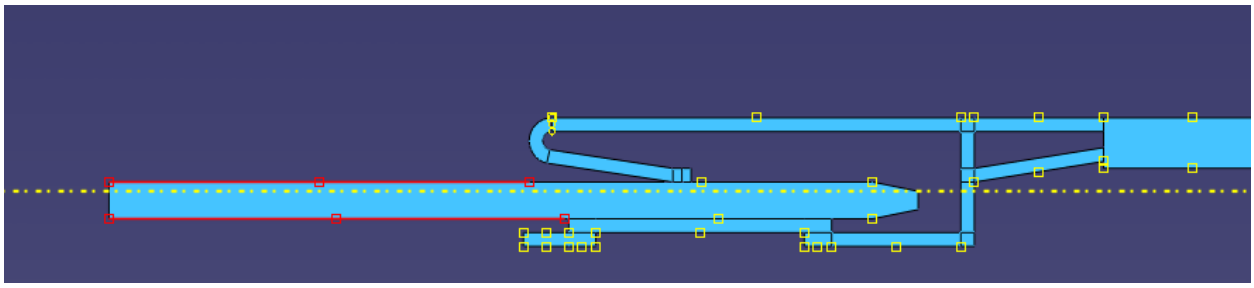

Figure 3-20 Displays Altered Line Segments on the Blade

Table 3-5 Temperature Dependent Heat Transfer Coefficient for the Receptacle

Temperature (°C)	Heat Transfer Coefficient (W/m^2-°C)
-173.15	1.07
-123.15	1.55
-73.15	2.01
26.85	2.90
76.85	3.30
126.85	3.71
226.85	4.46
326.85	5.13
476.85	6.00
826.85	7.79
926.85	8.31
1226.85	10.88
1826.85	15.98
2226.85	24.11
2726.85	52.76

Table 3-6 Temperature Dependent Heat Transfer Coefficient for the Blade

Temperature (°C)	Heat Transfer Coefficient (W/m^2-°C)
-173.15	3.61
-123.15	5.28
-73.15	6.89
26.85	9.96
76.85	11.35
126.85	12.77
226.85	15.36
326.85	17.68
476.85	20.68
826.85	26.90
926.85	28.70
1226.85	37.60
1826.85	55.22
2226.85	83.38
2726.85	182.47

Table 3-7 Temperature Dependent Heat Transfer Coefficient for the Cable

Temperature (°C)	Heat Transfer Coefficient (W/m^2-°C)
-173.15	1.54
-123.15	2.24
-73.15	2.92
26.85	4.22
76.85	4.80
126.85	5.40
226.85	6.49
326.85	7.47
476.85	9.11
826.85	11.35
926.85	12.11
1226.85	15.85
1826.85	23.28
2226.85	35.14
2726.85	76.88

3.3.3.2 Thermal Conductivity and Thermal Expansion

In order to obtain an accurate response from the cable during thermal cycling, two sections had to be added to the cable (see Figure 3-16). As can be seen from Tables F-3 and F-4, the difference between the thermal expansions of both copper and silicone rubber is extremely large. Also combining the two of them together would be inaccurate, because area for the copper and silicone rubber are not equal to each other. Because of that reason, picking either one of the material's thermal expansions is not an option. In order to obtain an accurate temperature distribution using separate thermal conductivities was necessary. It can be seen on Table F-1 and F-2 that the thermal conductivities of both materials are very different:

3.3.3.3 Young's Modulus

In Section 3.3.1, it is stated that the Young's Modulus of the outer structure (rigid tin plated copper) of the receptacle is set to a very large value (numerical values used in the program can be seen in Table F-8). To determine how Young's Modulus varies with temperature, the values determined for tin plated copper was scaled[12] for rigid tin plated copper. The Young's Modulus for the components of the cable (silicone rubber and copper) are also listed in Tables F-9 and F-10.

3.3.3.4 Static Friction Coefficient

The static friction coefficient for tin on tin was experimentally found using methods discussed in Chapter 2. Tables 2-6, 2-7, and 2-8 display the numerical values that were graphically displayed in Chapter 2 (see Figures 2-11 to 2-16). Because the pressure between the spring and the blade was extremely high (due to a small contact area), the static friction

[12] 1000x greater

coefficient was determined at several pressures. ABAQUS™ will be able to determine a function, thus determining the static friction coefficient at the specified temperature and pressure.

3.3.4 Boundary Conditions

The boundary conditions listed were setup to simulate the blade/receptacle connector undergoing thermal cycling. This model undergoes three steps which are described in the steps below.

1. Initial Conditions: Receptacle, blade, and cable are all fixed. Room temperature (20 °C) is the initial temperature (see Figure 3-21).
2. Step 1 (0.1 sec): Same as initial conditions; in addition to the initial conditions a concentrated load was added. The concentrated load simulates contact normal force, between blade and spring (see Figure 3-22).
3. Step 2: Blade and cable are still fixed, receptacle is no longer fixed. Temperature amplitudes and frequencies are specified (See Figure 3-19).

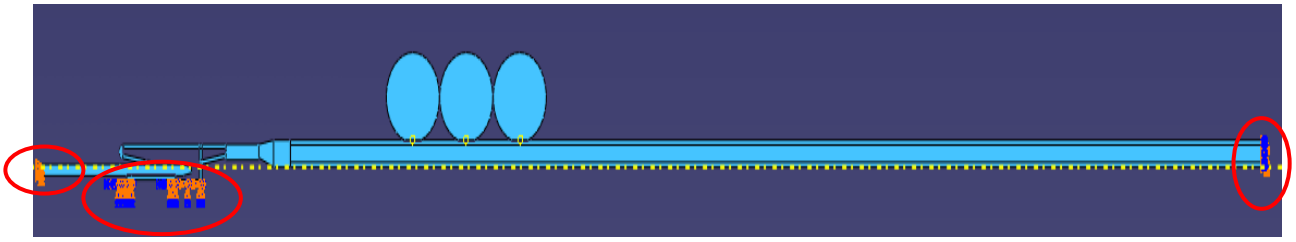

Figure 3-21 Visually Describing the Initial Conditions of the Model

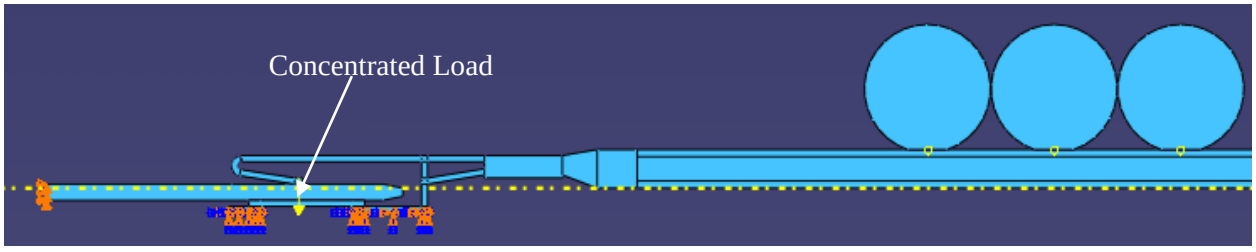

Figure 3-22 Visually Describing the First Step of the Model

3.3.5 Results and Process

Differential thermal expansion drives the motion between the points of contact. The faster the temperature cycle the larger the temperature difference needed for the difference between the output and input to be 1.5μm. This is due to a time lag between the surrounding temperature and the connector and cable, which is illustrated in Figures 3-23 and 3-24. For the connector temperature to change one degree (by convective heat transfer), it takes 538 sec; for the cable to change one degree, it takes 533 sec. As the temperature change increases the time needed for the rest of the system to arrive to that temperature also increases. The frequencies that where simulated in ABAQUS™ are: $\frac{1}{300}$ Hz, $\frac{1}{600}$ Hz, $\frac{1}{900}$ Hz, $\frac{1}{1800}$ Hz, $\frac{1}{3600}$ Hz, and $\frac{1}{10800}$ Hz (which equates to one cycle per 5 min, 10 min, 15 min, 30 min, 1hr, and 3 hr respectively).

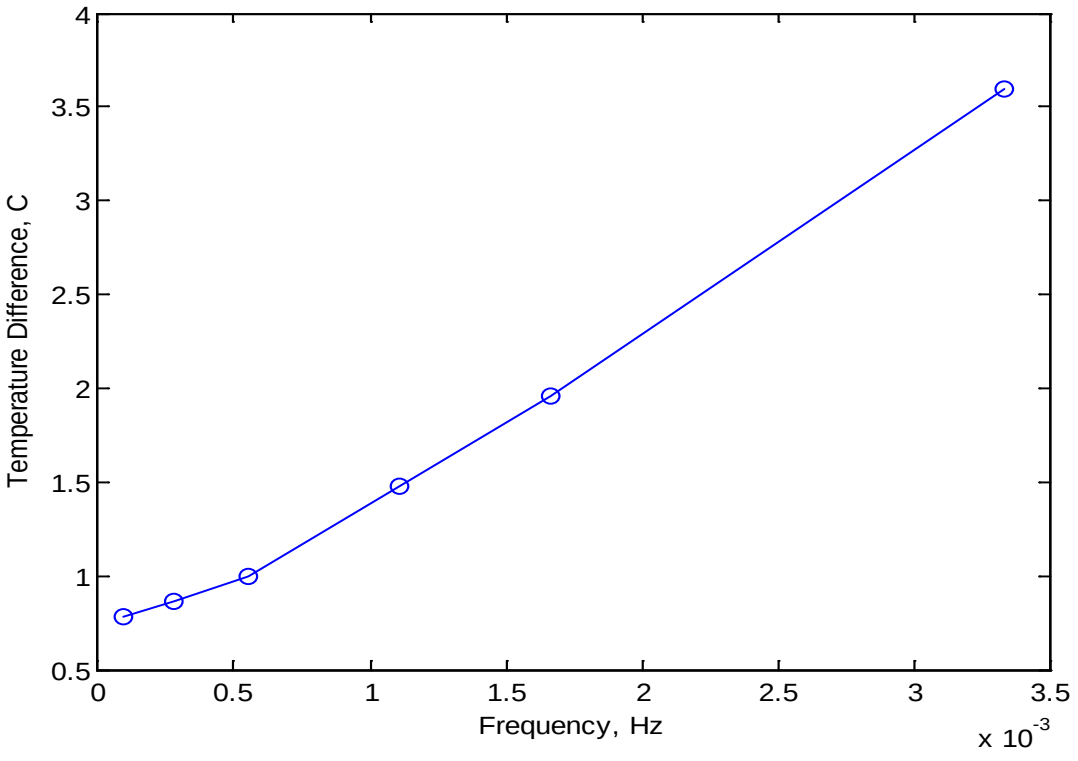

Figure 3-23 Temperature Difference (During Thermal Cycling) Needed to Produce Fretting Corrosion

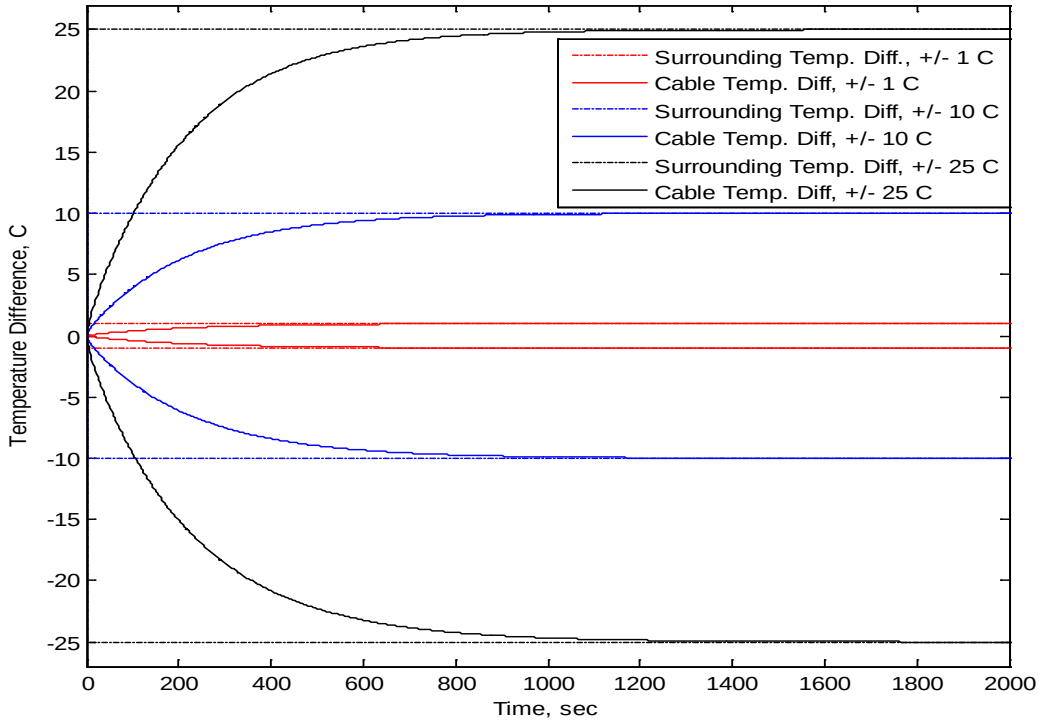

Figure 3-24 Time Lag Between Cable Temperature and Surrounding Temperature at Various Temperature Differences

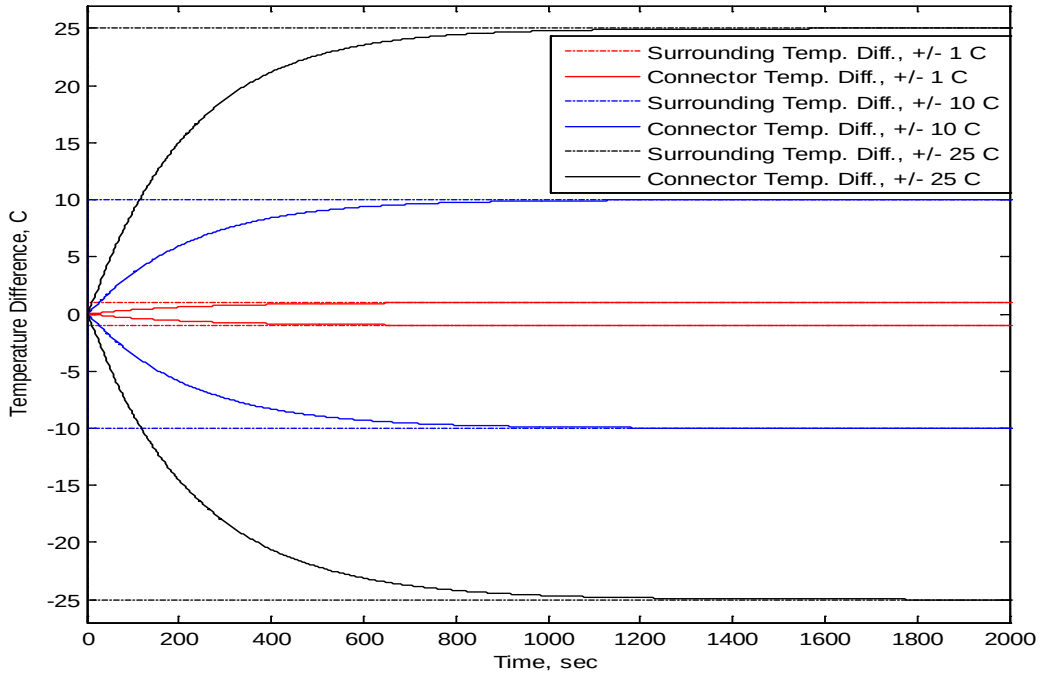

Figure 3-25 Time Lag Between Connector Temperature and Surrounding Temperature at Various Temperature Differences

CHAPTER 4- CONCLUSION AND FUTURE WORK

Two experiments and two computational models have been presented in this thesis. Both experiments examined how pressure and temperature affect the static friction coefficient. It was found that as the pressure increased the static friction coefficient decreased. This held true to the previously published data (Cohen et al. 2008). Because trend of the analytical and the experimental data coincided, data produced from that apparatus could be trusted. That same apparatus was then used in a temperature chamber to see how temperature affected the static friction coefficient. It was found that as temperature increased the static friction coefficient decreased. This was expected, so the results obtained from that experiment were then entered into the finite element models.

With the data from the experiments conducted in the previous paragraph and other experiments done in the past, both finite element models were constructed and produced results. In the vibration model, because the material properties varied very little it was hardly any change, but it can be seen that the same overall trend (as the frequency increases, the threshold displacement at the shaker head, decreases) obtained from that program matches the trend from Chen, 2009b. The second model showed how thermal cycling affects fretting corrosion. The results obtained from that model show that as the frequency of the temperature increases the higher the temperature amplitude (difference) needed for fretting corrosion to start. The reason for this is due to the time lag between the surrounding temperature and the temperature of the connector and the cable.

Progress has been made in the field of fretting corrosion, but more can be done. The following are some suggestions for future research in this area:

- Create a finite element model that not only includes vibration and thermal cycling, but also include electrical current. Electrical current would be a practical and interesting parameter.
- Create a 3-D model to simulate how thermal cycling affects fretting corrosion.
- Design an experiment that can either confirm or reject the 2-D and 3-D finite element models.
- Expand the temperature range in which the temperature dependent materials are tested. Many of the properties are tested at room temperature and above; material properties that were tested at temperatures below room temperature are few and far between.
- Retesting the temperature dependent material properties that would be entered in a finite element model. The vast majority of the temperature dependent properties, for materials used in connectors, were tested in 1950-1970's. Experimental measurements have since greatly improved.

References

[1] S.V. Angadi, W.E. Wilson, R.L. Jackson, G.T. Flowers, and B.I. Rickett, "A multi-physics finite element model of an electrical connector considering rough surface contact," *IEEE Trans. CHMT*, 2008, pp. 168-177.

[2] M. Antler, "Survey of Contact Fretting in Electrical Connectors," *IEEE Trans. CHMT*, vol. 8, 1985, pp. 87-104.

[3] P.J. Arrazola and T. Ozel, "Investigations on the effects of friction modeling in finite element simulation of machining," *International Journal of Mechanical Sciences*, vol. 52, 2010, pp. 31-42.

[4] M. Attia, *Standardization of Fretting Fatigue Test Methods and Equipment*, Philadelphia, PA: ASTM Publication Code, 1992.

[5] E.M. Bock and J.H. Whitley, "Fretting corrosion in electric contacts," *IEEE Holm Conf*, 1974, pp. 128-138.

[6] J.C. Bowling, *2007 Baccalaurate Sermon*, Bourbonnais: 2007.

[7] W. Chang, I. Etsion, and D. Bogy, "Static Friction Coefficient Model for Metallic Rough Surfaces," *ASME Journal of Tribology*, vol. 110, 1988, pp. 57-63.

[8] C. Chen, "A Study of the Prediction of Vibration-Induced Fretting Corrosion in Electrical Contacts," 2009.

[9] D. Cohen, Y. Kligerman, and I. Etsion, "A Model for Contact and Static Friction of Nominally Flat Rough Surfaces Under Full Stick Contact Condition," *ASME Journal of Tribology*, vol. 130, 2008, pp. 1-9.

[10] J. Davis, *Metals Handbook*, Materials Park, OH: ASM International, 1998.

[11] J. Dunkin and D. Kim, "Measurement of Static Friction Coefficient Between Flat Surfaces," *Wear*, vol. 193, 1996, pp. 186-192.

[12] I. Etsion, "A Model for Static Sealing Performance of End Face Seals," *STLE Tribology Transactions*, vol. 37, 1994, pp. 111-119.

[13] I. Etsion and I. Front, "Model for Static Sealing Performance of End Face Seals," *STLE Tribology Transactions*, vol. 37, 1994, pp. 111-119.

[14] G.T. Flowers, F. Xie, M.J. Bozack, X. Hai, B.I. Rickett, and R.D. Malucci, "A Study of the Physical Characteristics of Vibration-Induced Fretting Corrosion," *IEEE Trans. CHMT*, vol. 29, 2006, pp. 318-325.

[15] G.T. Flowers, F. Xie, M.J. Bozack, and R.D. Malucci, "Vibration Thresholds for Fretting Corrosion in Electrical Connectors," *IEEE Trans. CHMT*, vol. 27, 2004, pp. 65-71.

[16] M. Fontana, *Corrosion Engineering*, New York, New York: McGraw Hill, 1986.

[17] H. Gao and G.C. Barber, "Microcontact Model for Paper-Based Wet Friction Materials," *ASME Journal of Tribology*, vol. 124, 2002, pp. 414-419.

[18] J. Geringer, B. Forest, and P. Combrade, "Fretting-corrosion of materials used as orthopaedic implants," *Wear*, vol. 259, 2005, pp. 943-951.

[19] J. Greenwood and J. Williamson, "Contact of Nominally Flat Surfaces," *Royal Society of London. Series A. Mathematical and Physical Sciences*, 1966, pp. 300-319.

[20] Incropera, DeWitt, Bergman, and Lavine, *Fundamentals of Heat and Mass Transfer*, Hoboken, NJ: Wiley and Sons, .

[21] M. Karamis and B. Selcuk, "Analysis of the Friction Behavior of Bolted Joints," *Wear*, vol. 166, 1993, pp. 73-83.

[22] L. Kogut and I. Etsion, "A Static Friction Model for Elastic- Plastic Contacting Rough Surfaces," *ASME Journal of Tribology*, vol. 126, 2004, pp. 34-40.

[23] H. Kongsjorden, J. Kulset, and J. Sletbak, "Degradation of Electrical Contacts Caused by Oscillatory Micromotion Between the Contact Members," *IEEE Trans. CHMT*, vol. 2, 1979, pp. 32-36.

[24] A. Lee and M.S. Mamrick, "Fretting Corrosion of Tin-Plated Copper Alloy," *IEEE Trans. CHMT*, 1987, pp. 63-67.

[25] A. Lee and M.S. Mamrick, "Fretting corrosion of tin at elevated temperatures," *IEEE Trans. CHMT*, 1988, pp. 87-91.

[26] G.H. Majzoobi, J. Nemati, A.J. Rooz, and G.H. Farrahi, "Modification of fretting fatigue behavior of AL7075–T6 alloy by the application of titanium coating using IBED technique and shot peening," *Tribology International*, vol. 42, 2009, pp. 121- 129.

[27] R.D. Malucci, "Accelerated Testing of Tin-Plated Copper Alloy Contacts," *IEEE Trans. CHMT*, vol. 22, 1999, pp. 53-60.

[28] R.D. Malucci, "Impact of fretting parameters on contact degradation," *IEEE Trans. CHMT*, 1996, pp. 395-403.

[29] J.W. McBride, "Developments in fretting studies applied to electrical contacts," *Institute of Electrical and Electronics Engineering*, 2006, pp. 170-180.

[30] J. McCool, "Relating Profile Instrument Measurements to the Functional Performance of Rough Surfaces," *ASME Journal of Tribology*, vol. 109, 1987, pp. 264-270.

[31] A. Monnier, B. Froidurot, C. Jarrige, and R. Meyer, "A Mechanical, Electrical, Thermal Coupled-Field Simulation of a Sphere-Plane Electrical Contact," *IEEE Trans. CHMT*, vol. 30, 2007, pp. 787-795.

[32] A. Moufki, A. Devillez, D. Dudzinski, and A. Molinari, "Thermomechanical modelling of oblique cutting and experimental validation," *International Journal*, vol. 44, 2004, pp. 971-989.

[33] A. Moufki, A. Molinari, and D. Dudzinski, "Modelling of orthogonal cutting with a temperature dependent friction law," *Journal of the Mechanics and Physics of Solids*, vol. 46, 1998, pp. 2103-2138.

[34] A. Nayebi, G. Mauvoisin, and H. Vaghefpour, "Modeling of twist drills wear by a temperature-dependent friction law," *Journal of Materials Processing Technology*, vol. 7, 2007, pp. 98-106.

[35] T. Ozel, "The influence of friction models on finite element simulations of machining ¨," *International Journal of Machine Tools and Manufacture*, vol. 46, 2006, pp. 518-530.

[36] Y.W. Park, T.S. Narayanan, and K.Y. Lee, "Effect of temperature on the fretting corrosion of tin plated copper alloy contacts," *Wear*, vol. 262, 2007, pp. 320-330.

[37] Y.W. Park, T.S. Narayanan, and K.Y. Lee, "Fretting corrosion of tin-plated contacts," *Tribology International*, vol. 41, 2008, pp. 616-628.

[38] C. Richard, "On the Identification and Haptic Display of Friction," 2000.

[39] Y. Sang, M. Dube, and M. Grant, "Dependence of friction on roughness, velocity, and temperature 1," *Physical Review E*, vol. 77, 2008, pp. 1-11.

[40] R. Serway and J. Jewett, *Physics for Scientists and Engineers with Modern Physics*, Belmont, CA: Thomson, Brooks, and Cole, 2004.

[41] D. Tabor, "Friction- The Present State of Our Understanding," *ASME Journal of Tribology*, vol. 103, 1981, pp. 169-179.

[42] D. Thuresson, "Stability of sliding contact—Comparison of a pin and a finite element model," *Wear*, vol. 261, 2006, pp. 896-904.

[43] Y.S. Touloukian, *Thermophysical properties of matter*, New York: IFI/Plenum, 1970.

[44] D. Tran, M. Cooke, and P. Newsome, "Laboratory evaluation of mouthguard material," *Dental Traumatology*, vol. 17, 2001, pp. 260-265.

[45] C. Upthegrove and H. Burghoff, *Elevated-temperature properties of coppers and copperbase alloys. Data compiled by and issued under the auspices of the Data and Publications Panel of the ASTM-ASME Joint Committee on Effect of Temperature on the Properties of Metals*, Philadelphia, PA: ASTM, 1956.

[46] J. Vance, *Rotordynamics of turbomachinery*, New York, New York: Wiley and Sons, 1988.

[47] G. Villeneuve, D. Kulkarni, P. Bastnagel, D. Berry, and W. Lafayette, "Dynamic finite element analysis simulation of the terminal crimping process," *IEEE Holm Conf*, 1996, pp. 156-172.

[48] R. Waterhouse, *Fretting Corrosion*, New York, New York: Pergamon Press, 1972.

[49] J. Williams, *Engineering Tribology*, New York, New York: Cambridge University Press, 2005.

[50] F. Xie, "A study of vibration-induced fretting corrosion for electrical connectors," *Computer*, 2006.

[51] F. Xie, G.T. Flowers, C. Chen, M. Bozack, J. Suhling, B.I. Rickett, R.D. Malucci, and C. Manlapaz, "Analysis and Prediction of Vibration-Induced Fretting Motion in a Blade/Receptacle Connector Pair," *IEEE Trans. CHMT*, vol. 32, 2009, pp. 583-590.

[52] W. Xie, DeMeter, and M. Tretheway, "An Experimental Evaluation of Coefficients of Static Friction of Common Workpiece-Fixture," *International Journal of Machine Tools and Manufacture*, 2000, pp. 467-488.

[53] "OC Oerlikon Corporation AG, Pfäffikon - Oerlikon Solar, Oerlikon Coating, Oerlikon Vacuum, Oerlikon Textile, Oerlikon Drive Systems, Oerlikon Components."

[54] "KSC Corrosion Technology Laboratory Home."

[55] "Bible," *Psalms 3:3*.

[56] "Operating Manual Digital Thermometer," 2009.

[57] "Weights of Classes E1 E2, F1, F2, M1, M1-2, M2, M2-3, Part 1: Metrological and Technical Requirements," 2004, p. 12.

Appendix A- Mechanical Drawings

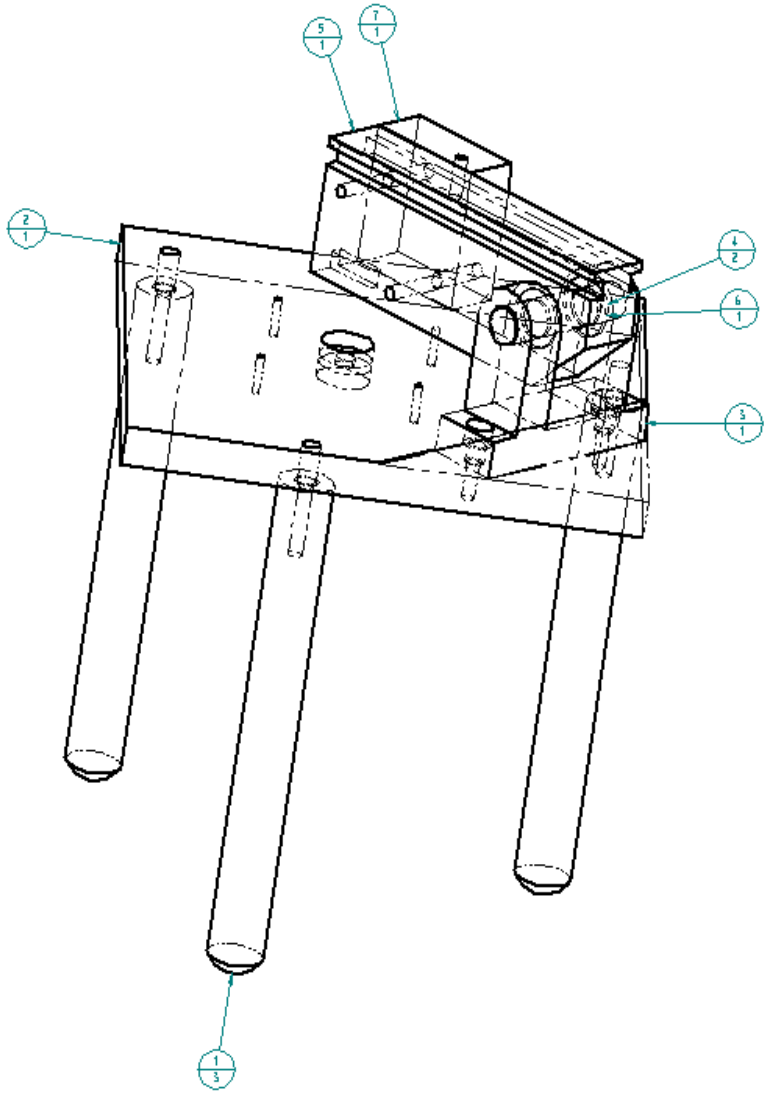

REVISION HISTORY			
REV	DESCRIPTION	DATE	APPROVED

BILL OF MATERIALS			
ITEM NUMBER	PART	QUANTITY	MATERIAL
1	LEGS	3	ALUMINUM
2	PLATE	1	ALUMINUM
3	HOLDER	1	ALUMINUM
4	WASHER	2	ALUMINUM
5	INCLINED PLANE	1	ALUMINUM
6	ROD	1	ALUMINUM
7	SENSOR HOLDER	1	ALUMINUM

	NAME	DATE
DRAWN	rzi0002	11/11/09
CHECKED		
ENG APPR		
MFG APPR		

UNLESS OTHERWISE SPECIFIED
DIMENSIONS ARE IN MILLIMETERS
ANGLES ±X°
2 PL ±XXX 3 PL ±XXXX

SOLID EDGE
UGS - The PLM Company

TITLE: MOTORIZED INCLINE PLANE

SIZE A2 | DWG NO | REV

FILE NAME: whole.dft

SCALE: | WEIGHT: | SHEET 1 OF 1

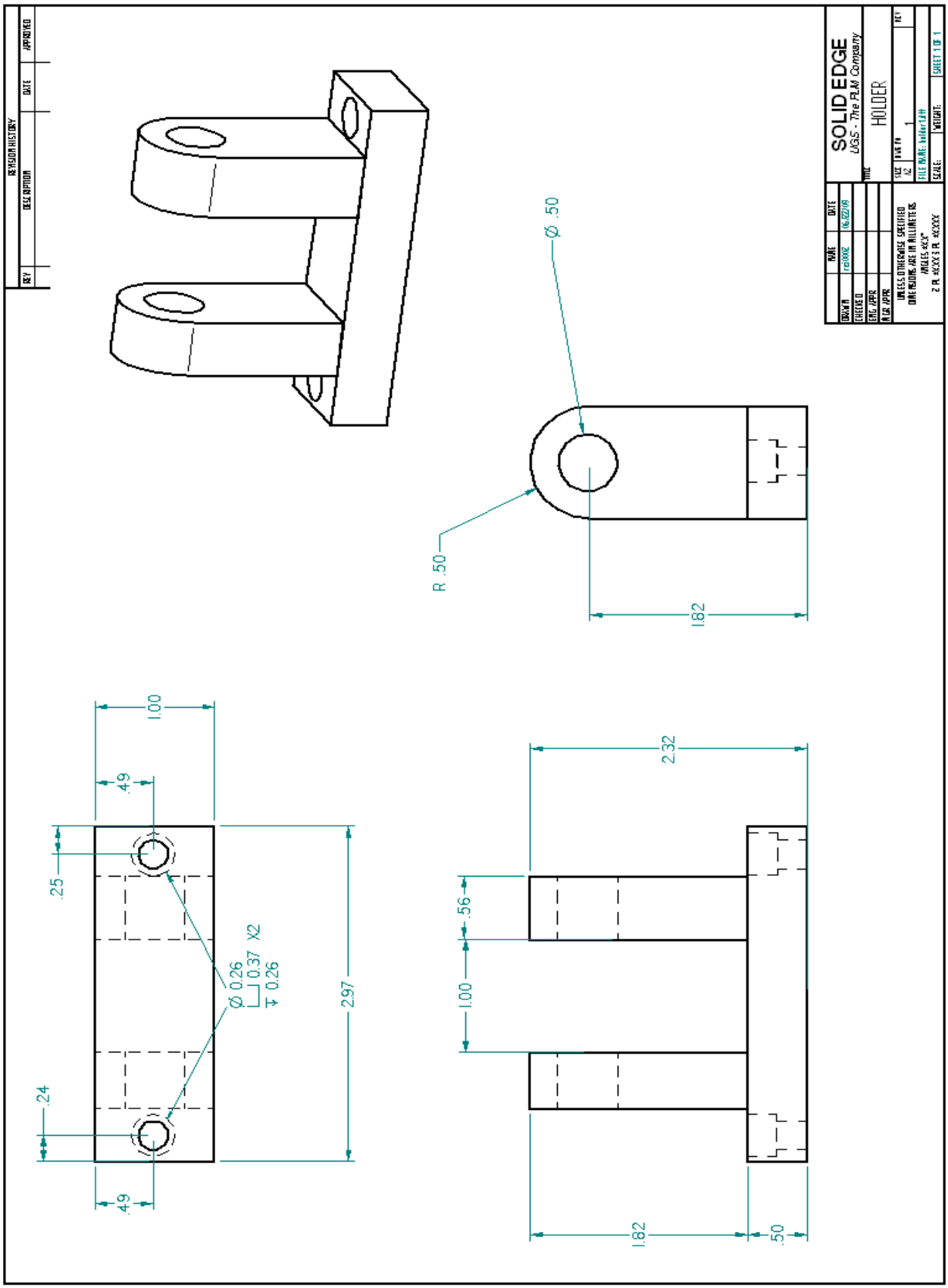
SOLID EDGE
UGS - The PLM Company
HOLDER
Ø .50
R .50
1.82
2.32
.56
1.00
.50
.25
.49
1.00
.24
Ø 0.26
0.37 X2
0.26
2.97

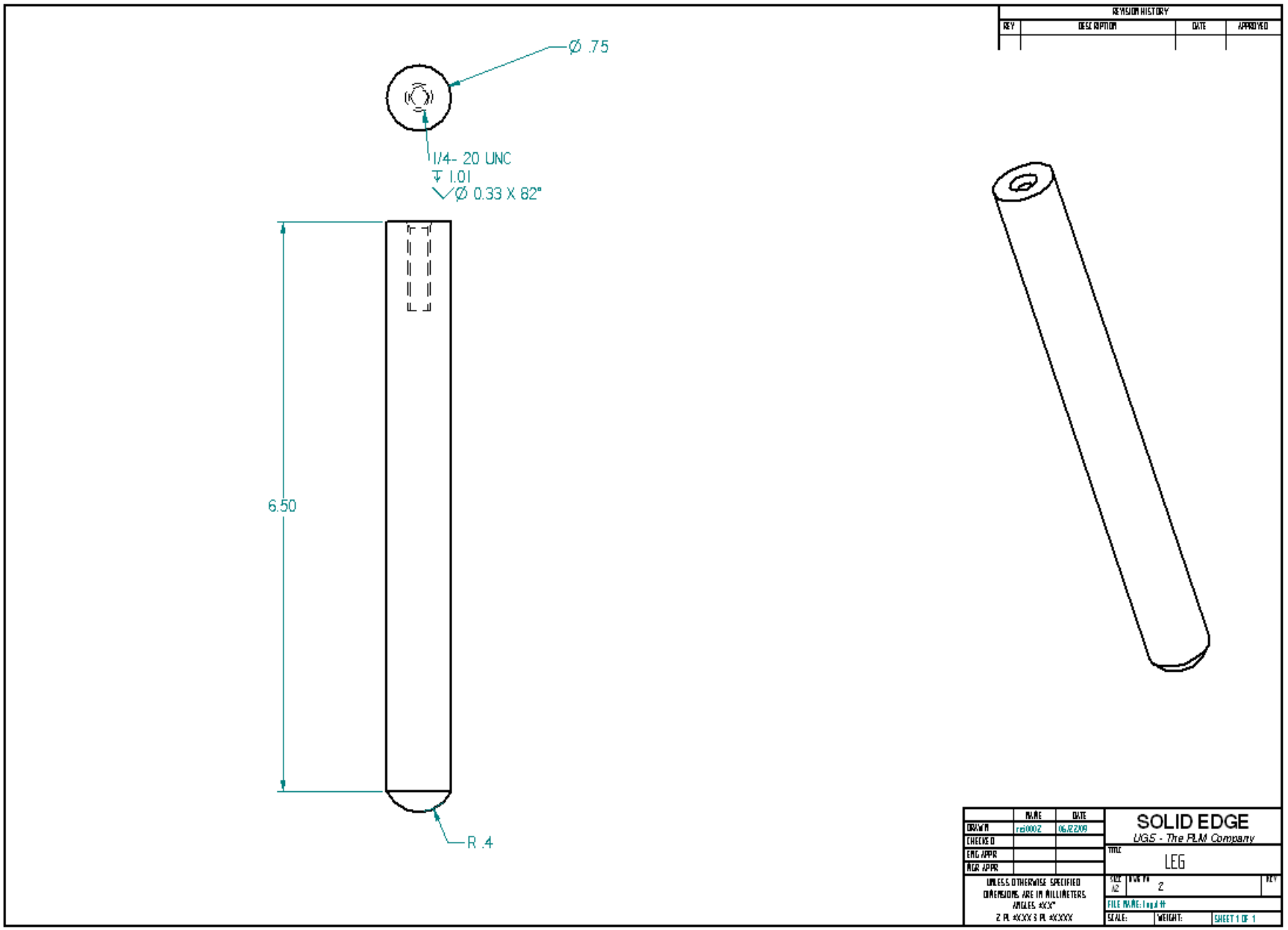
Ø .75
1/4- 20 UNC
↧ 1.01
⌵Ø 0.33 X 82°
6.50
R .4
REVISION HISTORY
REV
DESCRIPTION
DATE
APPROVED
NAME
DATE
DRAWN
rs10002
06/12/2009
CHECKED
ENG APPR.
MFG APPR.
UNLESS OTHERWISE SPECIFIED
DIMENSIONS ARE IN MILLIMETERS
ANGLES ±X°
2 PL ±XXX 3 PL ±XXXX
SOLID EDGE
UGS - The PLM Company
TITLE
LEG
SIZE
A2
DWG NO
2
REV
FILE NAME: leg.dft
SCALE:
WEIGHT:
SHEET 1 OF 1

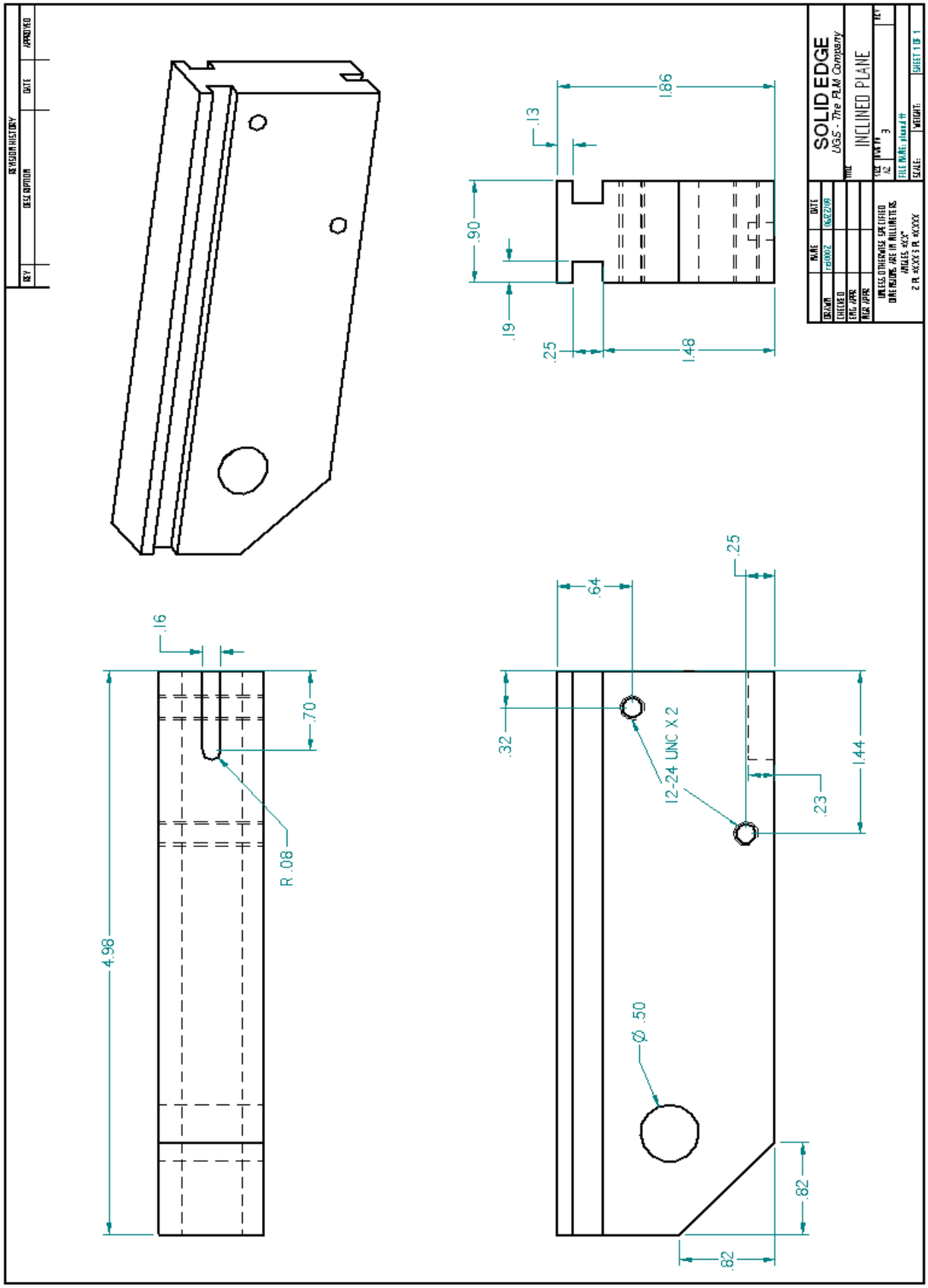
REVISION HISTORY
REV
DESCRIPTION
DATE
APPROVED
SOLID EDGE
UGS - The PLM Company
INCLINED PLANE
DRAWN
CHECKED
ENG APPR.
MFG APPR.
NAME
DATE
SIZE
DWG NO.
REV
SCALE:
WEIGHT:
SHEET 1 OF 1
UNLESS OTHERWISE SPECIFIED
DIMENSIONS ARE IN MILLIMETERS.
ANGLES ±X°
2 PL ±XXX 3 PL ±XXXX
.13
1.86
.90
.19
.25
1.48
.16
.70
R .08
4.98
.64
.25
.32
12-24 UNC X 2
.23
1.44
Ø .50
.82
.82

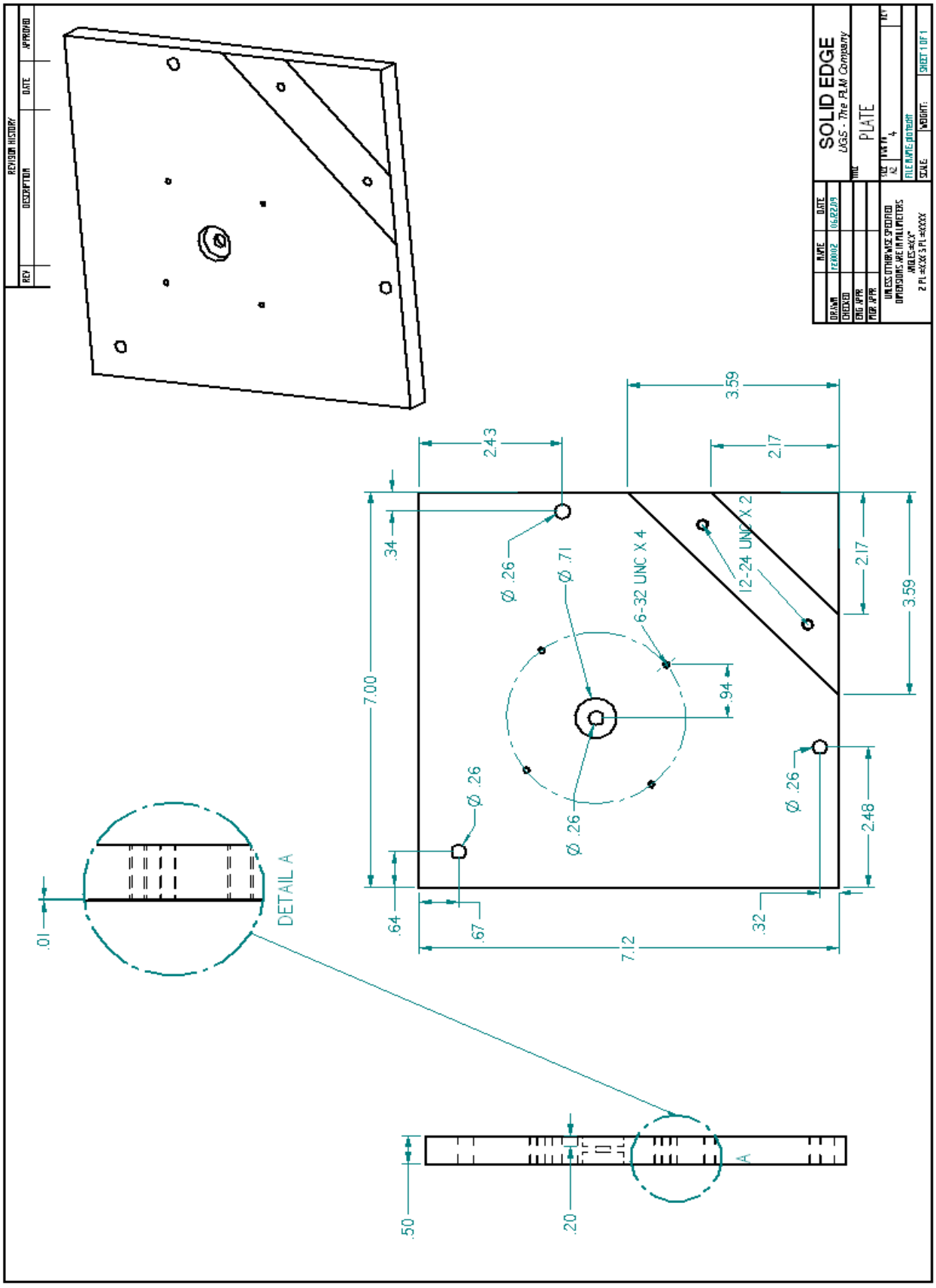
REVISION HISTORY
REV
DESCRIPTION
DATE
APPROVED
SOLID EDGE
UGS - The PLM Company
PLATE
DRAWN
CHECKED
ENG APPR.
MFG APPR.
NAME
DATE
UNLESS OTHERWISE SPECIFIED
DIMENSIONS ARE IN MILLIMETERS
ANGLES ±X.X°
2 PL ±X.XX 3 PL ±X.XXX
SIZE
SCALE:
WEIGHT:
SHEET 1 OF 1
FILE NAME: plate.par
3.59
2.43
2.17
.34
Ø .26
Ø .71
6-32 UNC X 4
12-24 UNC X 2
.94
7.00
2.17
3.59
Ø .26
Ø .26
Ø .26
2.48
.64
.67
7.12
.32
DETAIL A
.01
.50
.20
A

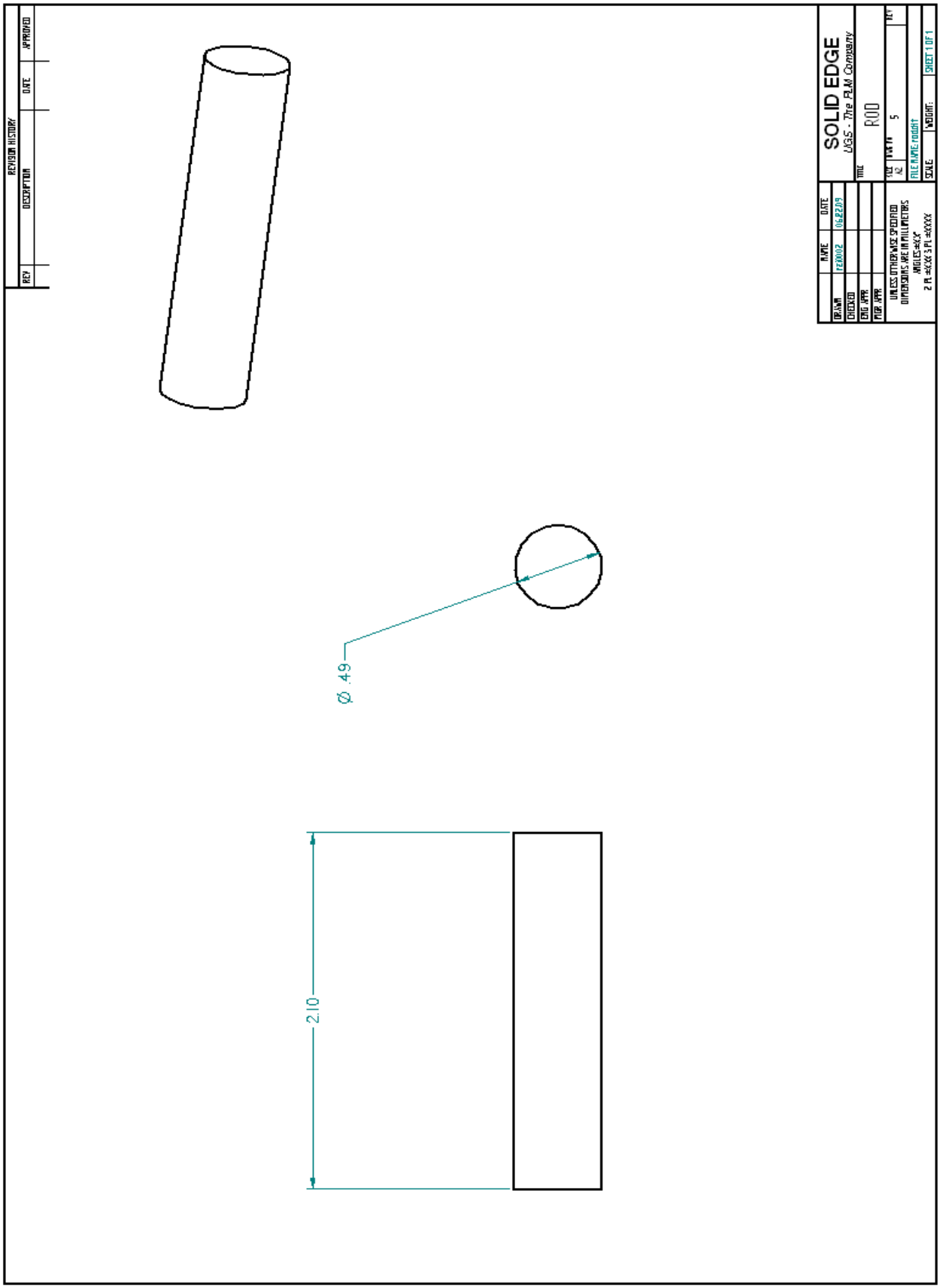
REVISION HISTORY
REV
DESCRIPTION
DATE
APPROVED
Ø .49
2.10
SOLID EDGE
VGS - The PLM Company
NAME
DATE
DRAWN
rzamora
06-22-09
CHECKED
ENG APPR.
MFG APPR.
UNLESS OTHERWISE SPECIFIED
DIMENSIONS ARE IN MILLIMETERS
ANGLES ±X.X°
2 PL ±X.XX 3 PL ±X.XXX
TITLE
ROD
SIZE
A2
DWG NO.
5
REV
FILE NAME: rodddft
SCALE:
WEIGHT:
SHEET 1 OF 1

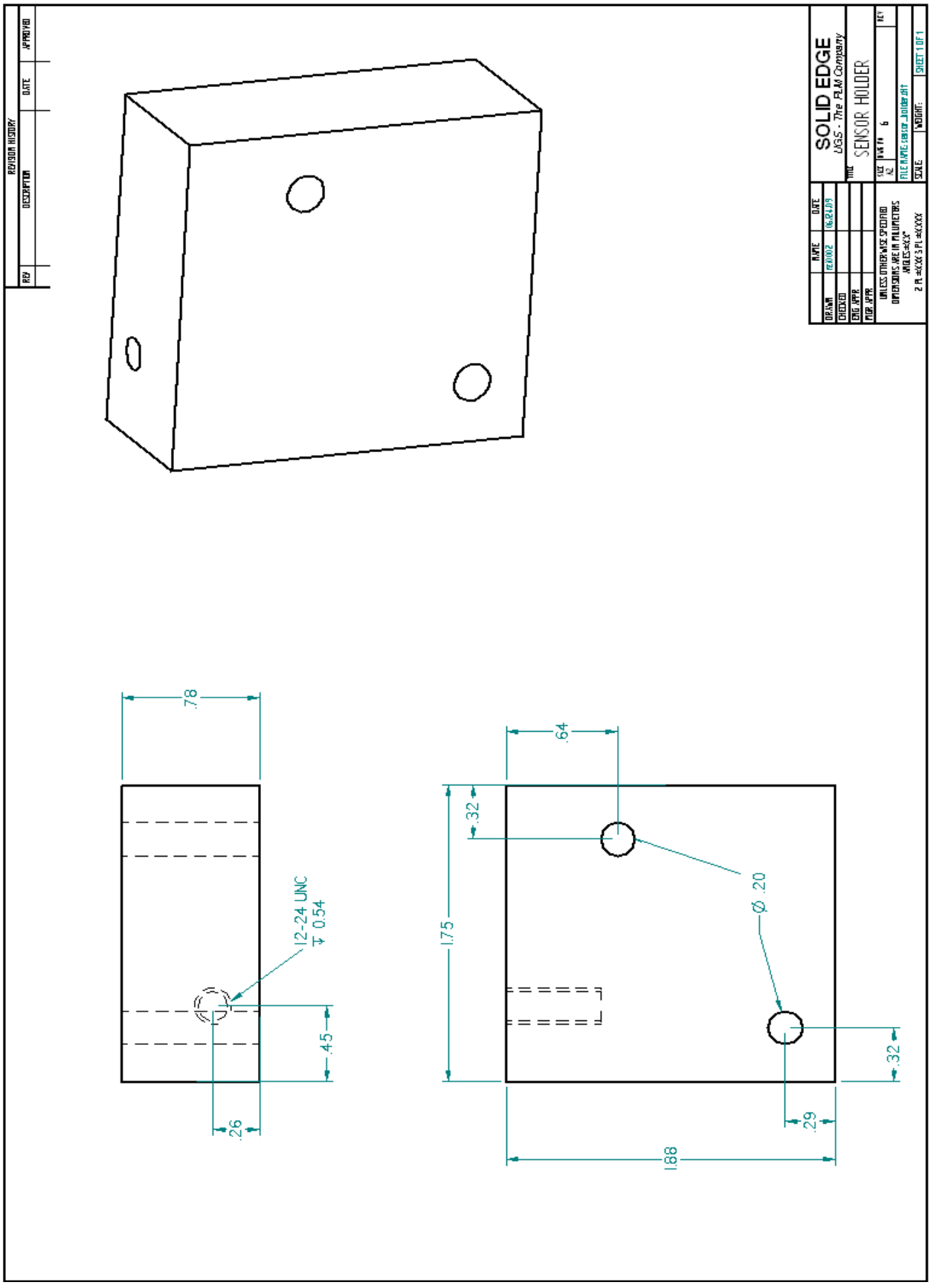
REVISION HISTORY
REV
DESCRIPTION
DATE
APPROVED
SOLID EDGE
UGS - The PLM Company
NAME
DATE
DRAWN
12/31/02
06/24/09
CHECKED
ENG APPR.
MFG APPR.
UNLESS OTHERWISE SPECIFIED
DIMENSIONS ARE IN MILLIMETERS
ANGLES ±X°
2 PL ±X.XX 3 PL ±X.XXX
TITLE
SENSOR HOLDER
SIZE
A2
DWG NO
6
REV
FILE NAME: sensor_holder.dft
SCALE:
WEIGHT:
SHEET 1 OF 1
.78
12-24 UNC
↧ 0.54
.45
.26
.64
.32
1.75
Ø .20
.32
.29
1.88

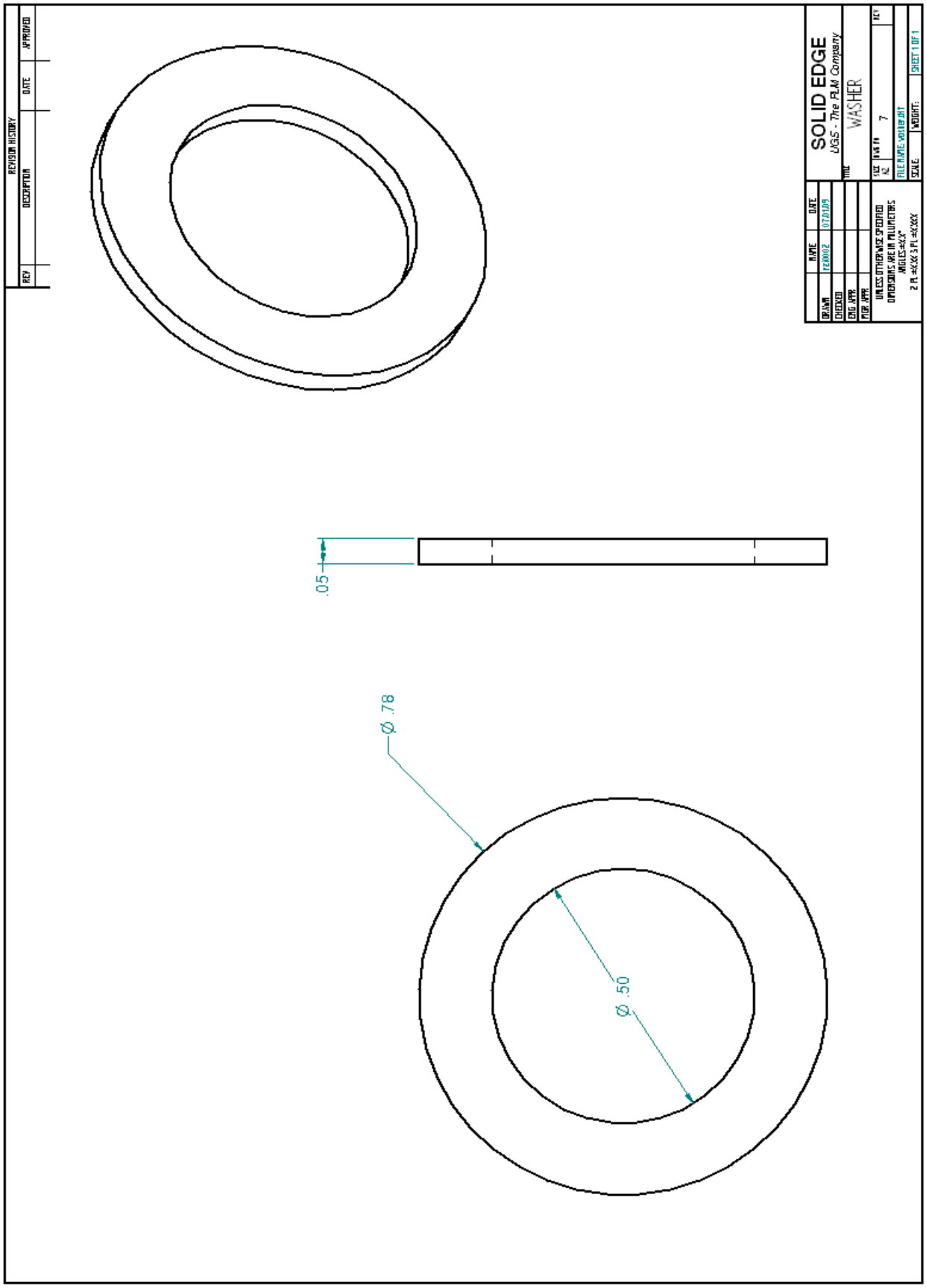
REVISION HISTORY
REV
DESCRIPTION
DATE
APPROVED
.05
Ø .78
Ø .50
SOLID EDGE
UGS - The PLM Company
WASHER
DRAWN
CHECKED
ENG APPR.
MFG APPR.
NAME
DATE
UNLESS OTHERWISE SPECIFIED
DIMENSIONS ARE IN MILLIMETERS
ANGLES: ±X.X°
2 PL ±X.XX 3 PL ±X.XXX
SIZE
A2
DWG NO
7
REV
FILE NAME: washer.dft
SCALE:
WEIGHT:
SHEET 1 OF 1

Appendix B- Electrical Drawing:

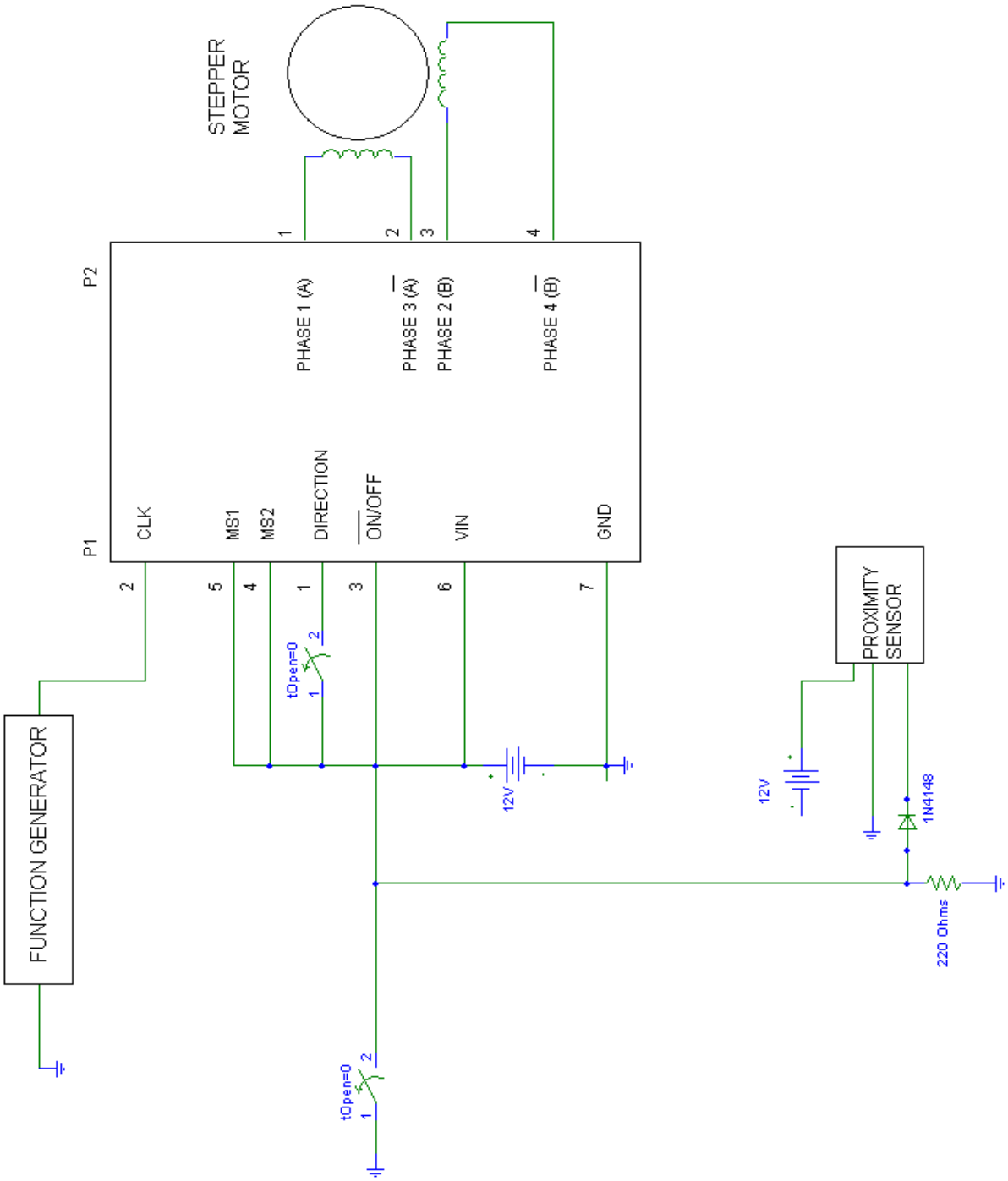

Figure B-1 Electrical Drawing of Motorized Inclined Plane

Appendix C- Uncertainty of Experiment

The instrument uncertainties of the experiments discussed in Chapter 2 are associated with the angle meter, the weight set, and the thermometer which will be discussed for each one below.

The angle meter has an uncertainty of ±0.05°, which is the smallest fraction it indicates. The additional uncertainty is caused by the position of the angle meter (Figure C-1). The angle meter was equipped with a level (Figure C-2), which was used to make sure that one of the arms is parallel with the base. Using the geometric theorem that states: if two parallel lines are cut by a transverse line the alternate interior angles (caused by that line) are equal (Figure C-3); where the angle meter (the arm with the level) and the base are parallel lines, and the inclined plane and the other arm of the angle meter are intersecting those lines. Because the "bubble" in the level could not be perfectly centered; in fact there are two bounds, one lower bound (Figure C-4) and one upper bound (Figure C-5). The additional uncertainty caused by the position of the angle meter was found to be ±0.5°. Therefore the total uncertainty of the angle meter is ±0.55°. Taking that value (±0.55°) and entering it into equation 12 the uncertainty of the static friction coefficient is ±0.0096.

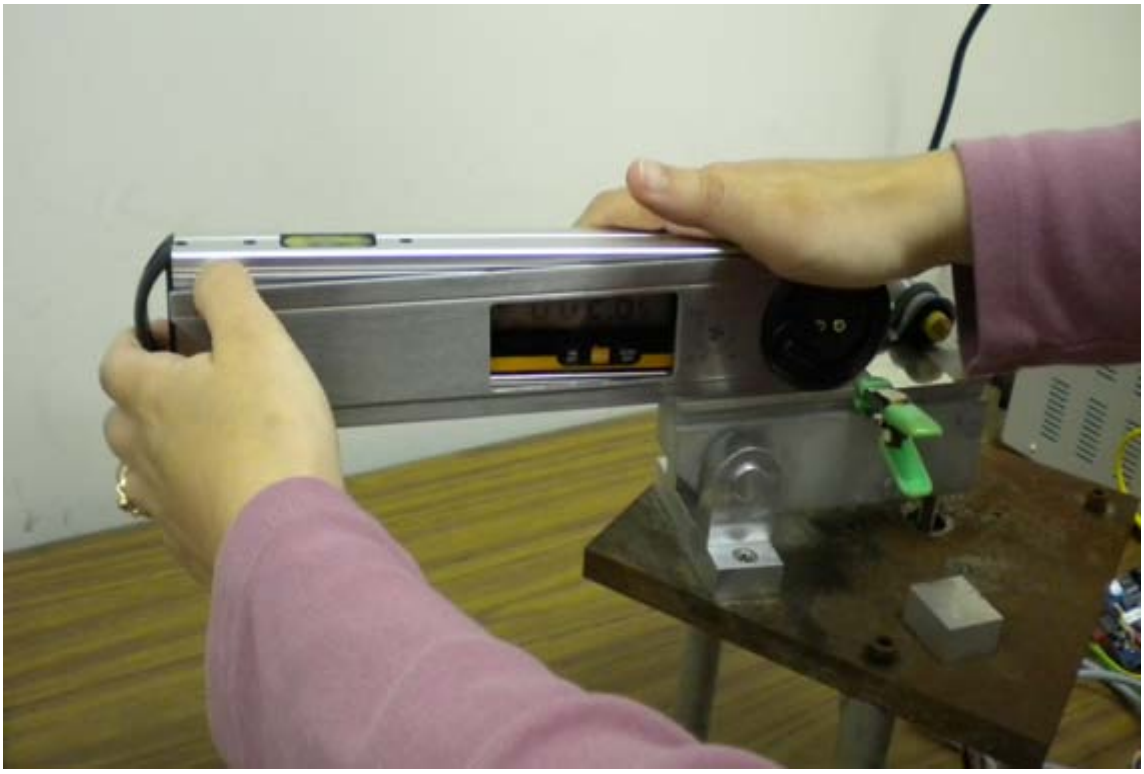

Figure C-1 Measuring theta

Figure C-2 Upper View of Level

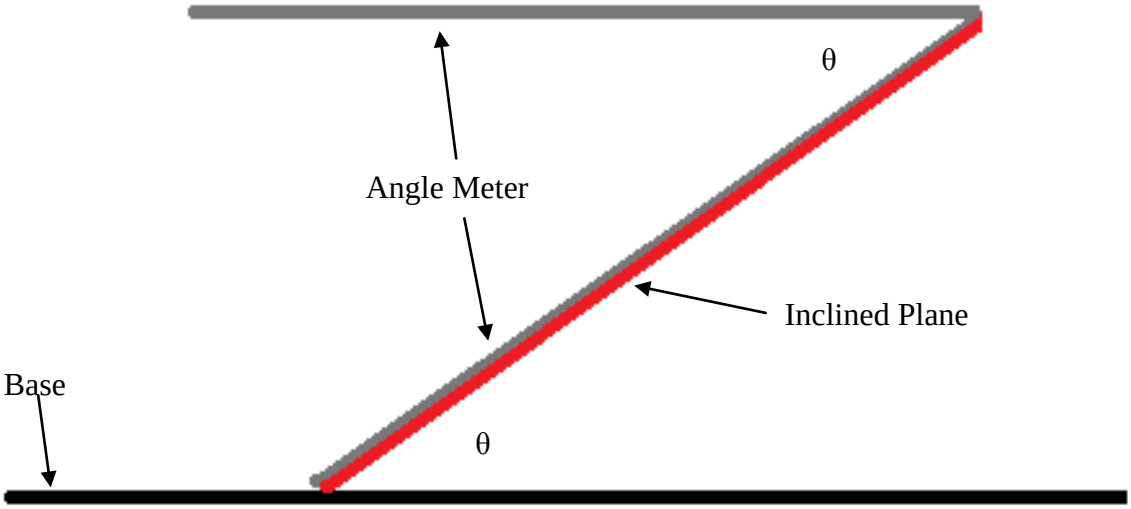

Figure C-3 Visual Display of Geometric Theorem Stating

Figure C-4 Lower Bound of the Level

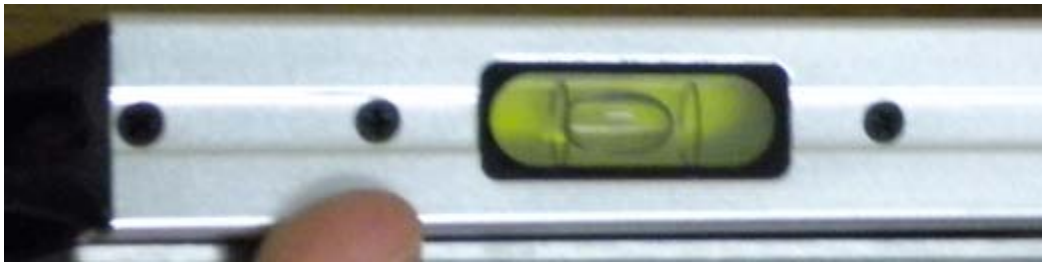

Figure C-5 High Bound of the Level

The specifications of the weight set state that the standard used was the International Organization of Legal Metrology M_2 tolerance. According to those standards (Weights of Classes E_1 E_2, F_1, F_2, M_1, M_{1-2}, M_2, M_{2-3}, and M_3, 2004), the uncertainty for 10 g, 20 g, and 50 g are ±6 mg, ±8 mg, and ±10 mg respectively. The masses listed in Table C-1 (which also display

the uncertainty) were compiled using various combinations of the masses listed in the previous sentence.

Table C-1 Uncertainty at Each Mass Tested

Mass (g)	Uncertainty (±mg)
70	18
100	32
130	42
160	56
190	66
220	80

According to the operating manual of the thermometer (which also came with a K-type thermocouple) the accuracy of the meter is ± (0.3% of the reading+2 °C). Because the temperature chamber door, had to be opened in order for the weight set (with sample adhered to it) to be placed on the inclined plane, the temperature changed. The temperature difference for each temperature is in Table C-2. The upper and lower bounds can be found and is listed in Table C-3.

Table C-2 Temperature Drop as Door Opens at each Temperature

Desired Temperature (°C)	Temperature Drop (°C)
-10	+3
10	+2
25	0
50	-2
75	-5
110	-10

Table C-3 Upper and Lower Bounds of the Temperature (including Temperature Drop)

Desired Temperature (°C)	Upper Bound (°C)	Lower Bound (°C)
-10	-5	-9
10	14	10
25	27	23
50	50	46
75	72	68
110	102	98

Appendix D- Second Order Normalization of all of the Samples

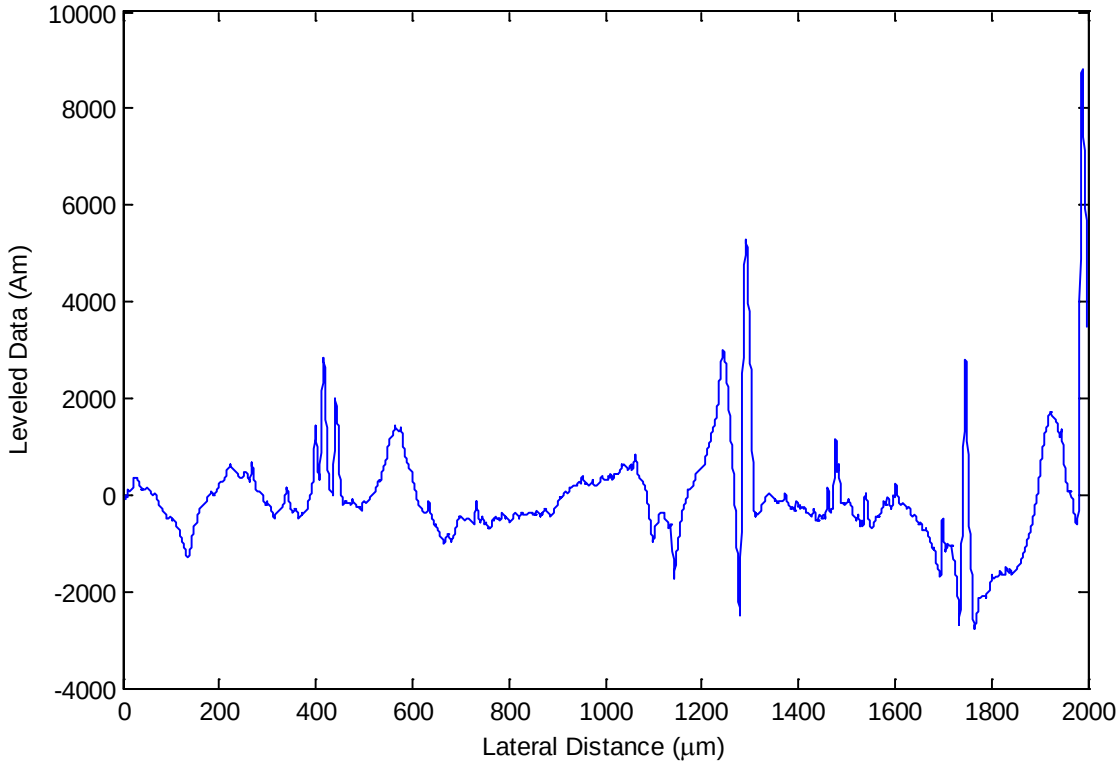

D-1 Second Order Normalization of Small Sample 1

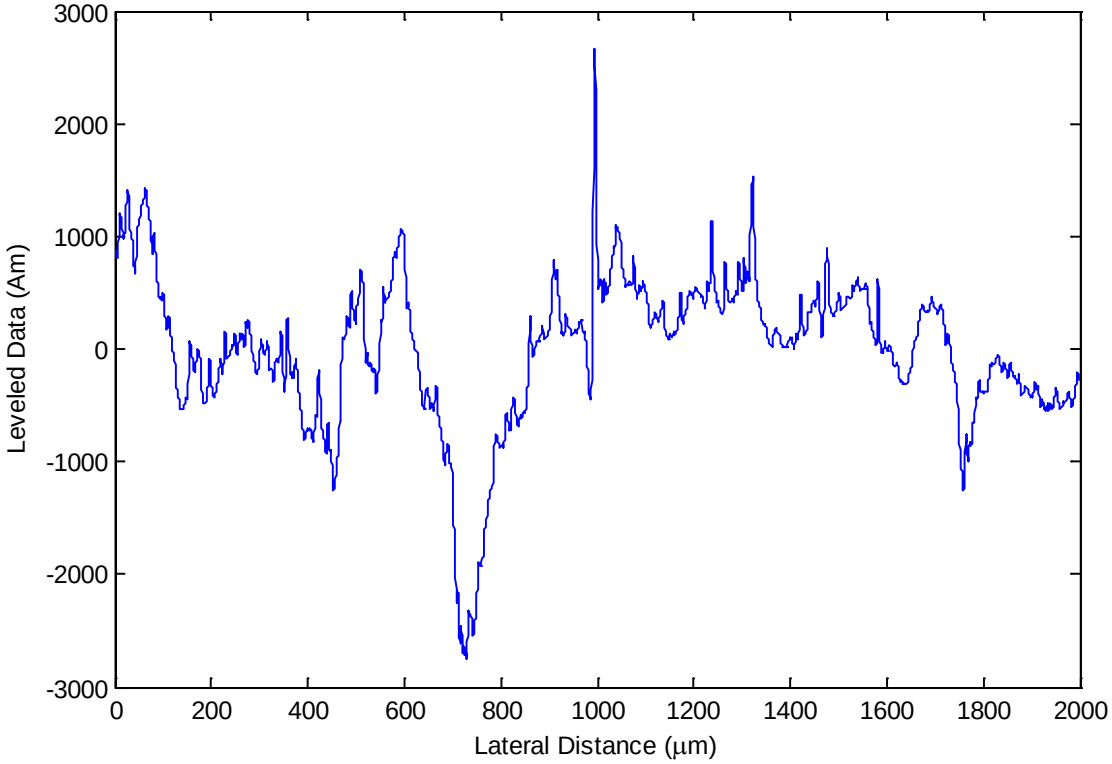

D-2 Second Order Normalization of Small Sample 2

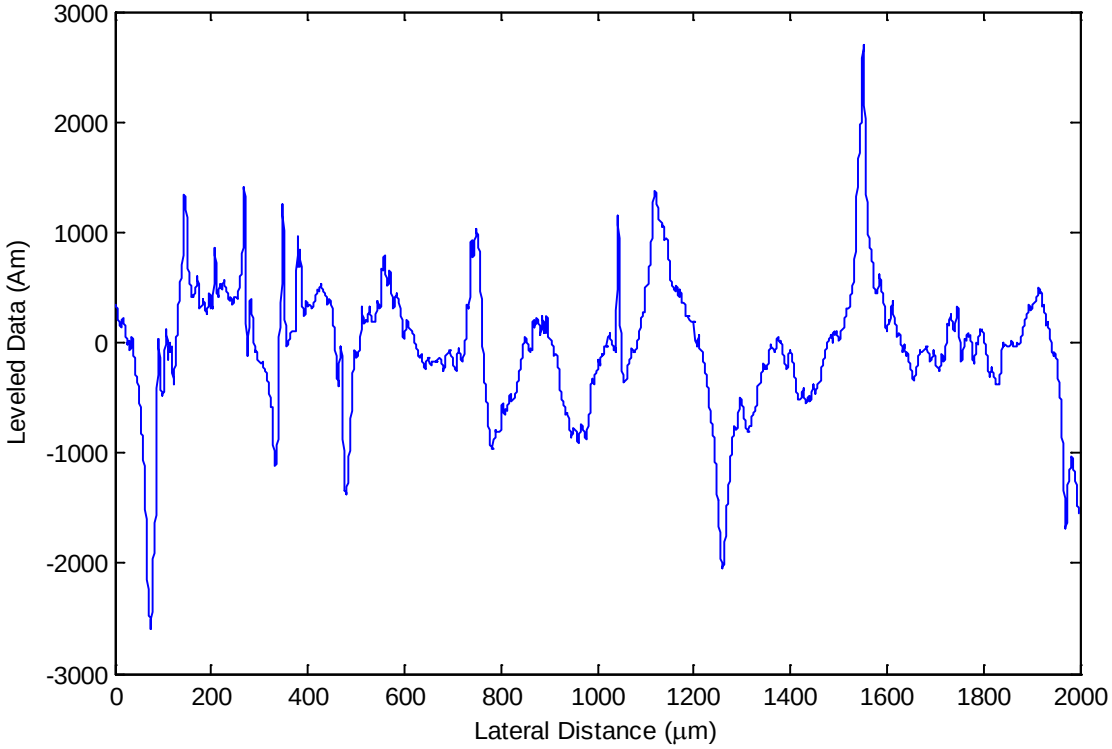

D-3 Second Order Normalization of Small Sample 3

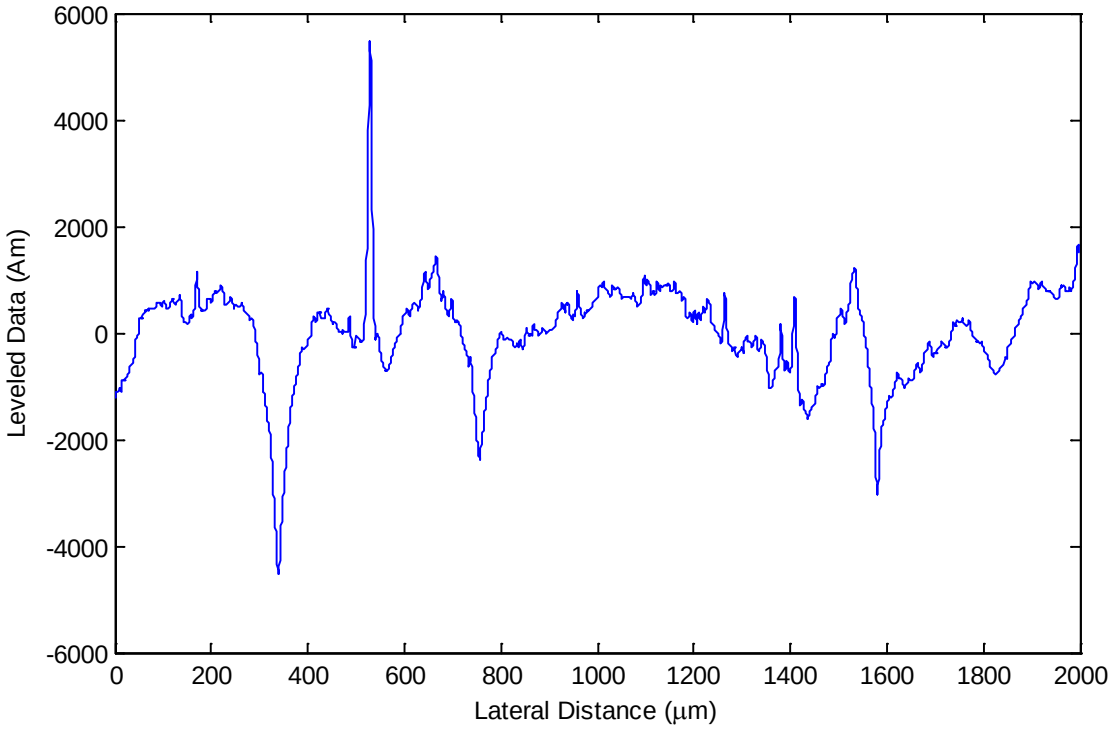

D-4 Second Order Normalization of Small Sample 4

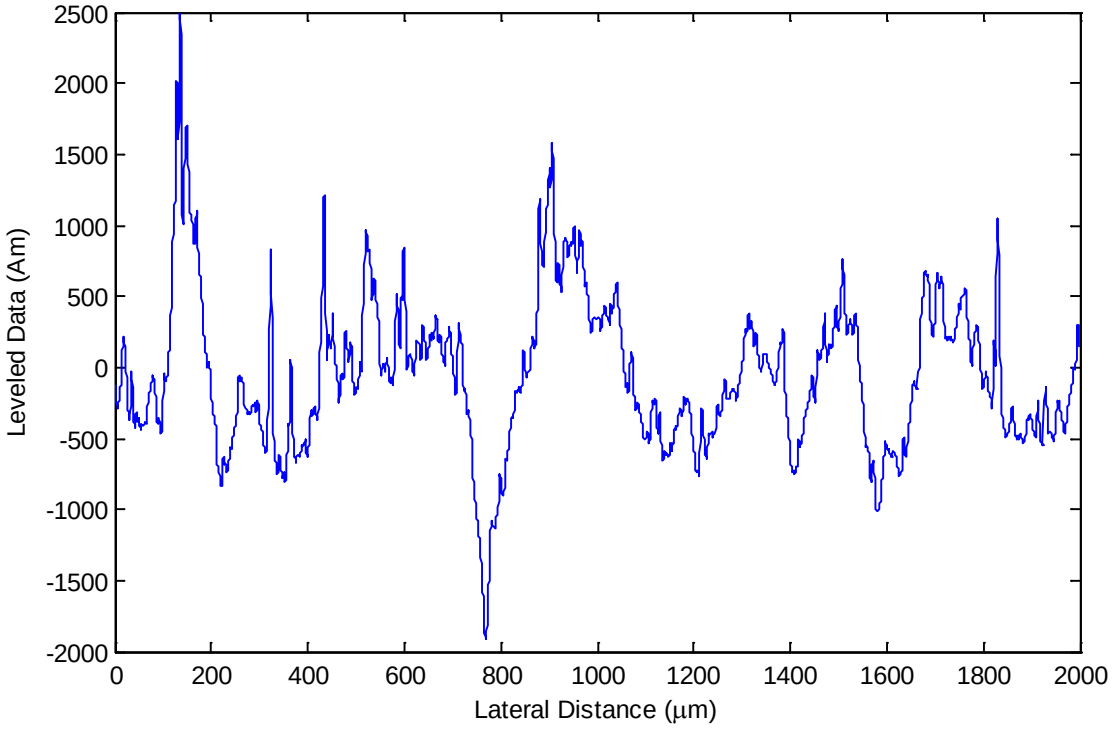

D-5 Second Order Normalization of Small Sample 5

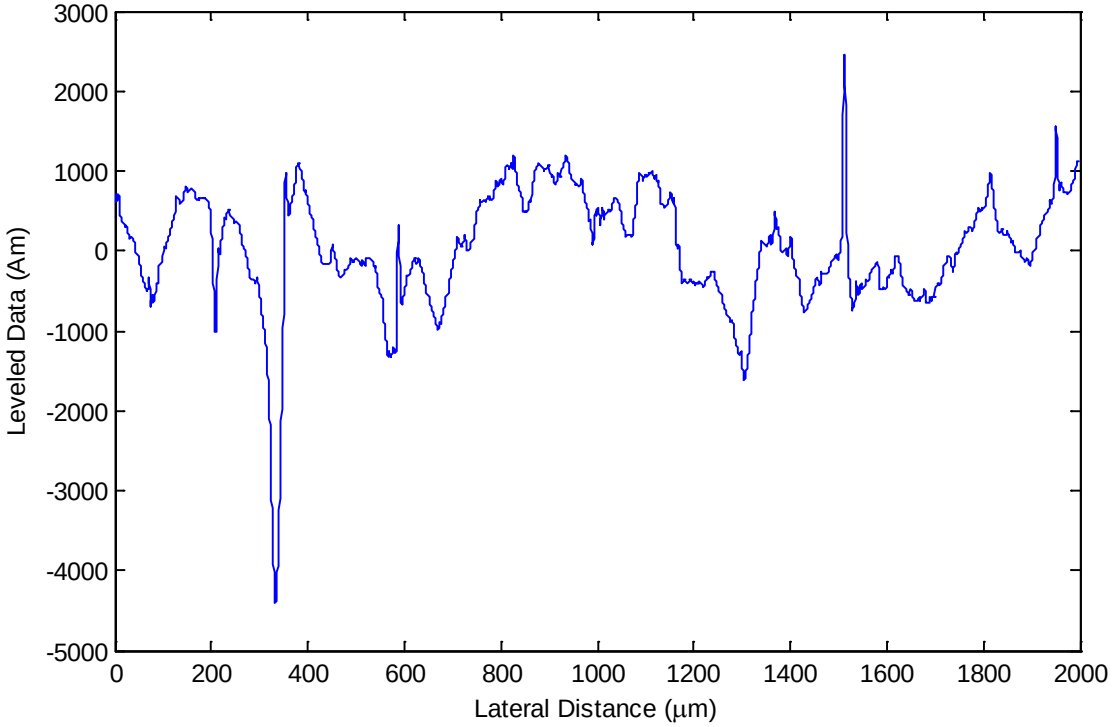

D-6 Second Order Normalization of Small Sample 6

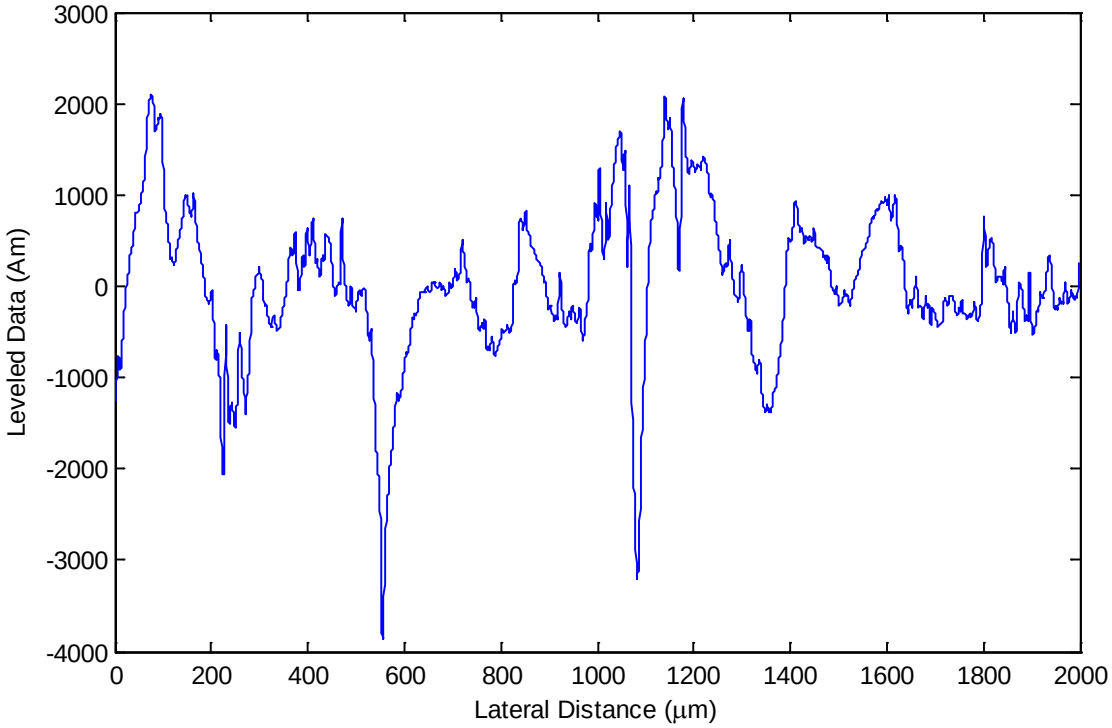

D-7 Second Order Normalization of Small Sample 7

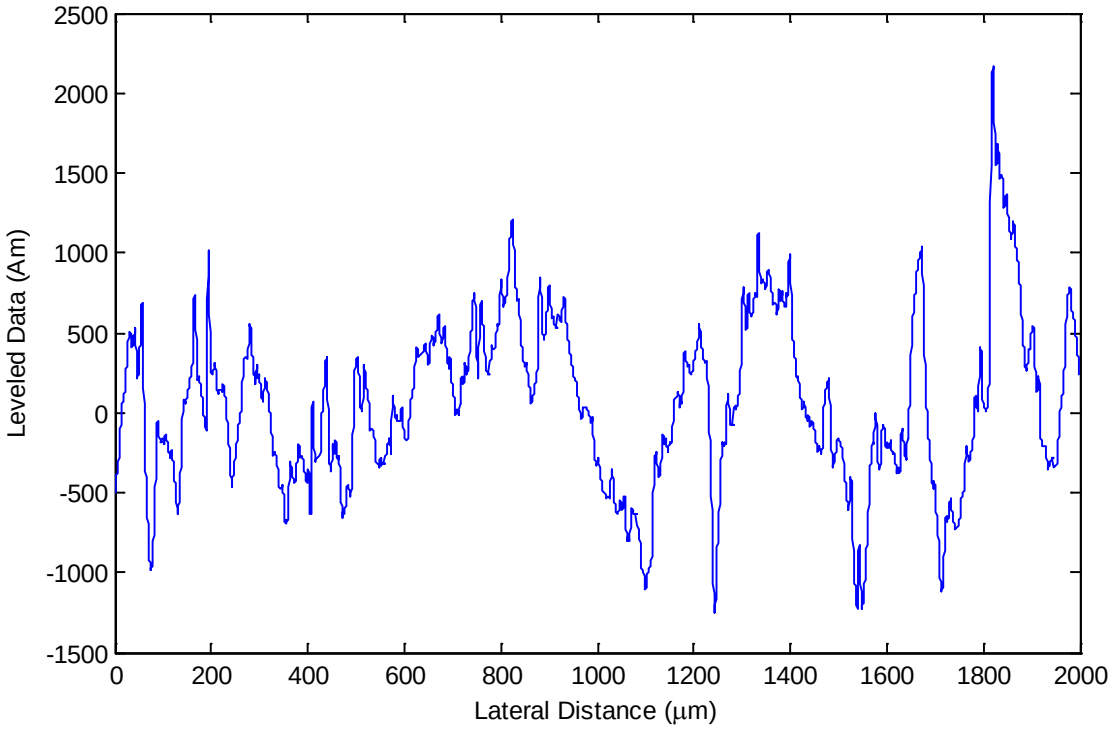

D-8 Second Order Normalization of Small Sample 8

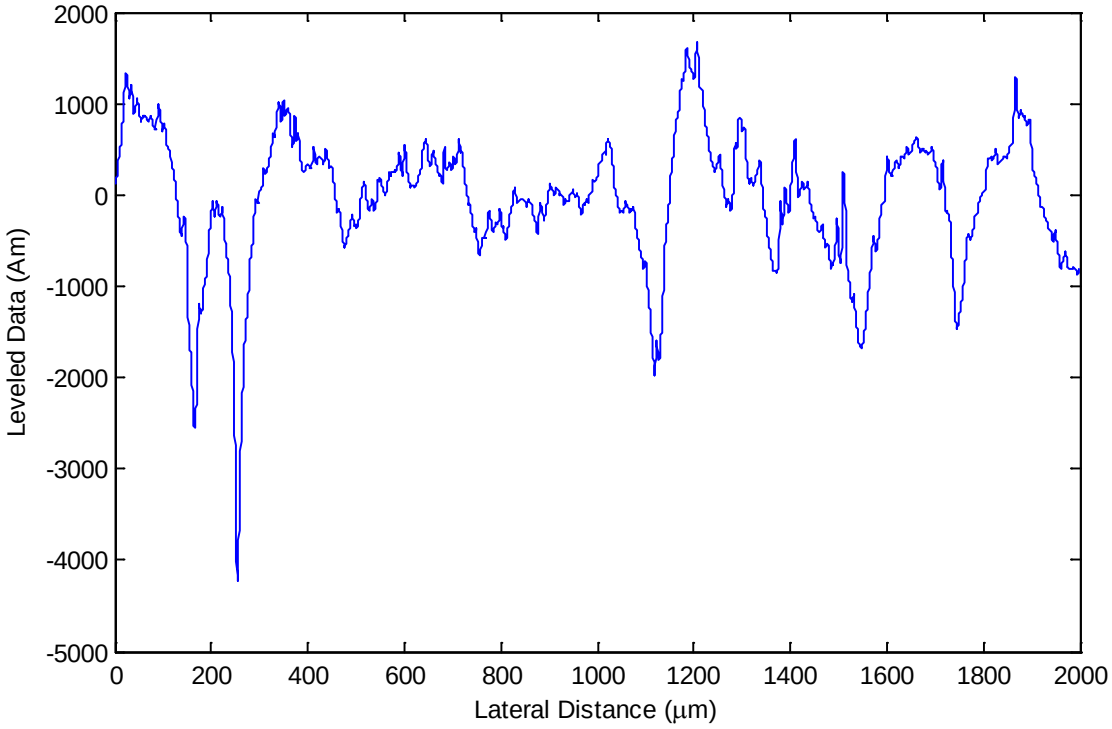

D-9 Second Order Normalization of Small Sample 9

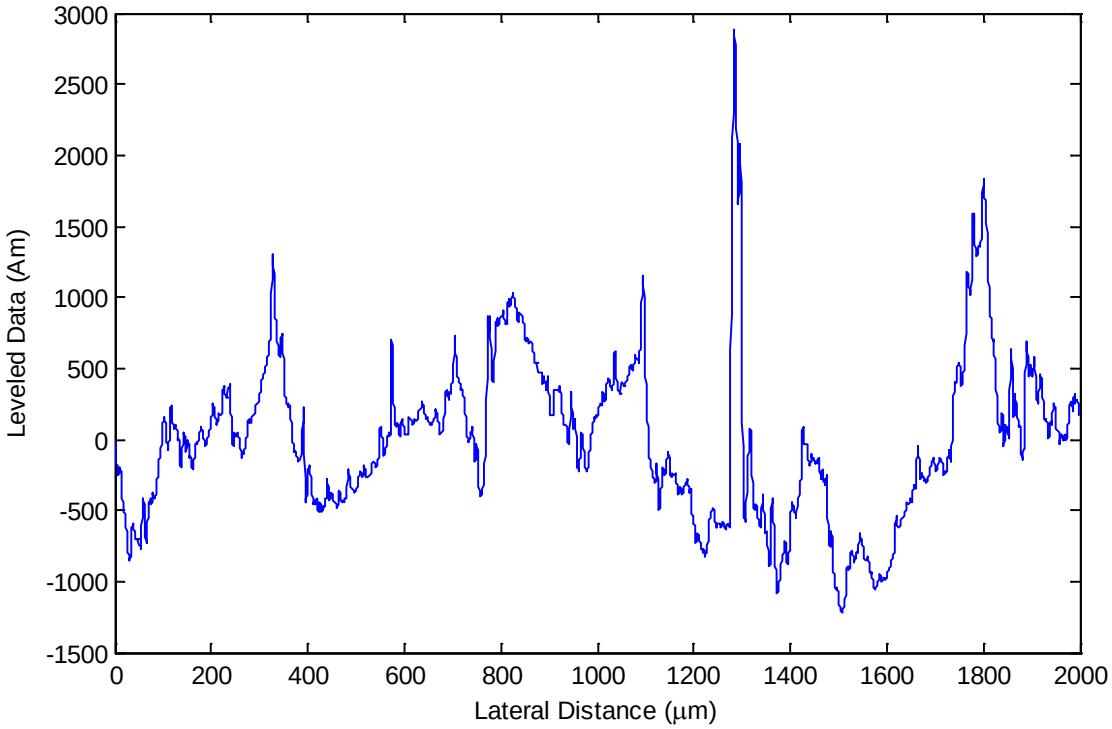

D-10 Second Order Normalization of Small Sample 10

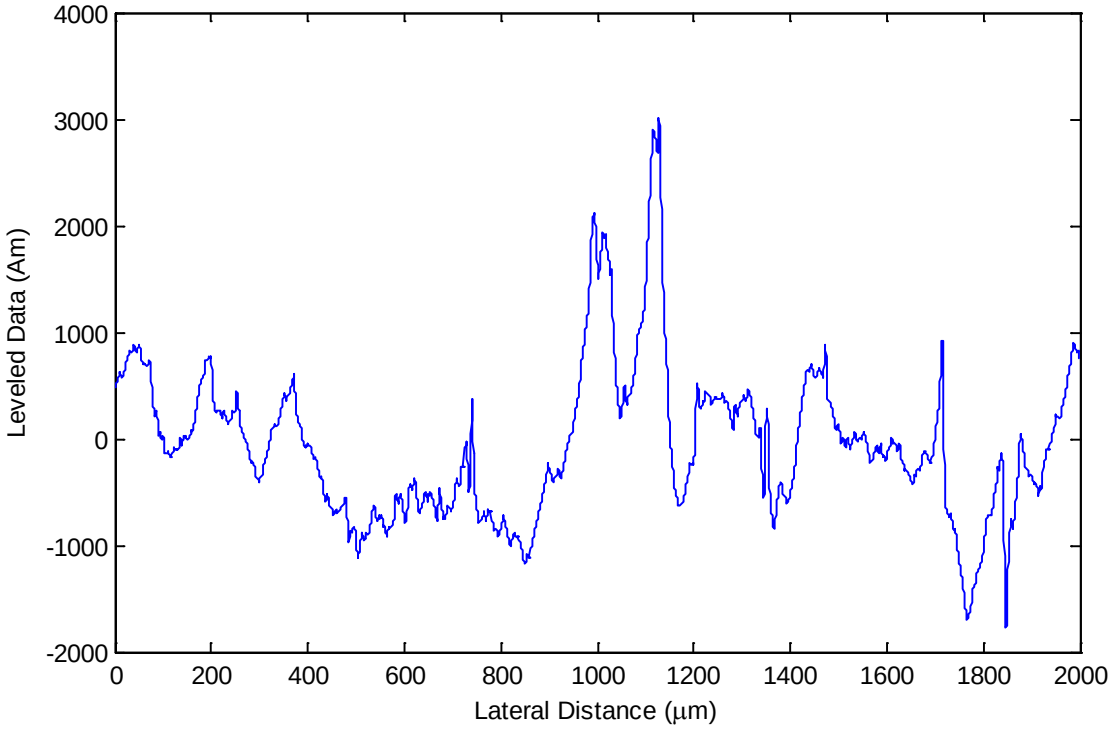

D-11 Second Order Normalization of Large Sample 1

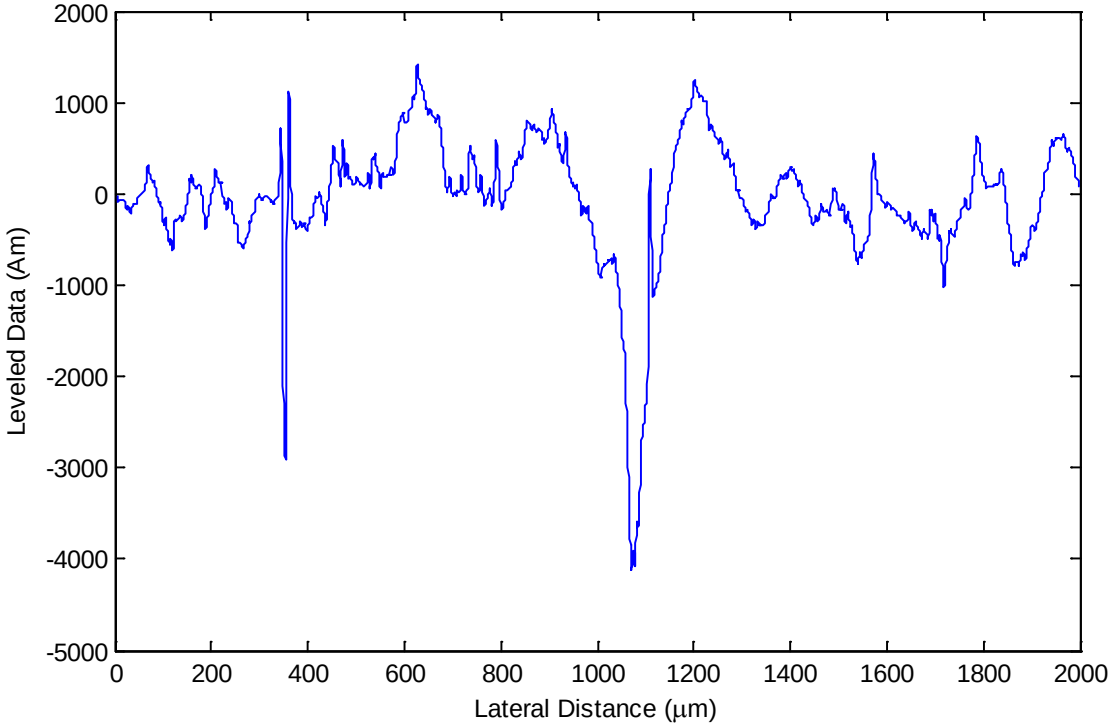

D-12 Second Order Normalization of Large Sample 2

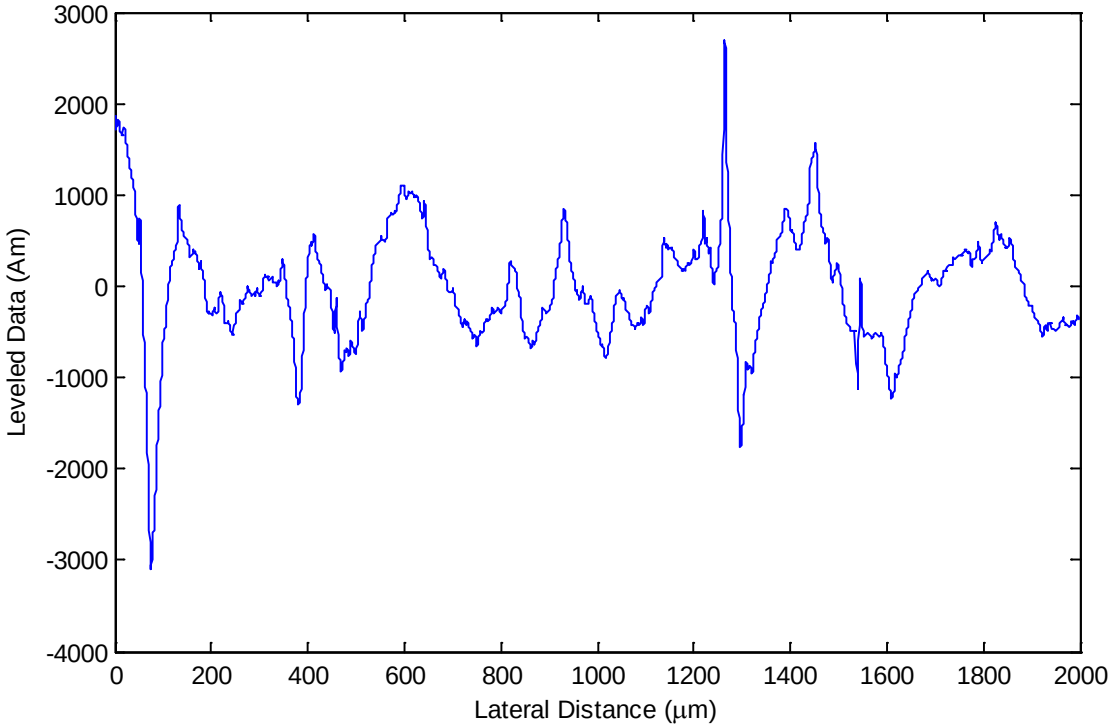

D-13 Second Order Normalization of Large Sample 3

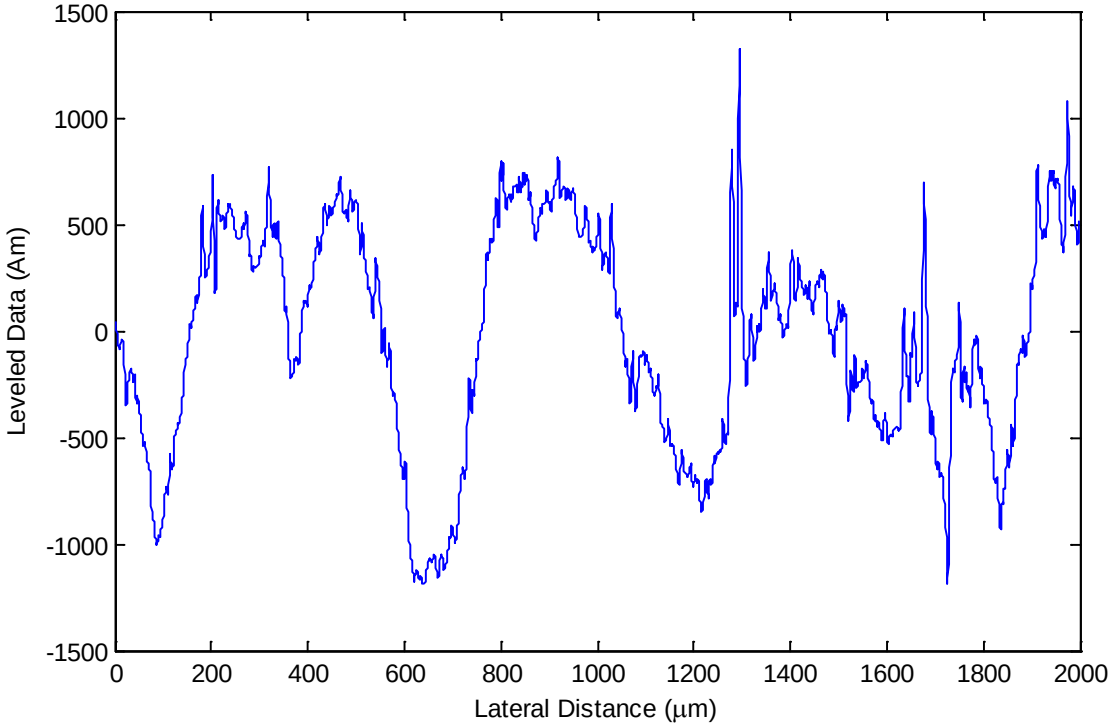

D-14 Second Order Normalization of Large Sample 4

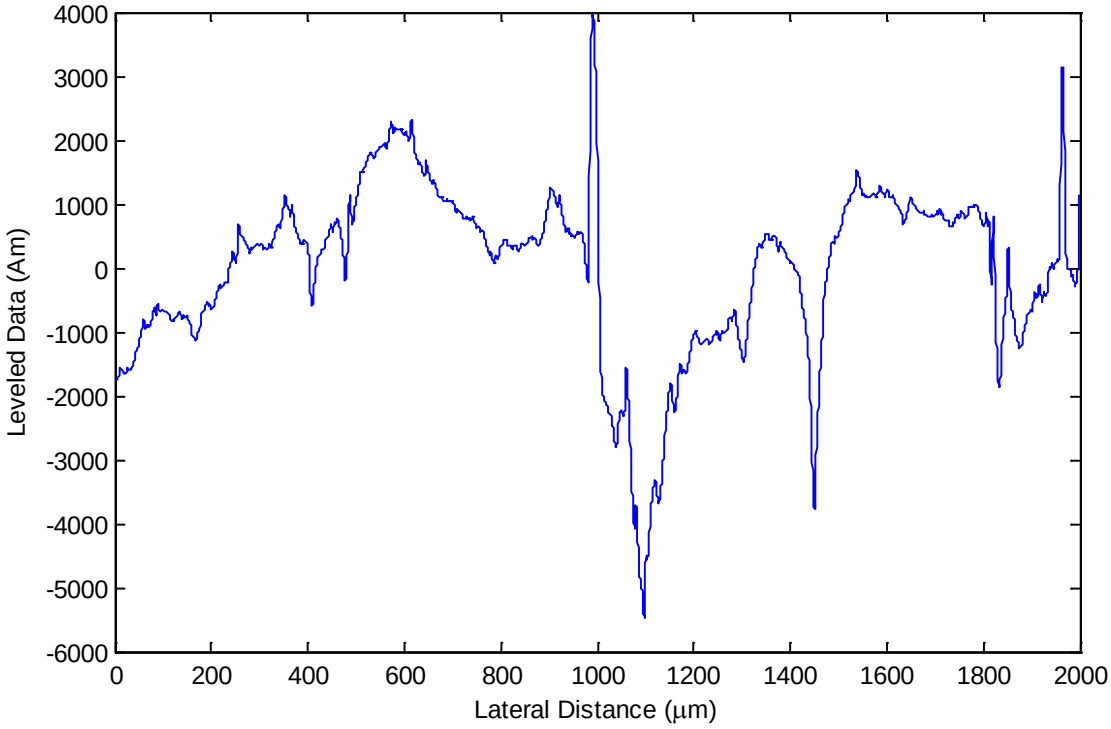

D-15 Second Order Normalization of Large Sample 5

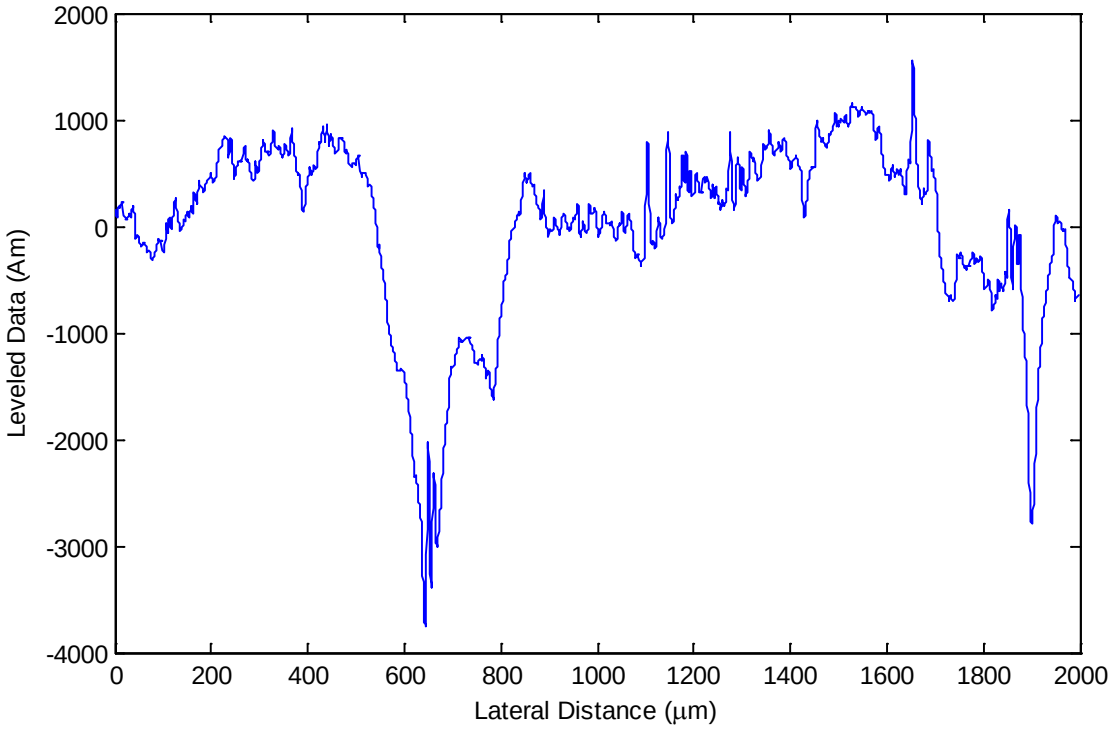

D-16 Second Order Normalization of Large Sample 6

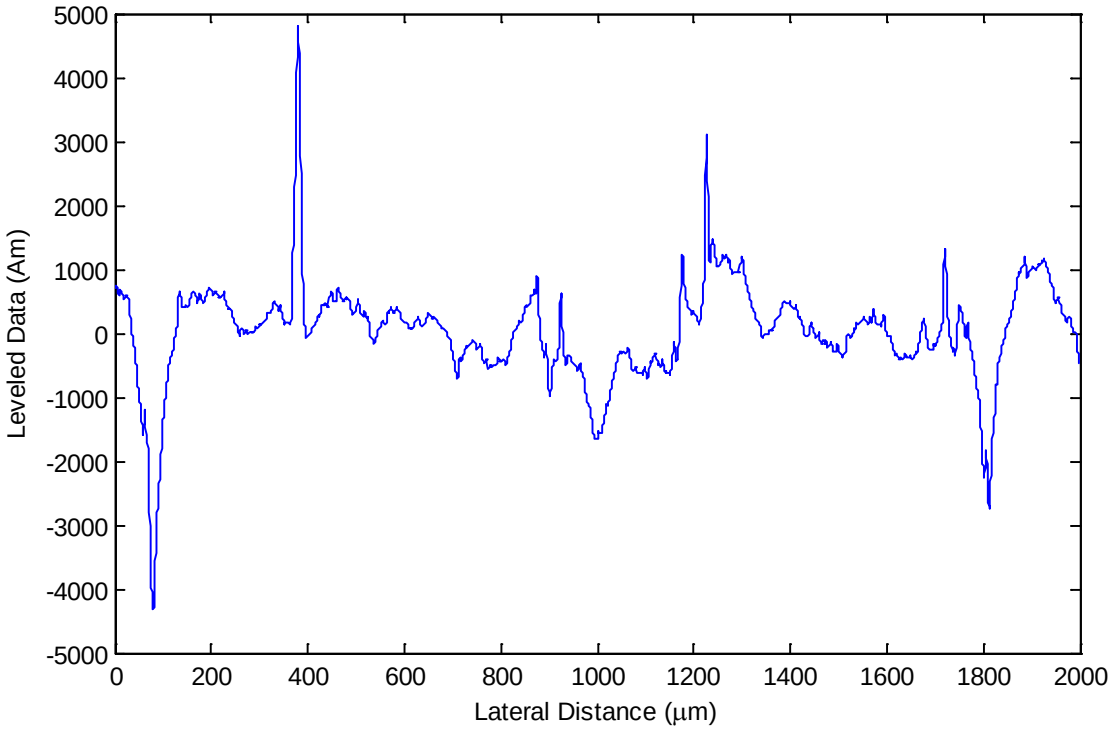

D-17 Second Order Normalization of Large Sample 7

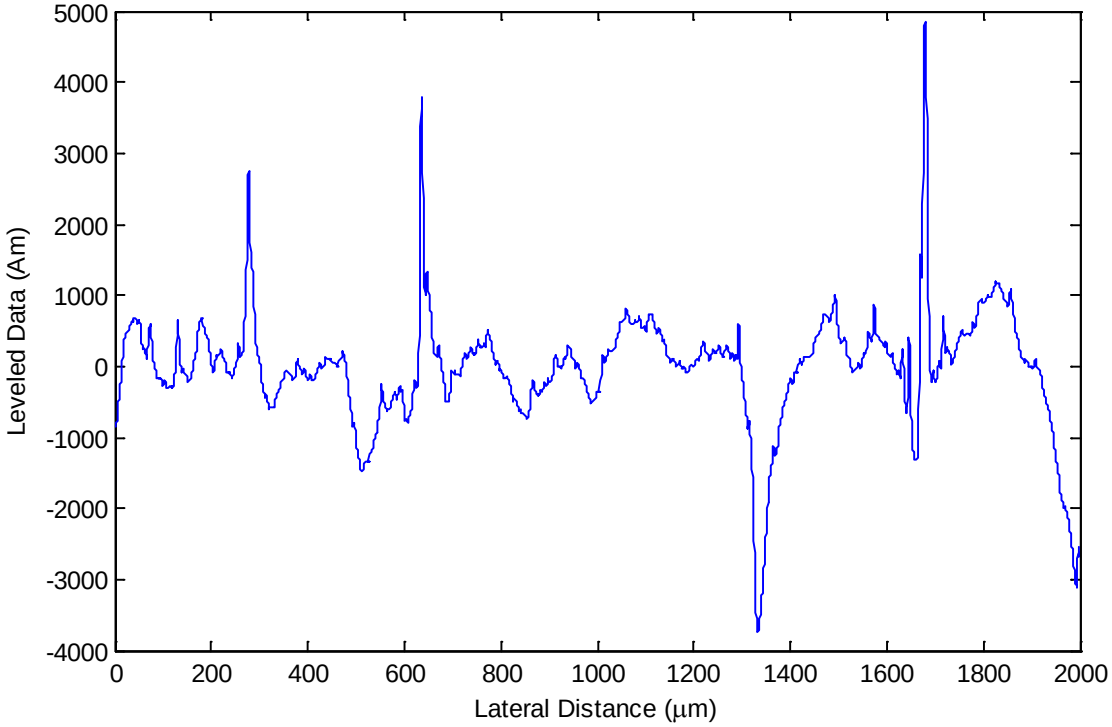

D-18 Second Order Normalization of Large Sample 8

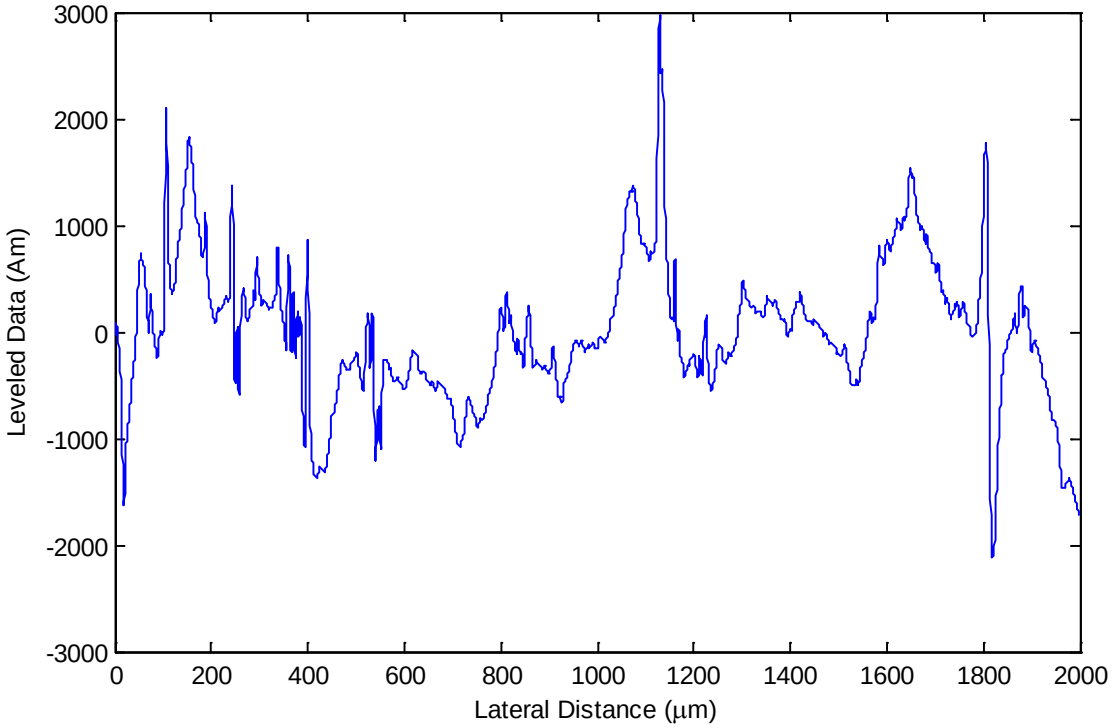

D-19 Second Order Normalization of Large Sample 9

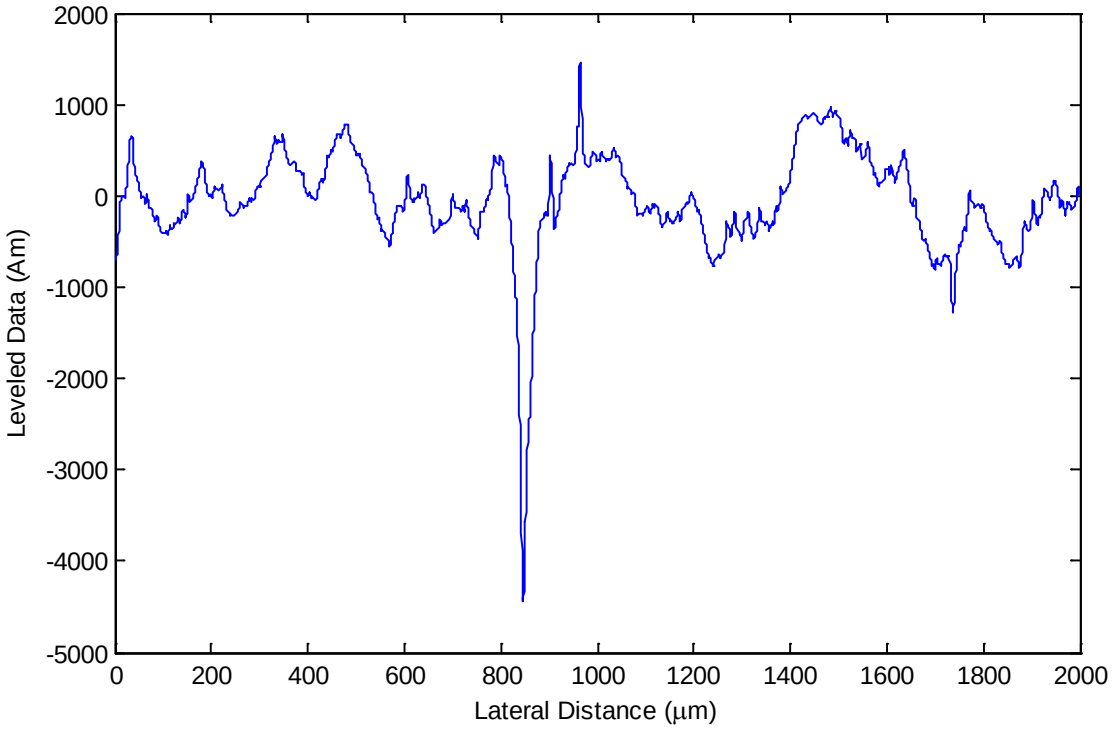

D-20 Second Order Normalization of Large Sample 10

Appendix E- Matlab Code Used to Find Plasticity Index

```
%zl= Profile Heights of the Average of all ten
% Large Samples
%zu= Profile Heights of the Average of all ten
% Small Samples

%Spectral Moment m_0-lower
for i=1:1:n
    fl(i)=(zl(i)^2);
end
m_0l=sum(fl)/n;

%Spectral Moment m_0-upper
for i=1:1:n
    fu(i)=(zu(i)^2);
end
m_0u=sum(fu)/n;

m_0=(m_0l)+(m_0u);

%Spectral Moment m_2-lower
for i=1:1:n
    if i==1
        %Using forward difference approximation for the first
data point
        sl(i)=((zl(i+1)-zl(i))./(x(i+1)-x(i))).^2;
    elseif i==3900
        %Using backward difference approximation for the last
data point
        sl(i)=((zl(i)-zl(i-1))./(x(i)-x(i-1))).^2;
    else
        %Using centered difference approximation for the rest of
the data
        %points
        sl(i)=((zl(i+1)-zl(i-1))./(x(i+1)-x(i-1))).^2;
    end
end
m_2l=sum(sl)/n;

%Spectral Moment m_2-upper
for i=1:1:n
    if i==1
        %Using forward difference approximation for the first
data point
        su(i)=((zu(i+1)-zu(i))./(x(i+1)-x(i))).^2;
    elseif i==3900
```

```
        %Using backward difference approximation for the last
data point
        su(i)=((zu(i)-zu(i-1))./(x(i)-x(i-1))).^2;
    else
        %Using centered difference approximation for the rest of
the data
        %points
        su(i)=((zu(i+1)-zu(i-1))./(x(i+1)-x(i-1))).^2;
    end
end
m_2u=sum(su)/n;

m_2=(m_2u)+(m_2l);

%Spectral Moment m_4-lower
for i=1:1:n
    if i==1
        %Using forward difference approximation for the first
data point
        hl(i)=((zl(i+2)-(zl(i+1).*2)+zl(i))./((x(i+2)-
x(i+1))*(x(i+1)-x(i)))).^2;
    elseif i==3900
        %Using backward difference approximation for the first
data point
        hl(i)=((zl(i)-(zl(i-1).*2)+zl(i-2))./((x(i-1)-x(i-
2))*(x(i)-x(i-1)))).^2;
    else
        %Using centered difference approximation for the rest of
the data
        %points
        hl(i)=((zl(i+1)-(zl(i).*2)+zl(i-1))./((x(i)-x(i-
1))*(x(i+1)-x(i)))).^2;
    end
end
m_4l=sum(hl)/n;

%Spectral Moment m_4-upper
for i=1:1:n
    if i==1
        %Using forward difference approximation for the first
data point
        hu(i)=((zu(i+2)-(zu(i+1).*2)+zu(i))./((x(i+2)-
x(i+1))*(x(i+1)-x(i)))).^2;
    elseif i==3900
        %Using backward difference approximation for the first
data point
```

```
        hu(i)=((zu(i)-(zu(i-1).*2)+zu(i-2))./((x(i-1)-x(i-
2))*(x(i)-x(i-1)))).^2;
    else
        %Using centered difference approximation for the rest of
the data
        %points
        hu(i)=((zu(i+1)-(zu(i).*2)+zu(i-1))./((x(i)-x(i-
1))*(x(i+1)-x(i)))).^2;
    end
end
m_4u=sum(hu)/n;

m_4=(m_4u)+(m_4l);

%Radius of Curvature
R=0.375*sqrt(pi/m_4)

%Bandwidth Paramenter
alpha=(m_0*m_4)/((m_2)^2);

%Asperity height standard deviation
sigma=sqrt(1-(0.8968/alpha))*sqrt(m_0)

%Material properties of tin(Metals Handbook edited by J.R Davis)
Y=9*(10^6); %Yield Strength (N/m^2)
v=0.33; %Poisson's Ratio
E=44.3*(10^9); % Young's Modulus (N/m^2)

%Hertz Modulus of Elasicity
bE1=(2*(1-(v.^2)))/E;
bE=1/bE1

%Function of Poission's Ratio
C=1.234+(1.256*v);

%Contact area:
A=(17*(10^-3))^2; % (m^2)

%Plasticity index
Pl=sqrt(sigma/R)*((2*bE)/(C*(1-(v^2))*pi*Y))
```

Appendix F- Temperature Dependent Material Properties

Table F-1 Temperature Dependent Thermal Conductivity of Tin Plated Copper and Rigid Tin Plated Copper (Touloukian et. al, 1970 and www.matweb.com)

Temperature (°C)	Thermal Conductivity (W/m-°C)
20	160
56.2	164
119	181
201.2	203
316.2	223
422.2	277
500.7	256

Table F-2 Temperature Dependent Thermal Expansion of Tin Plated Copper and Rigid Tin Plated Copper (Touloukian et. al, 1970 and www.matweb.com)

Temperature (°C)	Thermal Expansion (1/°C)
20	1.63E-5
127	1.67E-5
227	1.78E-5
327	1.87E-5
427	1.95E-5
527	2.09E-5
627	2.13E-5
727	2.16E-5

Table F-3 Temperature Dependent Thermal Conductivity of Silicone Rubber (Touloukian et. al, 1970)

Temperature (°C)	Thermal Conductivity (W/m-°C)
37.9	0.197
149.1	0.192
204.6	0.192
260.2	0.172

Table F-4 Temperature Dependent Thermal Expansion of Silicone Rubber (Touloukian et. al, 1970 and www.matweb.com)

Temperature (°C)	Thermal Expansion (1/°C)
-173	1.08E-4
-153	1.14E-4
-113	1.26E-4
-73	1.36E-4
-53	1.39E-4
-33	1.40E-4
-13	1.40E-4
0.2	1.40E-4
7	1.40E-4
27	1.40E-4
47	1.49E-4
67	1.55E-4

Table F-5 Temperature Dependent Thermal Conductivity of Copper (Touloukian et. al, 1970 and www.matweb.com)

Temperature (°C)	Thermal Conductivity (W/m-°C)
-173	483
0	401
20	385
27	398

Table F-6 Temperature Dependent Thermal Expansion of Copper (Touloukian et. al, 1970 and www.matweb.com)

Temperature (°C)	Thermal Expansion (1/°C)
20	1.64E-5
100	1.64E-5
250	1.85E-5
500	2.02E-5
925	2.48E-5

Table F-7 Temperature Dependent Young's Modulus of Tin Plated Copper (Upthegrove et al., 1956 and Olin Brass®)

Temperature (°C)	Young's Modulus (N/m^2)
20	1.297E11
23.89	1.180E11
148.89	1.180E11
204.44	1.042E11
260	1.042E11

Table F-8 Temperature Dependent Young's Modulus of Rigid Tin Plated Copper (Upthegrove et al., 1956 and Olin Brass®)

Temperature (°C)	Young's Modulus (N/m^2)
20	1.297E13
23.89	1.273E13
148.89	1.273E13
204.44	1.272E13
260	1.272E13

Table F-9 Temperature Dependent Young's Modulus of Silicone Rubber (Tran et al. 2001)

Temperature (°C)	Young's Modulus (N/m^2)
20	7.00E5
50	6.70E5
60	6.80E5
71	6.30E5
81	6.70E5
96	6.20E5
120	4.30E5
150	1.10E5

Table F-10 Temperature Dependent Young's Modulus of Copper
(Upthegrove et al., 1956 and www.matweb.com)

Temperature (°C)	Young's Modulus (N/m^2)
-196.11	1.238E11
-67.78	1.272E11
-40	1.155E11
20	1.2E11
23.89	6.792E10
100	6.792E10
204.44	1.038E11

Appendix G- Input File for Vibration Model

```
**
** PARTS
**
*Part, name=Ball_2D
*Element, type=CPS4R
** Section: Ball_2D
*Solid Section, elset=_PickedSet6, material=Ball
2.55,
*End Part
**
*Part, name=Blade_2D
*Element, type=CPS4R
** Section: Blade_2D
*Solid Section, elset=_PickedSet6, material=Star
1.5
*End Part
**
*Part, name=Receptacle_part_2D
*Element, type=CPS4R
** Section: Receptacle_nonrigid
*Solid Section, elset=_PickedSet45, material=Star
2.55,
** Section: Receptacle_rigid
*Solid Section, elset=_PickedSet44, material=Star_rigid
2.55,
*End Part
**
*Part, name=Spring_new
*Element, type=CPS4R
** Section: Spring_2D
*Solid Section, elset=_PickedSet14, material=Star
1.5,
** Section: Annulus
*Solid Section, elset=_PickedSet13, material=Star
1.9,
*End Part
**
*Element, type=CPS4R
** Section: Wire
*Solid Section, elset=_PickedSet10, material=Cable
1.12,
*End Part
**
**
** ASSEMBLY
```

```
**
*Assembly, name=Assembly
**
*Instance, name=Blade_2D-1, part=Blade_2D
*End Instance
**
*Instance, name=Receptacle_part_2D-1, part=Receptacle_part_2D
*End Instance
**
*Instance, name=Ball_2D-1, part=Ball_2D
*End Instance
**
*Instance, name=Ball_2D-2, part=Ball_2D
*End Instance
**
*Instance, name=Ball_2D-3, part=Ball_2D
*End Instance
**
*Instance, name=Wire_2D-1, part=Wire_2D
*End Instance
**
*Instance, name=Spring_new-1, part=Spring_new
*End Instance
**
*Surface, type=ELEMENT, name=_PickedSurf63, internal
*Surface, type=ELEMENT, name=_PickedSurf69, internal
*Surface, type=ELEMENT, name=_PickedSurf70, internal
*Surface, type=ELEMENT, name=_PickedSurf75, internal
*Surface, type=ELEMENT, name=_PickedSurf102, internal
*Surface, type=ELEMENT, name=_PickedSurf103, internal
*Surface, type=ELEMENT, name=_PickedSurf104, internal
*Surface, type=ELEMENT, name=_PickedSurf105, internal
*Surface, type=ELEMENT, name=_PickedSurf106, internal
*Surface, type=ELEMENT, name=_PickedSurf107, internal
** Constraint: Spring_rec
*Tie, name=Spring_rec, adjust=yes
_PickedSurf107, _PickedSurf106
** Constraint: ball-wire
*Tie, name=ball-wire, adjust=yes
_PickedSurf75, _PickedSurf63
** Constraint: rect-wire
*Tie, name=rect-wire, adjust=yes
_PickedSurf70, _PickedSurf69
*End Assembly
*Amplitude, name=Smooth_step, definition=SMOOTH STEP
0., 0., 0.1, 1.
```

```
*Amplitude, name=V25Hz, definition=PERIODIC
1, 157., 0.0001, 0.
0., 1.
*Amplitude, name=V30Hz, definition=PERIODIC
1, 188.4, 0.0001, 0.
0., 1.
*Amplitude, name=V35Hz, definition=PERIODIC
1, 219.8, 0.0001, 0.
0., 1.
*Amplitude, name=V40Hz, definition=PERIODIC
1, 251.2, 0.0001, 0.
0., 1.
*Amplitude, name=V45Hz, definition=PERIODIC
1, 282.6, 0.0001, 0.
0., 1.
*Amplitude, name=V50Hz, definition=PERIODIC
1, 314., 0.0001, 0.
0., 1.
*Amplitude, name=V55Hz, definition=PERIODIC
1, 345.4, 0.0001, 0.
0., 1.
**
** MATERIALS
**
*Material, name=Ball
        *Density
         1.2876e-08,
        *Elastic
        195000., 0.3
*Material, name=Cable
        *Damping, alpha=8., beta=0.00125
        *Density
         4.564e-09,
        *Elastic
         1673.95, 0.3
*Material, name=Star
        *Density
         8.91e-09,
        *Elastic
        129742., 0.3
*Material, name=Star_rigid
        *Density
         8.91e-09,
        *Elastic
         1.2742e+07, 0.3
**
```

```
** INTERACTION PROPERTIES
**
*Surface Interaction, name=Star_star_contact
1.,
        *Friction, slip tolerance=0.005
         0.163, , 0.001355
         0.156, , 0.001936
         0.142, , 0.002517
         0.149, , 0.003098
         0.125, , 0.003678
         0.142, , 0.004259
        *Surface Behavior, no separation, pressure-overclosure=HARD
*Film Property, name="heat transfer coeff"
0.1
**
** BOUNDARY CONDITIONS
**
** Name: Wire_end_fixed_first Type: Symmetry/Antisymmetry/Encastre
*Boundary
_PickedSet56, ZASYMM
**
** INTERACTIONS
**
** Interaction: Blade_receptacle
*Contact Pair, interaction=Star_star_contact
_PickedSurf103, _PickedSurf102
** Interaction: Spring_rece
*Contact Pair, interaction=Star_star_contact
_PickedSurf105, _PickedSurf104
** ----------------------------------------------------------------
**
** STEP: Load
**
*Step, name=Load, nlgeom=YES, inc=100000
*Dynamic,alpha=-0.05,haftol=0.5
1e-05,0.1,1e-15,0.1
**
** BOUNDARY CONDITIONS
**
** Name: fixed_rec Type: Symmetry/Antisymmetry/Encastre
*Boundary
_PickedSet108, ENCASTRE
**
** LOADS
**
** Name: Pre_load   Type: Concentrated force
```

```
*Cload, amplitude=Smooth_step
_PickedSet101, 2, -4.3
**
** OUTPUT REQUESTS
**
*Restart, write, frequency=0
**
** FIELD OUTPUT: F-Output-1
**
*Output, field, variable=PRESELECT
**
** HISTORY OUTPUT: H-Output-1
**
*Output, history, variable=PRESELECT
*End Step
** ----------------------------------------------------------------
**
** STEP: Implicit
**
*Step, name=Implicit, nlgeom=YES, inc=1000000
*Dynamic,alpha=-0.05,haftol=3.
1e-10,0.5,1e-15,0.5
**
** BOUNDARY CONDITIONS
**
** Name: Motion Type: Displacement/Rotation
*Boundary, op=NEW, amplitude=V30Hz
_PickedSet100, 1, 1
_PickedSet100, 2, 2, 1.2
** Name: Wire_end_fixed_first Type: Symmetry/Antisymmetry/Encastre
*Boundary, op=NEW
_PickedSet56, ZASYMM
** Name: fixed_rec Type: Symmetry/Antisymmetry/Encastre
*Boundary, op=NEW
**
** OUTPUT REQUESTS
**
*Restart, write, frequency=0
**
** FIELD OUTPUT: F-Output-1
**
*Output, field, variable=PRESELECT
**
** HISTORY OUTPUT: H-Output-1
**
*Output, history, variable=PRESELECT
```

*End Step

Appendix H- Input File for Thermal Cycling Model

```
**
** PARTS
**
*Part, name=Ball_2D
*Element, type=CPS4R
** Section: Ball_2D
*Solid Section, elset=_PickedSet6, material=Ball
2.55,
*End Part
**
*Part, name=Blade_new
*Element, type=CPE4RT
*Element, type=CPE3T
** Section: Blade_new
*Solid Section, elset=_PickedSet10, material=Star
1.,
*End Part
**
*Element, type=CPE4RT
** Section: Receptacle_nonrigid
*Solid Section, elset=_PickedSet45, material=Star
2.55,
** Section: Receptacle_rigid
*Solid Section, elset=_PickedSet44, material=Star_rigid
2.55,
*End Part
**
*Part, name=Spring_new
*Element, type=CPE4RT
** Section: Spring_2D
*Solid Section, elset=_PickedSet14, material=Star
1.5,
** Section: Annulus
*Solid Section, elset=_PickedSet13, material=Star
1.9,
*End Part
**
*Part, name=Wire_2D
*Element, type=CPE4RT
```

** Section: rubber
*Solid Section, elset=_PickedSet44, material=Rubber
1.,
** Section: Copper
*Solid Section, elset=_PickedSet45, material=copper
1.,
*End Part
**
**
** ASSEMBLY
**
*Assembly, name=Assembly
**
*Instance, name=Receptacle_part_2D-1, part=Receptacle_part_2D
*End Instance
**
*Instance, name=Ball_2D-1, part=Ball_2D
*End Instance
**
*Instance, name=Ball_2D-2, part=Ball_2D
*End Instance
**
*Instance, name=Ball_2D-3, part=Ball_2D
*End Instance
**
*Instance, name=Wire_2D-1, part=Wire_2D
*End Instance
**
*Instance, name=Spring_new-1, part=Spring_new
*End Instance
**
*Instance, name=Blade_new-1, part=Blade_new
*End Instance
**
*Surface, type=ELEMENT, name=_PickedSurf103, internal
*Surface, type=ELEMENT, name=_PickedSurf105, internal
*Surface, type=ELEMENT, name=_PickedSurf106, internal
*Surface, type=ELEMENT, name=_PickedSurf107, internal
*Surface, type=ELEMENT, name=_PickedSurf119, internal
*Surface, type=ELEMENT, name=_PickedSurf120, internal

*Surface, type=ELEMENT, name=_PickedSurf127, internal
*Surface, type=ELEMENT, name=_PickedSurf144, internal
*Surface, type=ELEMENT, name=_PickedSurf147, internal
*Surface, type=ELEMENT, name=_PickedSurf149, internal
*Surface, type=ELEMENT, name=_PickedSurf155, internal
*Surface, type=ELEMENT, name=_PickedSurf156, internal
*Surface, type=ELEMENT, name=_PickedSurf157, internal
*Surface, type=ELEMENT, name=_PickedSurf158, internal
*Surface, type=ELEMENT, name=_PickedSurf164, internal
** Constraint: Spring_rec
*Tie, name=Spring_rec, adjust=yes
_PickedSurf107, _PickedSurf106
** Constraint: ball-wire
*Tie, name=ball-wire, adjust=yes
_PickedSurf158, _PickedSurf157
** Constraint: rect-wire
*Tie, name=rect-wire, adjust=yes
_PickedSurf156, _PickedSurf155
*End Assembly
*Amplitude, name=Smooth_step, definition=SMOOTH STEP
0., 0., 0.1, 1.
*Amplitude, name=hr_1, definition=PERIODIC
1, 0.00174533, 0.0001, 0.
0., 1.
*Amplitude, name=hr_3, definition=PERIODIC
1, 0.000581776, 0.0001, 0.
0., 1.
*Amplitude, name=min_1, definition=PERIODIC
1, 0.10472, 0.001, 0.
0., 1.
*Amplitude, name=min_5, definition=PERIODIC
1, 0.020944, 0.0001, 0.
0., 1.
*Amplitude, name=min_10, definition=PERIODIC
1, 0.010472, 0.0001, 0.
0., 1.
*Amplitude, name=min_30, definition=PERIODIC
1, 0.00349066, 0.001, 0.
0., 1.
**

```
** MATERIALS
**
*Material, name=Ball
        *Density
        1.2876e-08,
        *Elastic
        195000., 0.3
*Material, name=Cable
        *Conductivity
        0.197,  37.9
        0.192, 149.1
        0.192, 204.6
        0.172, 260.2
        *Damping, alpha=8., beta=0.00125
        *Density
        4.564e-09,
        *Elastic
        1996.03,     0.3, -196.11
        2056.52,     0.3,  -67.78
        1850.87,     0.3,    -40.
        1930.,     0.3,     20.
        1016.16,     0.3,   23.89
        1645.21,     0.3,    100.
        1487.95,     0.3,  204.44
        *Expansion
        -0.000108,-173.
        -0.000114,-153.
        -0.000126,-113.
        -0.000136, -73.
        -0.000139, -53.
        -0.00014, -33.
        -0.00014, -13.
        -0.00014,  0.2
        -0.00014,   7.
        0.00014,  27.
        0.000149,  47.
        0.000155,  67.
        *Specific Heat
        8.52e+08,
*Material, name=Rubber
        *Conductivity
        0.197,  17.9
        0.192, 129.1
```

```
0.192, 184.6
0.172, 240.2
*Damping, alpha=0.001, beta=0.01
*Density
1.4e-09,
*Elastic
0.7, 0.5,  0.
0.67, 0.5, 30.
0.68, 0.5, 40.
0.63, 0.5, 51.
0.67, 0.5, 61.
0.62, 0.5, 76.
0.43, 0.5,100.
0.11, 0.5,130.
*Expansion
-0.000108, -193.
-0.000114, -173.
-0.000126, -133.
-0.000136,  -93.
-0.000139,  -73.
-0.00014,  -53.
-0.00014,  -33.
-0.00014, -19.8
-0.00014,  -13.
0.00014,    7.
0.000149,   27.
0.000155,   47.
*Specific Heat
6.92e+08,    0.
1.24526e+09,  17.9
5.18499e+09, 129.1
1.67656e+09, 184.6
1.83973e+09, 240.2
*Material, name=Star
*Conductivity
160.,    0.
164.,  36.2
181.,   99.
203., 181.2
223., 296.2
277., 402.2
256., 480.7
*Density
```

8.91e-09,
*Elastic
129742., 0.33, 0.
117953., 0.33, 3.89
117953., 0.33, 128.89
104163., 0.33, 184.44
104163., 0.33, 240.
*Expansion
1.63e-05, 0.
1.67e-07,107.
1 .78e-05,207.
1.87e-05,307.
1.95e-05,407.
2.09e-05,507.
2.13e-05,607.
2.16e-05,707.
*Specific Heat
1.8342e+08, -120.
2.53404e+08, -70.
3.23799e+08, -30.
3.43399e+08, -20.
3.85e+08, 0.
5.82301e+08, 79.6
6.45776e+08, 101.6
7.96709e+08, 149.3
8.563e+08, 166.7
*Material, name=Star_rigid
*Conductivity
160., 0.
164., 36.2
181., 99.
203., 181.2
223., 296.2
227., 402.2
256., 480.7
*Density
8.91e-09,
*Elastic
1.2742e+07, 0.33, 0.
1.27302e+07, 0.33, 3.89
1.27302e+07, 0.33, 128.89
1.27164e+07, 0.33, 184.44

1.27164e+07, 0.33, 240.
*Expansion
1.63e-05, 0.
1.67e-05,107.
1.78e-05,207.
1.87e-05,307.
1.95e-05,407.
2.09e-05,507.
2.13e-05,607.
2.16e-05,707.
*Specific Heat
1.8342e+08, -120.
2.53404e+08, -70.
3.23799e+08, -30.
3.43399e+08, -20.
3.85e+08, 0.
5.82301e+08, 79.6
6.45776e+08, 101.6
7.96709e+08, 149.3
8.563e+08, 166.7
*Material, name=copper
*Conductivity
483.,-193.
401., -20.
385., 0.
398., 7.
357., 707.
*Damping, alpha=0.01, beta=0.0025
*Density
 8.93e-09
*Elastic
123764., 0.3, -216.11
127211., 0.3, -87.78
115490., 0.3, -60.
120000., 0.3, 0.
67916., 0.3, 3.89
103769., 0.3, 80.
94805.5, 0.3, 184.44
*Expansion
1.64e-05, 0.
1.64e-05, 80.

1.85e-05,230.
2.02e-05,480.
2.48e-05,905.
*Specific Heat
349.96, -143.2
375.31, -93.2
381.29, -43.2
377.35,   -20.
380.57,   6.8
481.8,   56.8
588.49, 106.8
**
** INTERACTION PROPERTIES
**
*Surface Interaction, name=Star_star_contact
1.,
*Friction, slip tolerance=0.005
0.235, , 0.001355,   -30.
0.256, , 0.001936,   -30.
0.255, , 0.002517,   -30.
0.254, , 0.003098,   -30.
0.227, , 0.003678,   -30.
0.191, , 0.004259,   -30.
0.222, , 0.001355,   -10.
0.209, , 0.001936,   -10.
0.187, , 0.002517,   -10.
0.167, , 0.003098,   -10.
0.177, , 0.003678,   -10.
0.174, , 0.004259,   -10.
0.21, , 0.001355,   5.
0.192, , 0.001936,   5.
0.19, , 0.002517,   5.
0.189, , 0.003098,   5.
0.181, , 0.003678,   5.
0.162, , 0.004259,   5.
0.163, , 0.001355,   30.
0.156, , 0.001936,   30.
0.142, , 0.002517,   30.
0.149, , 0.003098,   30.
0.125, , 0.003678,   30.
0.142, , 0.004259,   30.

0.155, , 0.001355, 55.
0.167, , 0.001936, 55.
0.151, , 0.002517, 55.
0.145, , 0.003098, 55.
0.156, , 0.003678, 55.
0.139, , 0.004259, 55.
0.136, , 0.001355, 90.
0.118, , 0.001936, 90.
0.155, , 0.002517, 90.
0.149, , 0.003098, 90.
0.116, , 0.003678, 90.
0.139, , 0.004259, 90.
*Surface Behavior, no separation, pressure-overclosure=HARD
*Gap Conductance
1e+09, 0.
0., 1e-05
*Gap Heat Generation
1., 0.5
*Film Property, name=blade_conv
3.61e-06, -193.15
5.28e-06, -143.15
6.89e-06, -93.15
9.96e-06, 6.85
1.13e-05, 56.85
1.28e-05, 106.85
1.54e-05, 206.85
1.77e-05, 306.85
2.07e-05, 456.85
2.69e-05, 806.85
2.87e-05, 906.85
3.76e-05, 1206.85
5.52e-05, 1806.85
8.34e-05, 2206.85
0.000182, 2706.85
*Film Property, name=rec_conv
1.0669e-06, -193.15
1.5488e-06, -143.15
2.0139e-06, -93.15
2.9014e-06, 6.85
3.3016e-06, 56.85
3.713e-06, 106.85

4.4597e-06, 206.85
5.1307e-06, 306.85
5.9962e-06, 456.85
7.7925e-06, 806.85
8.3121e-06, 906.85
1.0882e-05, 1206.85
1.5976e-05, 1806.85
2.4113e-05, 2206.85
5.2756e-05, 2706.85
*Film Property, name=wire_conv
1.54e-06, -193.15
2.24e-06, -143.15
2.92e-06, -93.15
4.22e-06, 6.85
4.8e-06, 56.85
5.4e-06, 106.85
6.49e-06, 206.85
7.47e-06, 306.85
9.11e-06, 456.85
1.13e-05, 806.85
1.21e-05, 906.85
1.59e-05, 1206.85
2.33e-05, 1806.85
3.51e-05, 2206.85
7.69e-05, 2706.85
**
** BOUNDARY CONDITIONS
**
** Name: Wire_end_fixed_first Type: Symmetry/Antisymmetry/Encastre
*Boundary
_PickedSet154, ZASYMM
** Name: blade_fixed Type: Displacement/Rotation
*Boundary
_PickedSet152, 1, 1
_PickedSet152, 2, 2
** Name: fix_recp Type: Symmetry/Antisymmetry/Encastre
*Boundary
_PickedSet110, ENCASTRE
**
** INTERACTIONS

```
**
** Interaction: Blade_Rec
*Contact Pair, interaction=Star_star_contact
_PickedSurf119, _PickedSurf127
** Interaction: Blade_spring
*Contact Pair, interaction=Star_star_contact, type=SURFACE TO SURFACE
_PickedSurf164, _PickedSurf120
** ----------------------------------------------------------------
**
** STEP: Load
**
*Step, name=Load, nlgeom=YES, inc=1000000
*Coupled Temperature-Displacement, creep=none, steady state
1e-06, 0.1, 1e-20, 0.1
**
** LOADS
**
** Name: Load-1   Type: Concentrated force
*Cload, amplitude=Smooth_step
_PickedSet166, 2, -4.3
**
** OUTPUT REQUESTS
**
*Restart, write, frequency=0
**
** FIELD OUTPUT: F-Output-1
**
*Output, field
        *Node Output
        NT, U
        *Element Output, directions=YES
        S,
**
** HISTORY OUTPUT: H-Output-1
**
*Output, history
*Contact Output
CSTRESS,
*End Step
** ----------------------------------------------------------------
```

```
**
** STEP: temp
**
*Step, name=temp, nlgeom=YES, inc=10000000
*Coupled Temperature-Displacement, creep=explicit, deltmx=100., cetol=1.
1e-08, 60., 1e-20, 0.01
**
** BOUNDARY CONDITIONS
**
** Name: Wire_end_fixed_first Type: Symmetry/Antisymmetry/Encastre
*Boundary, op=NEW
_PickedSet154, ZASYMM
** Name: blade_fixed Type: Displacement/Rotation
*Boundary, op=NEW
_PickedSet152, 1, 1
_PickedSet152, 2, 2
** Name: fix_recp Type: Symmetry/Antisymmetry/Encastre
*Boundary, op=NEW
** Name: fix_recp2 Type: Symmetry/Antisymmetry/Encastre
*Boundary, op=NEW
_PickedSet168, YSYMM
**
** INTERACTIONS
**
** Interaction: blade_conv
*Sfilm, amplitude=sec_10
_PickedSurf144, F, 2., blade_conv
** Interaction: rec_conv
*Sfilm, amplitude=sec_10
_PickedSurf149, F, 2., rec_conv
** Interaction: wire_conv
*Sfilm, amplitude=sec_10
_PickedSurf147, F, 2., wire_conv
**
** OUTPUT REQUESTS
**
*Restart, write, frequency=0
**
** FIELD OUTPUT: F-Output-1
**
```

```
*Output, field
        *Node Output
        NT, U
        *Element Output, directions=YES
        S,
**
** FIELD OUTPUT: F-Output-2
**
*Contact Output, master=_PickedSurf120, slave=_PickedSurf164
CSTRESS,
**
** HISTORY OUTPUT: H-Output-1
**
*Output, history
*Contact Output
CSTRESS,
**
** HISTORY OUTPUT: H-Output-2
**
*Contact Output, master=_PickedSurf120, slave=_PickedSurf164
CSTRESS,
*End Step
```